AFRL-PR-WP-TR-1999-2115

THE EFFECT OF WORKING FLUID INVENTORY ON THE PERFORMANCE OF HELICALLY GROOVED HEAT PIPES

SCOTT K. THOMAS
R. MICHAEL CASTLE
KIRK L. YERKES

WRIGHT STATE UNIVERSITY
DEPARTMENT OF MECHANICAL AND MATERIALS ENGINEERING
DAYTON, OHIO 45435

SEPTEMBER 1999

INTERIM REPORT FOR 08/21/1998 – 08/20/1999

APPROVED FOR PUBLIC RELEASE; DISTRIBUTION UNLIMITED

PROPULSION DIRECTORATE
AIR FORCE RESEARCH LABORATORY
AIR FORCE MATERIEL COMMAND
WRIGHT-PATTERSON AIR FORCE BASE OH 45433-7251

20000211 078

[DTIC QUALITY INSPECTED 1

NOTICE

USING GOVERNMENT DRAWINGS, SPECIFICATIONS, OR OTHER DATA INCLUDED IN THIS DOCUMENT FOR ANY PURPOSE OTHER THAN GOVERNMENT PROCUREMENT DOES NOT IN ANY WAY OBLIGATE THE US GOVERNMENT. THE FACT THAT THE GOVERNMENT FORMULATED OR SUPPLIED THE DRAWINGS, SPECIFICATIONS, OR OTHER DATA DOES NOT LICENSE THE HOLDER OR ANY OTHER PERSON OR CORPORATION; OR CONVEY ANY RIGHTS OR PERMISSION TO MANUFACTURE, USE, OR SELL ANY PATENTED INVENTION THAT MAY RELATE TO THEM.

THIS REPORT IS RELEASABLE TO THE NATIONAL TECHNICAL INFORMATION SERVICE (NTIS). AT NTIS, IT WILL BE AVAILABLE TO THE GENERAL PUBLIC, INCLUDING FOREIGN NATIONS.

THIS TECHNICAL REPORT HAS BEEN REVIEWED AND IS APPROVED FOR PUBLICATION.

KIRK YERKES
Project Engineer
Power Generation & Thermal Branch
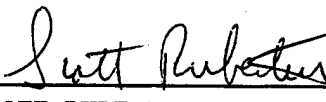
SCOTT RUBERTUS
Chief
Power Generation & Thermal Branc

FOR THE COMMANDER
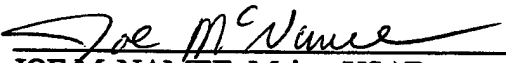
JOE McNAMEE, Major, USAF
Deputy Chief
Power Division

Do not return copies of this report unless contractual obligations or notice on a specific document requires its return.

REPORT DOCUMENTATION PAGE

1. AGENCY USE ONLY *(Leave blank)*	2. REPORT DATE	3. REPORT TYPE AND DATES COVERED
	SEPTEMBER 1999	INTERIM REPORT FOR 08/21/1998 - 08/20/1999

4. TITLE AND SUBTITLE
THE EFFECT OF WORKING FLUID INVENTORY ON THE PERFORMANCE OF HELICALLY GROOVED HEAT PIPES

5. FUNDING NUMBERS
C   F33615-98-1-2844
PE   62203
PR   3145
TA   20
WU   C5

6. AUTHOR(S)
SCOTT K. THOMAS
R. MICHAEL CASTLE
KIRK L. YERKES

7. PERFORMING ORGANIZATION NAME(S) AND ADDRESS(ES)
WRIGHT STATE UNIVERSITY
DEPARTMENT OF MECHANICAL AND MATERIALS ENGINEERING
DAYTON, OHIO 45435

8. PERFORMING ORGANIZATION REPORT NUMBER

9. SPONSORING/MONITORING AGENCY NAME(S) AND ADDRESS(ES)
PROPULSION DIRECTORATE
AIR FORCE RESEARCH LABORATORY
AIR FORCE MATERIEL COMMAND
WRIGHT-PATTERSON AFB, OH 45433-7251
POC: KIRK L. YERKES, AFRL/PRPG, 937-255-6241

10. SPONSORING/MONITORING AGENCY REPORT NUMBER

AFRL-PR-WP-TR-1999-2115

11. SUPPLEMENTARY NOTES

12a. DISTRIBUTION AVAILABILITY STATEMENT

APPROVED FOR PUBLIC RELEASE, DISTRIBUTION UNLIMITED.

12b. DISTRIBUTION CODE

13. ABSTRACT *(Maximum 200 words)*

The results of a recently completed experimental and analytical study showed that the capillary limit of a helically-grooved heat pipe (HGHP) was increased significantly when the transverse body force field was increased. This was due to the geometry of the helical groove wick structure. The objective of the present research was to experimentally determine the performance of revolving helically-grooved heat pipes when the working fluid inventory was varied. This report describes the measurement of the geometry of the heat pipe wick structure and the construction and testing of a heat pipe filling station. In addition, an extensive analysis of the uncertainty involved in the filling procedure and working fluid inventory has been outlined. Experimental measurements include the maximum heat transport, thermal resistance and evaporative heat transfer coefficient of the revolving helically-grooved heat pipe for radial accelerations of $|\vec{a_r}| = 0.0, 2.0, 4.0, 6.0, 8.0,$ and 10.0-g and working fluid fills of $G = 0.5, 1.0$ and 1.5. An existing capillary limit model was updated and comparisons were made to the present experimental data.

14. SUBJECT TERMS
Heat pipe, Revolving, Alternator, Cooling, Working Fluid Inventory

15. NUMBER OF PAGES
106

16. PRICE CODE

17. SECURITY CLASSIFICATION OF REPORT	18. SECURITY CLASSIFICATION OF THIS PAGE	19. SECURITY CLASSIFICATION OF ABSTRACT	20. LIMITATION OF ABSTRACT
UNCLASSIFIED	UNCLASSIFIED	UNCLASSIFIED	SAR

Contents

List of Figures

List of Tables

Nomenclature

a adiabatic length near the evaporator end cap, m

$\vec{a}_r$ radial acceleration, m/s^2

$\vec{A}$ acceleration vector at any point in the helical groove, m/s

A_e surface area in the evaporator section, $\pi r_v^2 L_e$, m^2

A_{gr} cross–sectional area of a groove, m^2

b adiabatic length near the condenser end cap, m

C_p specific heat at constant pressure, J/(kg-K)

D_o tube outside diameter, m

D_{vs} diameter of the heat pipe vapor space, m

$\hat{e}$ unit vector

$f_l \mathrm{Re}_l$ drag coefficient

G Ratio of liquid volume to total groove volume, V_l/V_{gr}

h groove height, m

h_e local heat transfer coefficient in the evaporator section, $Q_t/A_e(T_w - T_a)$, W/m^2-K

h_{fg} heat of vaporization, J/kg

I heater current, A

L_a adiabatic length, m

L_c condenser length, m

L_e evaporator length, m

L_{gr} helical groove length, m

L_t total heat pipe length, m

m_d mass of working fluid dispensed by the filling station, kg

m_l mass of liquid, kg

m_t total mass of working fluid inventory, kg

m_v mass of vapor, kg

$\dot{m}_{cw}$ coolant mass flow rate, kg/s

n	number of data samples
N_{gr}	number of grooves
p	helical pitch, m
P	pressure, N/m^2
Q_g	heat transfer due to a single groove, W
Q_{in}	heat input at the evaporator, W
Q_t	heat transported, W
r_c	capillary pore radius, m
r_h	radius of the helix, m
r_l	liquid hydraulic radius, m
r_o	outer pipe radius, m
r_v	radius of the heat pipe vapor space, m
R	radius of curvature, m
R_{th}	thermal resistance, K/W
R_{wire}	electrical resistance of heater lead wires, Ω
s	coordinate along the centerline of the heat pipe, m
t_w	tube wall thickness, m
T_a	adiabatic temperature, K
T_{actual}	actual temperature, K
T_{cec}	condenser end cap temperature, K
T_{cw}	coolant temperature, K
T_{eec}	evaporator end cap temperature, K
T_{in}	calorimeter inlet temperature, K
T_{out}	calorimeter outlet temperature, K
$T_{reading}$	thermocouple reading, K
T_{sat}	saturation temperature, K
T_w	outer wall temperature, K
v_l, v_v	specific volume of liquid and vapor, m^3/kg
V	heater voltage

V_b	burette volume, m³
V_{gr}	volume of the grooves, m³
V_p	pore volume, m³
V_t	total volume, m³
V_{vs}	vapor space volume, m³
w	width along the bottom of the groove, m
α	aspect ratio
β	groove aspect ratio
γ	meniscus contact angle, rad
Δ	uncertainty
ϵ	standard error
θ_1, θ_2	angles from the sides of the groove to vertical, rad
μ	absolute viscosity, kg/(m-s)
ρ	density, kg/m³
σ	surface tension, N/m
ϕ	helix angle, rad
φ	porosity

Subscripts

bf	body force
cap	capillary
g	gravity
gr	groove
l	liquid
max	maximum
v	vapor
vs	vapor space

Acknowledgement

The authors would like to acknowledge the technical assistance of Mr. Don Reinmuller.

1 Introduction

Helically–grooved heat pipes (HGHPs) have potential applications in the thermal management of rotating equipment such as aircraft alternators, large–scale industrial electric motors, and spinning satellites. In two recent studies (Klasing et al., 1999; Thomas et al., 1998), the performance of revolving HGHPs was investigated. It was found that the capillary limit increased with the strength of the acceleration field perpendicular to the heat pipe axis. In order to move HGHPs closer to application, knowledge must be gained concerning the sensitivity of the capillary limit to working fluid fill amount, since variations in the fill amount are inevitable during the manufacture of these devices. Very few studies were available concerning the effect of working fluid fill on the performance of axially–grooved heat pipes, but those found have been outlined below. In addition, synopses of the two aforementioned studies on revolving HGHPs have also been provided.

Brennan et al. (1977) developed a mathematical model to determine the performance of an axially–grooved heat pipe which accounts for liquid recession, liquid–vapor shear interaction and puddle flow in a 1-g acceleration environment. The model considered three distinct flow zones: the grooves unaffected by the puddle, the grooves that emerge from the puddle, and the grooves that are submerged by the puddle. The model for the puddle consisted of satisfying the equation of motion for the puddle and the continuity equation at the puddle–groove interface, and was solved by a fourth–order Runge–Kutta integration method with self–adjusting step sizes. The assumptions made by the model for the puddle were uniform heat addition and removal with a single evaporator and a single condenser section, and one–dimensional laminar flow in the puddle. The transport capability of the grooves unaffected by the puddle and the grooves extending beyond the puddle were approximated by a closed–form solution with laminar liquid and vapor flow. The working fluids used for the experiment were methane, ethane and ammonia. Brennan et al. (1977) stated that the mathematical model agreed well with the experimental data for ideally filled and overfilled heat pipes, but some differences were noted for underfilled heat pipes.

1

In general, it was found for ideally filled heat pipes the predicted transported heat was higher than that measured. Also, this discrepancy was more significant for lower operating temperatures. In addition, it was found during the experiments that the maximum transported heat increased with fill volume.

Vasiliev et al. (1981) performed a series of experiments on an aluminum axially-grooved heat pipe which was overfilled and ideally filled. The width and height of the grooves were $w = 0.123$ mm and $h = 0.7$ mm, respectively, with an overall heat pipe length of $L_t = 80.0$ cm. The working fluids were acetone and ammonia. Vasiliev et al. showed that the temperature difference from the evaporator to the adiabatic regions increased at a much slower rate with increasing overfills. This was attributed to a thin film of liquid emerging from the overfill pool wetting the upper grooves. Vasiliev et al. stated that this thin film was lifted over the grooves by capillary forces due to microroughness on the groove surface. A mathematical model was developed for low temperature axially-grooved heat pipes to estimate heat pipe performance for 0-g and 1-g applications. The mathematical model was a set of boundary-value problems applied to each groove and was solved by a numerical iteration method. The model was based on pressure balance equations and mass continuity written for a single groove. The temperature of the vapor in the adiabatic region was an input parameter, and the vapor pressure gradient was assumed to be one-dimensional. In addition, the liquid-vapor shear stress was assumed to be constant, and the starting liquid film thickness was of the same order of magnitude as the groove microroughness. Very good agreement was reported between the mathematical model and experimental transported heat results for ideally filled and overfilled heat pipes under gravity.

Thomas et al. (1998) presented experimental data obtained from a helically-grooved copper heat pipe which was tested on a centrifuge table. The heat pipe was bent to match the radius of curvature of the table so that uniform transverse (perpendicular to the axis of the heat pipe) body forces field could be applied along the entire length of the pipe. The steady-state performance of the curved heat pipe was determined by varying the heat input ($Q_{in} = 25$ to 250 W) and centrifuge table

2

velocity (radial acceleration $|\vec{a}_r| = 0.01$ to 10-g). It was found that the capillary limit increased by a factor of five when the radial acceleration increased from $|\vec{a}_r| = 0.01$ to 6-g due to the geometry of the helical grooves. A model was developed to calculate the capillary limit of each groove in terms of centrifuge table angular velocity, the geometry of the heat pipe and the grooves, and the temperature–dependent working fluid properties. The agreement between the model and the experimental data was satisfactory.

Klasing et al. (1999) developed a mathematical model to determine the operating limits of a revolving helically–grooved straight heat pipe. The capillary limit calculation required an analysis of the total body force imposed by rotation and gravity on the liquid along the length of the helical grooves. The boiling and entrainment limits were calculated using methods described by Faghri (1995). It was found that the capillary limit increased significantly with rotational speed due to the helical geometry of the heat pipe wick structure. The maximum heat transport was found to be a function of angular velocity and tilt angle from horizontal. In addition, a minimum value of angular velocity was required to obtain the benefits of the helical groove geometry.

The first objective of the present study was to determine the sensitivity of the performance of revolving HGHPs to the working fluid fill amount. This required a precise knowledge of the geometry of the heat pipe and helical grooves. In addition, a precision filling station was constructed and calibrated to determine the uncertainties involved in the filling procedure. The copper–ethanol heat pipe was tested on a centrifuge table at Wright–Patterson AFB (AFRL/PRPG) to determine the capillary limit, thermal resistance and evaporative heat transfer coefficient for fill ratios of $G = 0.5$, 1.0 and 1.5, and radial accelerations of $|\vec{a}_r| = 0.01$, 2.0, 4.0, 6.0, 8.0 and 10.0-g. The second objective of the present study was to improve the existing analytical capillary limit model developed by Thomas et al. (1998) using the above–mentioned geometric measurements and by using improved equations for the working fluid properties.

2 Determination of Heat Pipe Working Fluid Inventory

The objective of this analysis was to determine the working fluid inventory of a HGHP, which consists of the mass of liquid in the grooves and the mass of vapor in the vapor space. Since the heat pipe is a closed container under saturation conditions, the total mass of working fluid in the heat pipe is given by

$$m_t = m_v + m_l = \frac{V_{vs}}{v_v} + \frac{GV_{gr}}{v_l} \tag{1}$$

where V_{vs} and V_{gr} are the volumes of the vapor space and grooves, v_v and v_l are the specific volumes of the working fluid vapor and liquid, and $G = V_l/V_{gr}$ is the ratio of the volume of liquid to total groove volume. The volume of the vapor space is given by

$$V_{vs} = \frac{\pi}{4}D_{vs}^2 L_t + V_{gr}(1 - G) \tag{2}$$

where D_{vs} is the diameter of the heat pipe vapor space and L_t is the total heat pipe length. The second term in eqn. (2) accounts for the increase or decrease in the vapor space volume when the parameter G is varied. The volume of the grooves is given by

$$V_{gr} = L_{gr}N_{gr}A_{gr} \tag{3}$$

where N_{gr} is the total number of grooves, A_{gr} is the groove cross–sectional area, and L_{gr} is the total groove length.

A cross–sectional view of a typical helical groove in the experimental test article is shown in Fig. 1. The cross–sectional area of the groove is given by

$$A_{gr} = wh + \frac{1}{2}h^2(\tan\theta_1 + \tan\theta_2) \tag{4}$$

where h is the height of the groove, w is the width of the groove base, and the angles from the sides of the groove to vertical are θ_1 and θ_2. The total length of each groove is given by

$$L_{gr} = L_t \left[\left(\frac{2\pi r_h}{p}\right)^2 + 1\right]^{\frac{1}{2}} \tag{5}$$

4
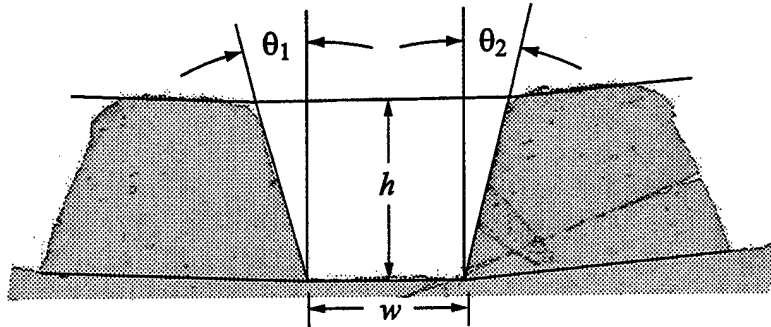
Figure 1: Photomicrograph of the helical groove geometry.

The radius of the helix is given by

$$r_h = \frac{1}{2}\left(D_{vs} + h\right) \tag{6}$$

The helical pitch is the distance through which the helix makes one revolution around its radius.

$$p = \frac{2\pi\left(s - s_1\right)}{\left(\phi - \phi_1\right)} \tag{7}$$

The helix angle ϕ corresponds to s, which is the distance traveled along the centerline of the heat pipe.

In order to calculate the working fluid inventory for the HGHP, measurements of the appropriate geometric parameters were made. These measurements are described in the following section. In addition, an extensive uncertainty analysis was performed to determine the uncertainties of both the measured and calculated variables used in finding the working fluid inventory.

5

2.1 Geometric Measurements

The physical variables given in eqn. (4) for the cross–sectional area of the grooves have been measured. A sample of the HGHP was set in an epoxy resin mold, polished, and examined under a Nikon (Model Epiphot) microscope with 50× magnification. Buehler Omnimet computer software was used to make bitmap pictures of ten different grooves and a microscopic calibration scale. These pictures were then analyzed using Adobe Illustrator software to determine the geometric values shown in Fig. 1. Since the corners at the top of the land between grooves were not well defined, a special procedure was established to determine the geometry of the grooves. First, lines were drawn along the bottom and sides of each groove. Then, a line was drawn across the bottom of the land between grooves, as shown in Fig. 1. This line was then transposed to the top of the land. The intersection between this line and the line along the side of the groove was defined as the upper corner of the groove. This procedure was also performed for the other side of the groove to establish the other corner. Note that the two lines along the land tops are at different angles due to the radius of curvature of the heat pipe container. The angles θ_1 and θ_2, and the height and width of the groove h and w were found using Adobe Illustrator software in conjunction with the microscopic calibration scale. However, the resolution of the calibration scale was 20 μm, which resulted in uncertainties of the groove area on the order of 12%. Therefore, the calibration scale was evaluated with a Nikon (Model R-14A) optical comparator as follows. The calibration scale was mounted in the optical comparator, and a distance of 300 μm indicated by the calibration scale was measured eight times as shown in Table 1. The bitmap picture of the calibration scale was then loaded into Adobe Illustrator and measured eight times using the Illustrator measurement tool, as shown in Table 2 to obtain a conversion factor. This factor was then used in the measurement of the groove height and width. Table 3 shows the raw data and average for each helical groove parameter over a sample of ten grooves.

The Nikon optical comparator was also used to determine the vapor space diameter

6

Table 1: Measurements of the calibration scale by the optical comparator.

Trial	Distance (cm)
1	0.0301
2	0.0299
3	0.0299
4	0.0301
5	0.0300
6	0.0300
7	0.0301
8	0.0301
Average	0.030025
Readability	±0.0001

Table 2: Measurements of the calibration scale by the Adobe Illustrator software.

Trial	Distance (cm)
1	4.7272
2	4.7390
3	4.7272
4	4.7272
5	4.7390
6	4.7272
7	4.7272
8	4.7390
Average	4.731625
Readability	±0.0059

Table 3: Statistical results for the helical groove geometry.

Groove Number	h (cm)	w (cm)	θ_1	θ_2
1	0.03806	0.03476	15.08°	14.08°
2	0.03838	0.03246	16.38°	11.63°
3	0.03851	0.03404	15.89°	13.88°
4	0.03958	0.03462	16.91°	13.67°
5	0.03857	0.03537	15.69°	14.77°
6	0.03791	0.03522	15.78°	13.20°
7	0.03830	0.03448	15.48°	13.74°
8	0.03777	0.03477	13.97°	13.50°
9	0.03800	0.03448	14.40°	14.82°
10	0.03806	0.03432	14.78°	14.69°
Average	0.03831	0.03445	15.44°	13.80°
Standard Deviation	0.00052	0.00080	0.90°	0.95°

Table 4: Statistical results for vapor space diameter.

Trial	D_{vs} (cm)	Trial	D_{vs} (cm)
1	1.3538	6	1.3564
2	1.3638	7	1.3538
3	1.3640	8	1.3564
4	1.3540	9	1.3665
5	1.3614	10	1.3564
Average	1.3586	Standard Deviation	0.0049

of the heat pipe container sample. The cross hairs of the optical comparator were carefully aligned with the top of the land between grooves on the left edge of the pipe. The comparator table was then moved until the land tops on the right edge of the pipe were aligned with the cross hairs. The diameter of the heat pipe vapor space was the distance of the table movement. Table 4 shows the raw data, average and standard deviation for ten vapor space diameter measurements.

The helical groove pitch was found using a vertical milling machine and an angular displacement transducer. The heat pipe container material was originally 1 m long. Approximately one-half was used to form the heat pipe, and the other half was used

to determine the pitch. The rotation angle $(\phi - \phi_1)$ and the corresponding distance along the centerline of the heat pipe $(s - s_1)$ has been found as shown in Fig. 2(a).

A heat pipe holding device was constructed from two angle aluminum uprights mounted to the table of a Positool vertical milling machine (Model S-1). Precision alignment blocks were attached to the undersides of the uprights to engage one of the grooves in the milling machine table for improved alignment. Nylon bushings were placed in the uprights to center both the heat pipe container and the shaft, which was concentric with the heat pipe container. A small pin was made from a 1.58 mm (0.0625 in) dowel pin, where one end was ground to 0.26 mm to fit in the base of the helical groove. This sprung pin was set in a hole in the shaft where it engaged one of the grooves, as shown in Fig. 2(b). A Trans–Tek angular displacement transducer (Model 0605) was mounted onto another piece of angle aluminum. A vertical 6.35 mm (0.25 in) dowel pin was placed in the angle aluminum to align with the angular displacement transducer shaft. The dowel pin was held by a collet installed in the milling machine spindle in order to fix the location of the displacement transducer. The shaft of the transducer was linked to the shaft within the heat pipe by three set screws. As the milling machine table moved the pipe over the stationary shaft, the pin followed the helical groove, causing the shaft to rotate. The angular displacement transducer measured this rotation. A Hewlett-Packard multimeter (Model 3478A) was used to measure the output voltage of the angular displacement transducer, as shown in Fig. 3. The distance of the table movement was $(s - s_1)$, which was read from the milling machine display unit. The transducer output voltage was measured over 10 cm lengths for ten different groups as shown in Table 5. Backlash errors were avoided by not reversing the table movement while taking data. The pitch was calculated using eqn. (7) at a point in the center of each 10 cm length. The helical pitch versus distance along the heat pipe container is presented in Fig. 4.

The total active heat pipe length was measured with a machinist's scale and a vernier caliper. The active length was the total container length minus the lengths of the two end caps which sealed the container.

(a)

② ③ ④ ⑤

① ⑥ Table movement
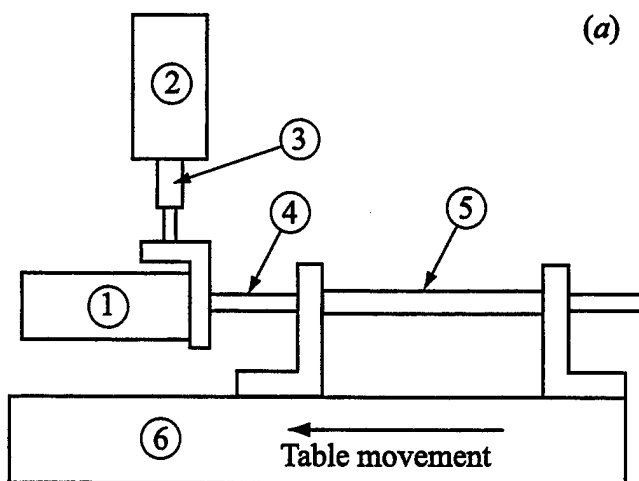
1. Angular Transducer   4. Shaft
2. Milling Machine Spindle 5. Heat Pipe Container
3. Milling Machine Collet   6. Milling Machine Table

Heat Pipe Container

(b)

Shaft
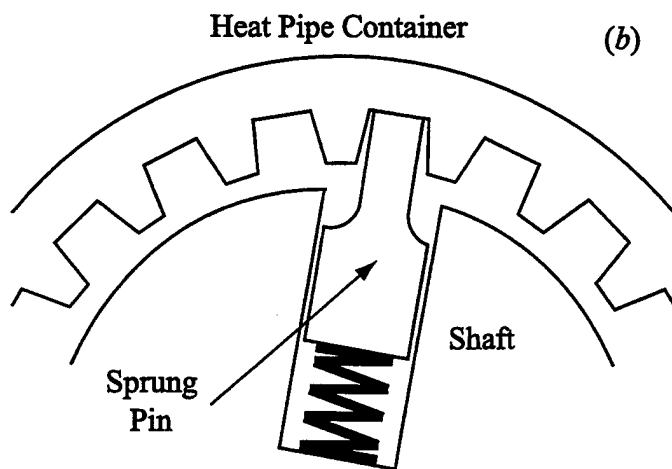
Sprung
Pin

Figure 2: Schematic of the helical pitch measurement technique: (a) Major components; (b) Cross-sectional view of sprung pin engaging a helical groove.
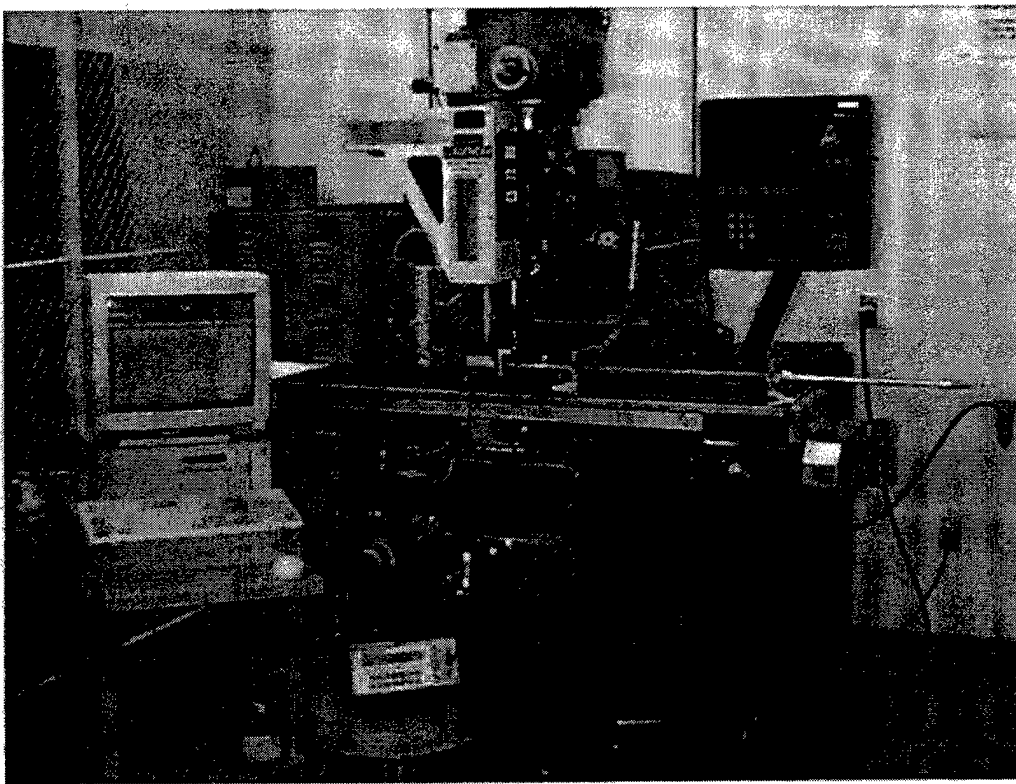
Figure 3: Photograph of the pitch measurement setup.
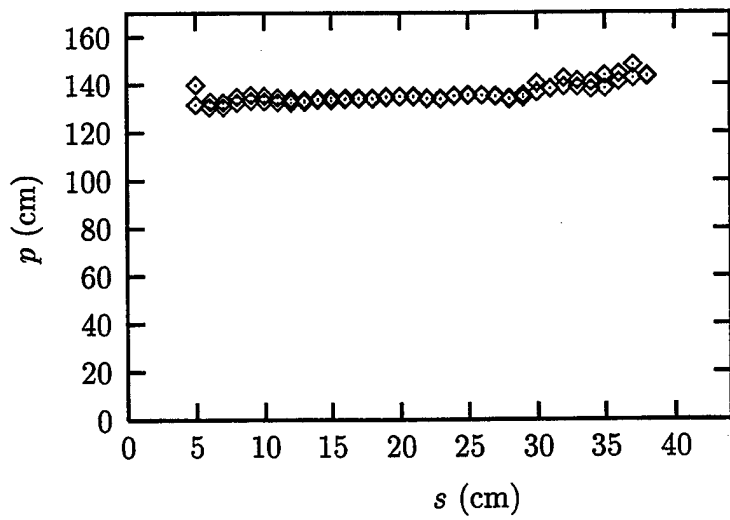
Figure 4: Helical pitch measurement data: $\bar{p} = 135.9$ cm.

Table 5: Measurements of the angular displacement voltage versus vertical milling machine travel.

Table Movement s (cm)	Transducer Voltage	Table Movement s (cm)	Transducer Voltage	Table Movement s (cm)	Transducer Voltage
0.0	0.9246	1.0	0.9992	2.0	1.1477
10.0	2.3569	11.12	2.5243	12.0	2.6589
20.0	3.8465	21.0	3.9982	22.0	4.1492
30.0	5.3273	31.0	5.478	32.0	5.6296
40.0	6.776	41.0	6.898	42.0	7.0338
40.0	6.7562	41.0	6.8962	42.0	7.0164
30.0	5.363	31.0	5.5093	31.998	5.6641
20.0	3.8876	21.0	4.0316	22.0	4.1789
10.0	2.38455	10.999	2.5328	12.0	2.684
0.0	0.86335	1.0	0.9996	1.999	1.1506
3.001	1.3068	4.0	1.4679	5.001	1.6183
13.0	2.792	14.0	2.9442	15.001	3.1004
23.0	4.2874	24.0	4.4335	25.006	4.5868
33.0	5.7794	34.0	5.9242	35.0	6.0517
43.0	7.1788	33.999	5.9354	35.0	6.0368
43.0	7.2109	24.0	4.4586	25.0	4.6110
33.0	5.817	14.0	2.9745	15.0	3.1278
22.998	4.3179	4.0	1.471	5.0	1.6219
13.0	2.8270				
3.0	1.3147				
6.0	1.7673	7.0	1.9100	8.0	2.0462
16.0	3.2564	17.0	3.4052	18.0	3.5462
26.0	4.7381	27.007	4.8980	28.0	5.0431
36.0	6.1890	37.0	6.3369	38.0	6.4862
36.0	6.2184	37.0	6.3304	38.0	6.4825
26.0	4.7704	27.0	4.9256	28.0	5.0670
15.999	3.2834	17.0	3.4299	18.0	3.5739
6.0	1.7740	7.0	1.9176	8.0	2.0638
9.0	2.2038				
19.0	3.6977				
29.0	5.1804				
39.02	6.6350				
39.0	6.6277				
29.0	5.2054				
19.0	3.7255				
9.0	2.2243				

2.2 Uncertainty Analysis

Using the analysis given by Miller (1989), the root–sum–square uncertainties for the groove cross–sectional area, helical pitch, helix radius, groove length, groove volume, vapor space volume, and total mass of the working fluid inventory are as follows. *Groove cross–sectional area:*

$$\Delta A_{\mathrm{gr}} = \left[\left(\frac{\partial A_{\mathrm{gr}}}{\partial w} \Delta w \right)^2 + \left(\frac{\partial A_{\mathrm{gr}}}{\partial h} \Delta h \right)^2 + \left(\frac{\partial A_{\mathrm{gr}}}{\partial \theta_1} \Delta \theta_1 \right)^2 + \left(\frac{\partial A_{\mathrm{gr}}}{\partial \theta_2} \Delta \theta_2 \right)^2 \right]^{\frac{1}{2}}$$

$$= \left[(h \Delta w)^2 + \{[w + h(\tan \theta_1 + \tan \theta_2)] \Delta h\}^2 + \left(\frac{1}{2} h^2 \sec^2 \theta_1 \Delta \theta_1 \right)^2 \right. \tag{8}$$

$$\left. + \left(\frac{1}{2} h^2 \sec^2 \theta_2 \Delta \theta_2 \right)^2 \right]^{\frac{1}{2}}$$

Helical pitch: The rotation angle of the angular displacement transducer (in arc degrees) was given by the following calibration equation

$$(\phi - \phi_1) = 17.986(V - V_1) \tag{9}$$

where V is the output voltage. Using this expression results in the following equation for helical pitch.

$$p = \frac{20.015(s - s_1)}{(V - V_1)} \tag{10}$$

Therefore, the uncertainty of the helical pitch measurement is

$$\Delta p = \left\{ \left(\frac{\partial p}{\partial (s - s_1)} \Delta (s - s_1) \right)^2 + \left[\frac{\partial p}{\partial (V - V_1)} \Delta (V - V_1) \right]^2 \right\}^{\frac{1}{2}}$$

$$= \left\{ \left(\frac{20.015 \, \Delta (s - s_1)}{(V - V_1)} \right)^2 + \left[\frac{20.015(s - s_1) \, \Delta (V - V_1)}{(V - V_1)^2} \right]^2 \right\}^{\frac{1}{2}} \tag{11}$$

Helix radius:

$$\Delta r_h = \left[\left(\frac{\partial r_h}{\partial D_{\mathrm{vs}}} \Delta D_{\mathrm{vs}} \right)^2 + \left(\frac{\partial r_h}{\partial h} \Delta h \right)^2 \right]^{\frac{1}{2}}$$

$$= \left[\left(\frac{\Delta D_{\mathrm{vs}}}{2} \right)^2 + \left(\frac{\Delta h}{2} \right)^2 \right]^{\frac{1}{2}} \tag{12}$$

13

Groove length:

$$\Delta L_{\mathrm{gr}} = \left[\left(\frac{\partial L_{\mathrm{gr}}}{\partial L_t} \Delta L_t \right)^2 + \left(\frac{\partial L_{\mathrm{gr}}}{\partial r_h} \Delta r_h \right)^2 + \left(\frac{\partial L_{\mathrm{gr}}}{\partial p} \Delta p \right)^2 \right]^{\frac{1}{2}}$$

$$= \left(\left\{ \left[\left(\frac{2\pi r_h}{p} \right)^2 + 1 \right]^{\frac{1}{2}} \Delta L_t \right\}^2 + \left\{ \frac{4\pi^2 L_t r_h}{p^2} \left[\left(\frac{2\pi r_h}{p} \right)^2 + 1 \right]^{-\frac{1}{2}} \Delta r_h \right\}^2 \right.$$

$$\left. + \left\{ \frac{4\pi^2 L_t r_h^2}{p^3} \left[\left(\frac{2\pi r_h}{p} \right)^2 + 1 \right]^{-\frac{1}{2}} \Delta p \right\}^2 \right)^{\frac{1}{2}} \quad (13)$$

Groove volume:

$$\Delta V_{\mathrm{gr}} = \left[\left(\frac{\partial V_{\mathrm{gr}}}{\partial L_{\mathrm{gr}}} \Delta L_{\mathrm{gr}} \right)^2 + \left(\frac{\partial V_{\mathrm{gr}}}{\partial A_{\mathrm{gr}}} \Delta A_{\mathrm{gr}} \right)^2 \right]^{\frac{1}{2}}$$

$$= \left[(N_{\mathrm{gr}} A_{\mathrm{gr}} \Delta L_{\mathrm{gr}})^2 + (N_{\mathrm{gr}} L_{\mathrm{gr}} \Delta A_{\mathrm{gr}})^2 \right]^{\frac{1}{2}} \quad (14)$$

Vapor space volume:

$$\Delta V_{\mathrm{vs}} = \left[\left(\frac{\partial V_{\mathrm{vs}}}{\partial D_{\mathrm{vs}}} \Delta D_{\mathrm{vs}} \right)^2 + \left(\frac{\partial V_{\mathrm{vs}}}{\partial L_t} \Delta L_t \right)^2 + \left(\frac{\partial V_{\mathrm{vs}}}{\partial V_{\mathrm{gr}}} \Delta V_{\mathrm{gr}} \right)^2 \right]^{\frac{1}{2}}$$

$$= \left[\left(\frac{\pi}{2} D_{\mathrm{vs}} L_t \Delta D_{\mathrm{vs}} \right)^2 + \left(\frac{\pi}{4} D_{\mathrm{vs}}^2 \Delta L_t \right)^2 + ((1 - G) \Delta V_{\mathrm{gr}})^2 \right]^{\frac{1}{2}} \quad (15)$$

Total mass of working fluid inventory:

$$\Delta m_t = \left[\left(\frac{\partial m_t}{\partial V_{\mathrm{vs}}} \Delta V_{\mathrm{vs}} \right)^2 + \left(\frac{\partial m_t}{\partial v_v} \Delta v_v \right)^2 + \left(\frac{\partial m_t}{\partial V_{\mathrm{gr}}} \Delta V_{\mathrm{gr}} \right)^2 \left(\frac{\partial m_t}{\partial v_l} \Delta v_l \right)^2 \right]^{\frac{1}{2}}$$

$$= \left[\left(\frac{\Delta V_{\mathrm{vs}}}{v_v} \right)^2 + \left(\frac{V_{\mathrm{vs}} \Delta v_v}{v_v^2} \right)^2 + \left(\frac{G \Delta V_{\mathrm{gr}}}{v_l} \right)^2 + \left(\frac{G V_{\mathrm{gr}} \Delta v_l}{v_l^2} \right)^2 \right]^{\frac{1}{2}} \quad (16)$$

In general, the uncertainties of the measured values were comprised of the readability and/or uncertainty of the measurement tool and the standard deviation found from several measurements. To be conservative, the greater of the readability or the uncertainty of the measurement tool was used in the calculations. The values of standard deviation for h, w, θ_1, θ_2 and D_{vs} are given in Tables 3 and 4. The readability or uncertainty of each instrument used in the measurements is provided in Table 6,

Table 6: Readability/uncertainty values for the instruments used in determining the working fluid inventory.

Instrument	Readability/ Uncertainty	Variables
Adobe Illustrator Angle Tool	$\pm 0.01°$	θ_1, θ_2
Adobe Illustrator Distance Tool	± 0.000037 cm	h, w
Optical Comparator	± 0.0001 cm	h, w, D_{vs}
Microscopic Calibration Scale	± 0.0001 cm	h, w
Multimeter	± 0.00455 V	$V - V_1$
Angular Displacement Transducer	± 0.0083 V	$V - V_1$
Vertical Milling Machine	± 0.001 cm	$s - s_1$
Machinist's Scale	± 0.079 cm	L_t
Vernier Caliper	± 0.0025 cm	L_t

which also indicates the variables found by each instrument. The groove height and width uncertainties included the readabilities of the optical comparator, the microscopic calibration scale and the Adobe Illustrator distance tool (Tables 1 and 2). The measured and calculated uncertainties for all geometric variables presented are shown in Table 7.

2.3 Working Fluid Properties

A literature survey was completed to determine the specific volumes of ethanol vapor and liquid at various saturation temperatures, as shown in Fig. 5. This information was needed to determine the total mass and uncertainty of the working fluid inventory $m_t \pm \Delta m_t$ [eqns. (1) and (16)]. While existing texts report these properties
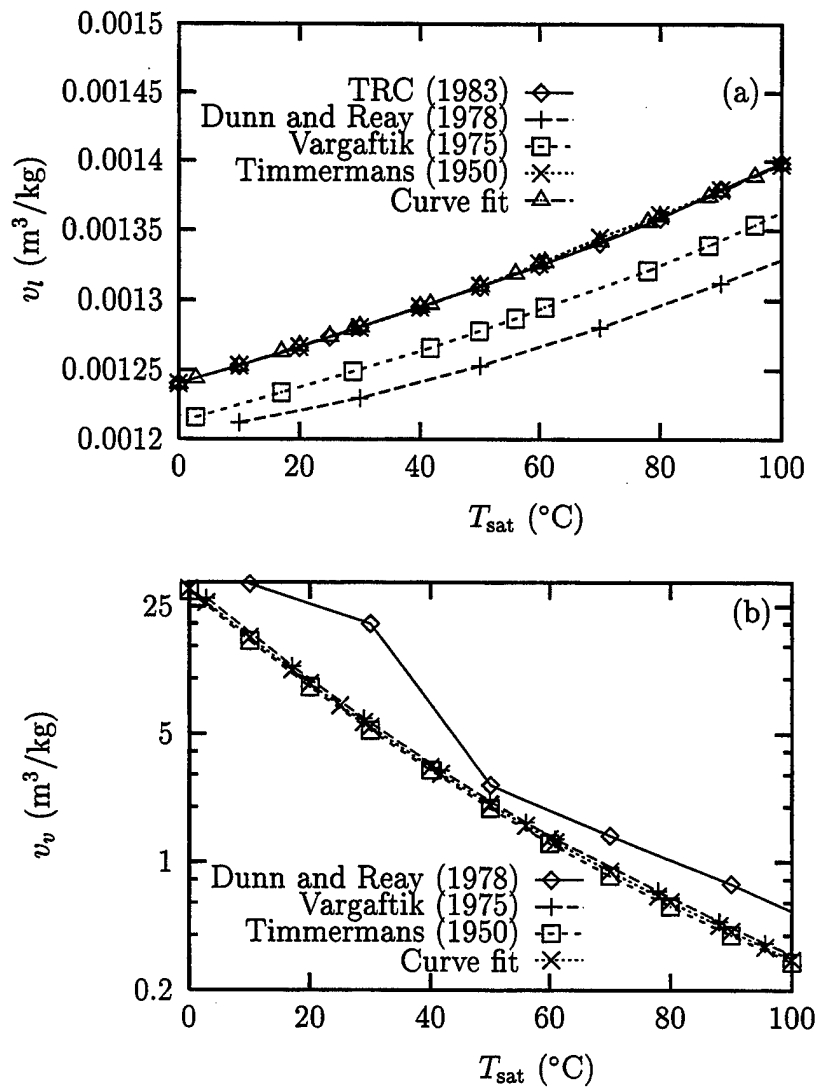
Figure 5: Specific volume of ethanol versus temperature: (*a*) Saturated liquid; (*b*) Saturated vapor.

Table 7: The geometric variable values associated with the working fluid inventory.

Measured Values	
h	0.03831 ± 0.00076 cm
w	0.03445 ± 0.0010 cm
θ_1	$15.44° \pm 0.91°$
θ_2	$13.80° \pm 0.96°$
$V - V_1$	1.474 ± 0.064 Volt
$s - s_1$	10.000 ± 0.023 cm
D_{vs}	1.359 ± 0.005 cm
L_t	43.8 ± 0.084 cm
Calculated Values	
A_{gr}	$1.703 \times 10^{-3} \pm 6.0 \times 10^{-5}$ cm^2
p	135.8 ± 5.9 cm
r_h	0.6992 ± 0.0025 cm
L_{gr}	43.82 ± 0.84 cm
V_{gr}	3.73 ± 0.13 cm^3

(Faghri, 1995; Peterson, 1994, Lide and Kehiaian, 1994; Carey, 1992; Schlunder, 1983; Ivanovskii et al., 1982), it was found that most simply referred to previous sources. Therefore, the data shown in Fig. 5 represent information gathered from primary sources that cannot readily be traced further. In Fig. 5(a), the available data for the specific volume of liquid in the range of $T_{sat} = 0$ to 100°C are relatively scattered. Vargaftik (1975) stated that the ethanol used was 96% pure by volume, with water making up most of the other 4%. Ethanol is agressively hygroscopic, so special procedures are required for further purification as outlined by Timmermans (1950) concerning anhydrous ethanol. Since the data by Timmermans (1950) and TRC (1983) are nearly coincident, it is believed that the data reported by TRC (1983) are also for anhydrous ethanol. Dunn and Reay (1978) do not provide information concerning purity. Therefore, the Vargaftik (1975) data and the Dunn and Reay (1978) data have been discarded in Fig. 5(a). In Fig. 5(b), the deviation of the Dunn and Reay (1978) data for the specific volume of vapor is significant. Therefore, the Dunn and Reay (1978) data has been discarded in Fig. 5(b). Polynomial curve fits from $0 \leq T_{sat} \leq 100°C$ have been obtained for the data shown in Figs. 5(a) and 5(b) for

17

Table 8: The calculated total mass of the working fluid inventory.

G	m_t (g)	Δm_t (g) Calculated [eqn. (16)]	Δm_d (g) Filling Station
0.5	1.47	$\pm$ 3.6%	$\pm$ 5.0%
1.0	2.92	$\pm$ 3.7%	$\pm$ 2.9%
1.5	4.38	$\pm$ 3.6%	$\pm$ 1.9%

the specific volumes of liquid and vapor ethanol. These curve fits have been evaluated at room temperature to determine the proper values to be used in the uncertainty analysis, since the heat pipe was filled at room temperature. Information concerning the uncertainty of the original data was not available. Therefore, the uncertainties of these properties have been estimated to be the maximum variance of the data from the curve fits ($\Delta v_l = 3.5 \times 10^{-8}$ m^3/kg, $\Delta v_v = 0.39$ m^3/kg). The specific volumes of liquid and vapor ethanol (m^3/kg) as functions of saturation temperature (°C) are shown below for the range $0 \leq T_{\text{sat}} \leq 100$°C

$$v_l = \exp(a_0 + a_1 T_{\text{sat}} + a_2 T_{\text{sat}}^2 + a_3 T_{\text{sat}}^3 + a_4 T_{\text{sat}}^4)/1000 \tag{17}$$

$$v_v = \exp(b_0 + b_1 T_{\text{sat}} + b_2 T_{\text{sat}}^2 + b_3 T_{\text{sat}}^3 + b_4 T_{\text{sat}}^4)/1000 \tag{18}$$

where the coefficients are

$a_0 = 0.2153$ $\quad\quad$ $b_0 = 10.35$

$a_1 = 1.049 \times 10^{-3}$ $\quad$ $b_1 = -6.375 \times 10^{-2}$

$a_2 = -1.345 \times 10^{-8}$ $\quad$ $b_2 = 1.735 \times 10^{-4}$

$a_3 = 2.025 \times 10^{-8}$ $\quad$ $b_3 = 5.714 \times 10^{-7}$

$a_4 = -5.474 \times 10^{-11}$ $\quad$ $b_4 = -6.003 \times 10^{-9}$

The total mass of the working fluid inventory m_t and the associated uncertainty Δm_t for the range of fill values are given in Table 8.

3 Heat Pipe Filling Station

3.1 Description

A filling station has been constructed which is capable of placing a low-temperature working fluid (i.e., water, ethanol, methanol) into a heat pipe without also introducing ambient air. A schematic of this station is shown in Fig. 6. The station consisted of a manifold of valves and interconnecting stainless steel tubing, a working fluid reservoir, a dispensing burette, a vacuum pump, and a container of compressed dry nitrogen gas. Previous experience with filling stations showed that long runs of horizontal tubing could cause significant filling errors due to vapor bubbles within the tubing. To address this problem, the manifold was constructed such that the interconnecting tubing runs were very short (on the order of 2 cm). In addition, the tubes which intersect the main vertical tube between valves 2 and 5 (Fig. 6) were offset from each other and ran at a diagonal from the main tube. Again, the purpose of this design was to reduce the possibility of vapor bubbles adhering to the tubing walls, thus causing errors in the fill amount. However, it is likely that some vapor still does adhere to the tubing, so certain procedures were carried out during filling to eject as much vapor as possible. For instance, the 1 psig relief valve over valve 1 was cycled on and off several times. In addition, valves 2 and 5 were cycled on and off while noting the meniscus displacement within the dispensing burette. If the meniscus was displaced more than 0.06 cm^3, vapor was probably trapped within the valve. The valve in question was then cycled until the bubble was ejected.

To fill the heat pipe, the container was first evacuated to a pressure of 10^{-6} Torr using a Varian turbomolecular vacuum pump (Model V450). The sealed pipe was then connected to the filling station at valve 5. The working fluid was frozen and thawed repeatedly to reduce the amount of dissolved air within the fluid. The entire filling station was then evacuated by a roughing pump, except the working fluid reservoir. After evacuation, the liquid working fluid was drawn up into the dispensing burette and into all interconnecting tubing. After noting the height of the meniscus, the
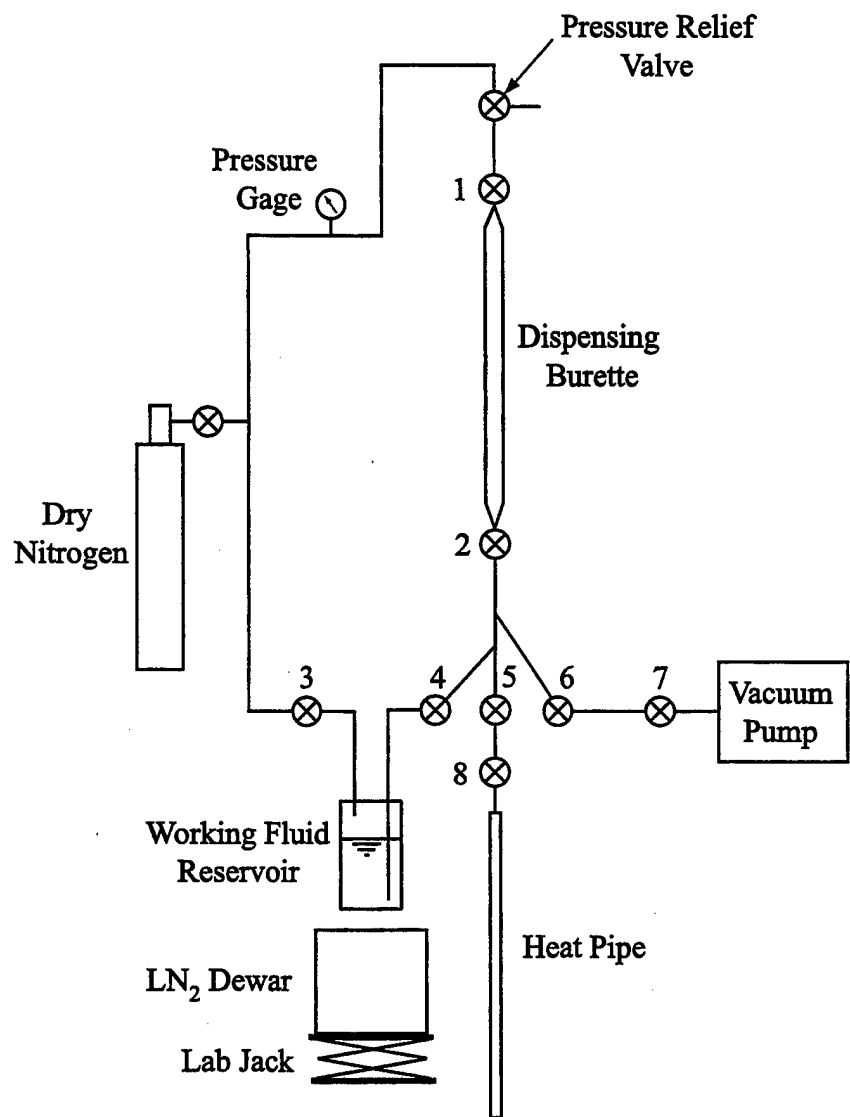
Figure 6: Schematic of the heat pipe filling station.

desired amount of working fluid was metered into the heat pipe by carefully opening the heat pipe fill valve 8. The difference in height of the liquid column was related to the dispensed mass of working fluid. A full description of the step-by-step process is provided in Section 9.1.

3.2 Uncertainty Analysis of the Dispensed Mass of Working Fluid

During initial testing of the filling station, it was found that the mass of working fluid dispensed into the heat pipe container was different than what was indicated by the dispensing burette. Therefore, a rigorous calibration of the filling station was undertaken to determine a correlation between the change in volume read by the dispensing burette and the change in mass of a receiving burette attached at valve 5, which was measured using a precision scale (Mettler Model PC4400). Figure 7(a) shows eight sets of data taken at seven different fill levels during the filling station calibration process and a linear curve fit to the data. Figure 7(b) indicates the maximum residual of the data from the linear curve fit. As expected, the residual percentage decreased as the dispensed working fluid amount increased. The maximum residual was added to the readability of the dispensing burette ($\pm$ 0.02 cm^3) to determine the total uncertainty of the working fluid inventory dispensed by the heat pipe filling station Δm_d as a function of the groove percentage (Table 8).
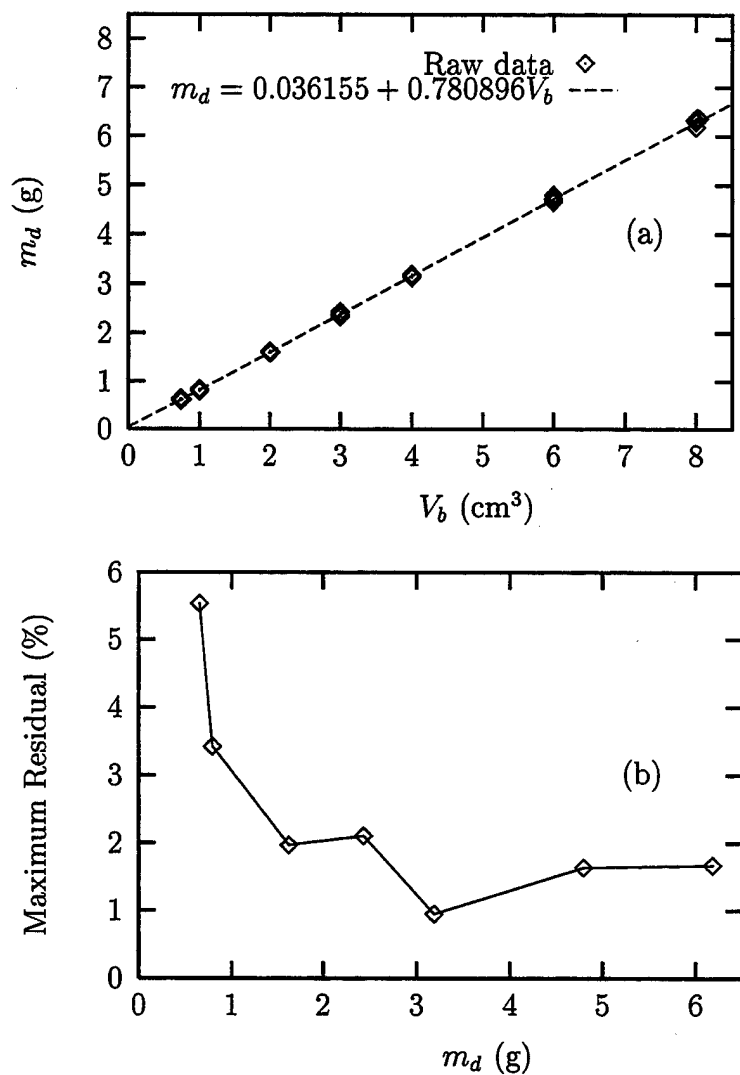
Figure 7: Calibration of the heat pipe fill station: (a) Dispensed mass versus dispensing burette volume; (b) Maximum residual of the data from the linear curve fit.
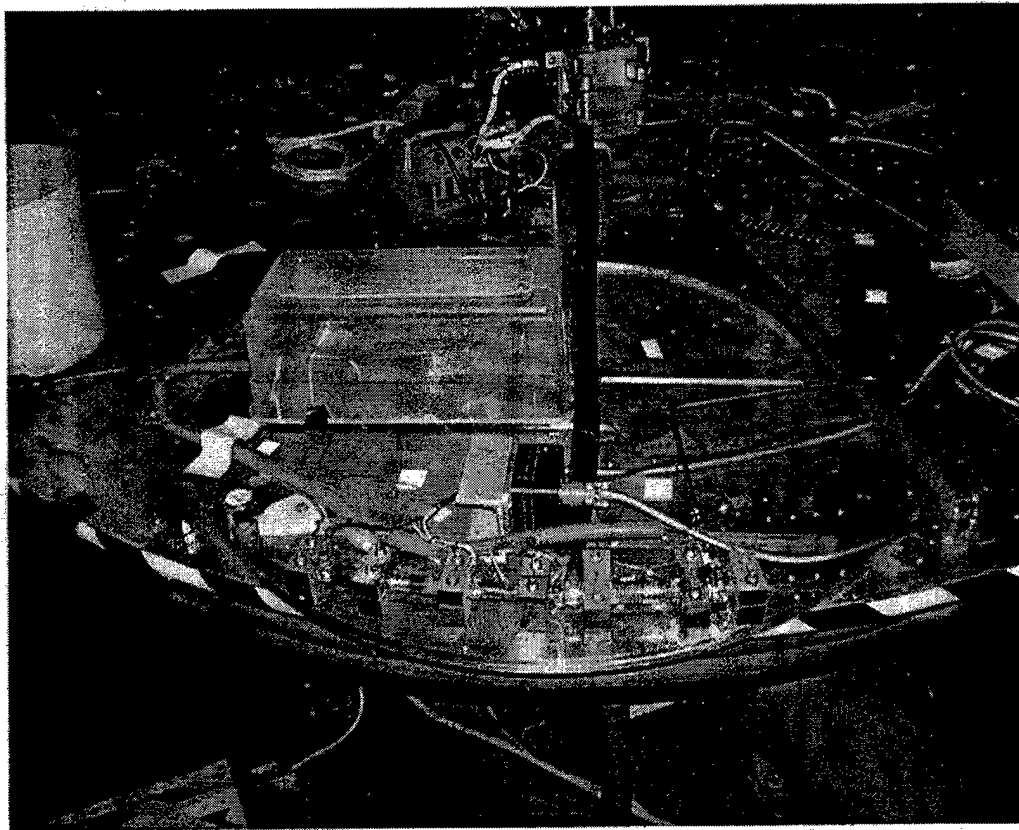
Figure 8: Experimental setup for testing the helically–grooved heat pipe.

4 Experimental Setup

The purpose of the experiment was to examine the steady–state performance of a helically–grooved copper–ethanol heat pipe under various heat inputs and transverse body force fields using a centrifuge table located at the Air Force Research Laboratory located at Wright–Patterson AFB (AFRL/PRPG). Specifically, the amount of working fluid was varied ($G = 0.5$, 1.0 and 1.5) to determine the effects of under/overfilling on the capillary limit, thermal resistance and evaporative heat transfer coefficient of the HGHP. To ensure uniform radial acceleration fields over the length of the heat pipe, the pipe was bent to match the radius of curvature of the centrifuge table ($R = 1.22$ m) as shown in Fig. 8. Physical information concerning the heat pipe is given in Table 9.   It should be noted that the total helix angle was very small: Each

23

Table 9: Helically–grooved heat pipe specifications.

Working fluid	Ethanol
Working fluid charge	$m_t = 1.47$, 2.92 and 4.38 g
Evaporator length	$L_e = 15.2 \pm 0.16$ cm
Adiabatic length	$L_a = 8.2 \pm 0.16$ cm
Condenser length	$L_c = 15.2 \pm 0.16$ cm
Tube outside diameter	$D_o = 1.588 \pm 0.005$ cm
Tube wall thickness	$t_w = 0.0757$ cm
Radius of curvature	$R = 1.22$ m
Wall/wick materials	Copper
Wick structure	Helical grooves
Number of Grooves	$N_{gr} = 50$
Heater element	Nichrome heater tape
Fill valve	Nupro B-4HW bellows valve
Calorimeter	1/8 in. OD coiled copper tubing

groove rotated through an angle of approximately 2.03 rad (116 arc degrees) over the length of the pipe. The heat pipe was mounted to a platform overhanging the edge of the horizontal centrifuge table. This allowed the heat pipe to be positioned such that the radius of curvature was equivalent to the outermost radius of the centrifuge table. Insulative mounting blocks were used to ensure that the heat pipe matched the prescribed radius as closely as possible. The horizontal centrifuge table was driven by a 20-hp dc motor. The acceleration field near the heat pipe was measured by a Columbia Research Laboratories (Model SA-307-TX) triaxial accelerometer. The acceleration field at the centerline of the heat pipe radius was calculated from these readings using a coordinate transformation.

A Clayborn Labs (Model J-16-2) pressure–sensitive nichrome heater tape with an aluminized backing was uniformly wound around the circumference of the evaporator section for heat input. Power was supplied to the heat pipe evaporator section by a Kepco (Model ATE150-7m) power supply through power slip rings to the table. While the current reading could be made directly using a precision ammeter, the voltage across the electric heater had to be measured on the rotating table because

of the voltage drop between the control room and the table. Therefore, the voltage at the heater was obtained through the instrumentation slip ring assembly and read by a Hewlett Packard (Model 3478A) precision multimeter.

The calorimeter consisted of a length of 1/8 in. OD copper tubing wound tightly around the condenser section. The size of the tubing was chosen to be small to minimize the effects of acceleration on the performance of the calorimeter. Thermal grease was used between the heat pipe and the calorimeter to decrease contact resistance. Type T thermocouples were inserted through brass T–branch connectors into the coolant inlet and exit streams, and a Signet (Model 8511) high-resolution digital flow meter was used to measure the mass flow rate of the coolant (50% by mass ethylene glycol/water mixture). The mass flow rate was controlled using a high–pressure booster pump, which aided the low–pressure pump in the recirculating chiller. The temperature of the coolant was maintained at a constant setting by the recirculating chiller ($T_{cw} = 30°C$). Coolant was delivered to the centrifuge table via a double–pass hydraulic rotary coupling. The mass flow rate was constant for all experiments. Values of the specific heat of ethylene glycol/water mixtures have been obtained from ASHRAE (1977), which were in terms of percent ethylene glycol by weight and temperature. The average temperature between the calorimeter inlet and outlet was used to evaluate the specific heat. The specific heat did not vary appreciably during testing since it is a weak function of temperature.

The Signet high–resolution digital flow meter was calibrated using a Mettler (Model PC4400) scale and a stop watch. The temperature of the ethylene glycol solution was set to $T_{in} = 30°C$, which was measured at the calorimeter inlet location. The temperature was monitored by Viewdac data acquisition software. The flow was then allowed to fill a graduated cylinder for 60 s, after which the mass of the ethylene glycol solution was recorded. This was repeated several times at different flow rates. The signal coming from the flow meter was displayed by a Signet 8511 Compak flow transmitter with the K-factor set to 2629. The results of the calibration are given in Table 10. The time and mass values shown in the table were averaged from the raw

Table 10: Averaged flow rates at different Signet meter readings.

Signet meter reading	Time $\pm$ 1.0 (s)	Mass $\pm$ 0.01 (g)	$\dot{m}_{cw}$ (g/s)
0.14	60.0	185.64	3.10 ± 0.05
0.15	60.0	207.06	3.45 ± 0.06
0.16	60.0	211.80	3.53 ± 0.06

data. The percentage of ethylene glycol in the coolant was measured in the following manner. The specific gravity of the coolant was found by mixing 530 g of water to 530 g of pure ethylene glycol, which was measured with a Cole–Parmer (Model 08292–16) hydrometer. The mass of the water and ethylene glycol each was measured with a Mettler (Model PC4400) scale. The hydrometer measurement was within 1.5% of the ratio of masses obtained from weighing the water and ethylene glycol separately before mixing them and the ASHRAE (1977) values. The percentage of ethylene glycol was measured periodically during testing to ensure that the mixture did not change.

Heat pipe temperatures were measured by Type T surface–mount thermocouples, which were held in place using Kapton tape. Mounting locations for the thermocouples are shown in Fig. 9. A short unheated length next to the evaporator end cap was instrumented with thermocouples specifically for the detection of dryout in the evaporator section and accurate thermal resistance measurements. In addition, groups of four thermocouples were arranged around the circumference of the heat pipe at stations in the evaporator section for local heat transfer coefficient information. Temperature signals were conditioned and amplified on the centrifuge table. These signals were transferred off the table through the instrumentation slip ring assembly, which was completely separate from the power slip ring assembly to reduce electronic noise. Conditioning the temperature signals prior to leaving the centrifuge table eliminated difficulties associated with creating additional junctions within the slip ring assembly. Temperature and acceleration signals were collected using a Keithley
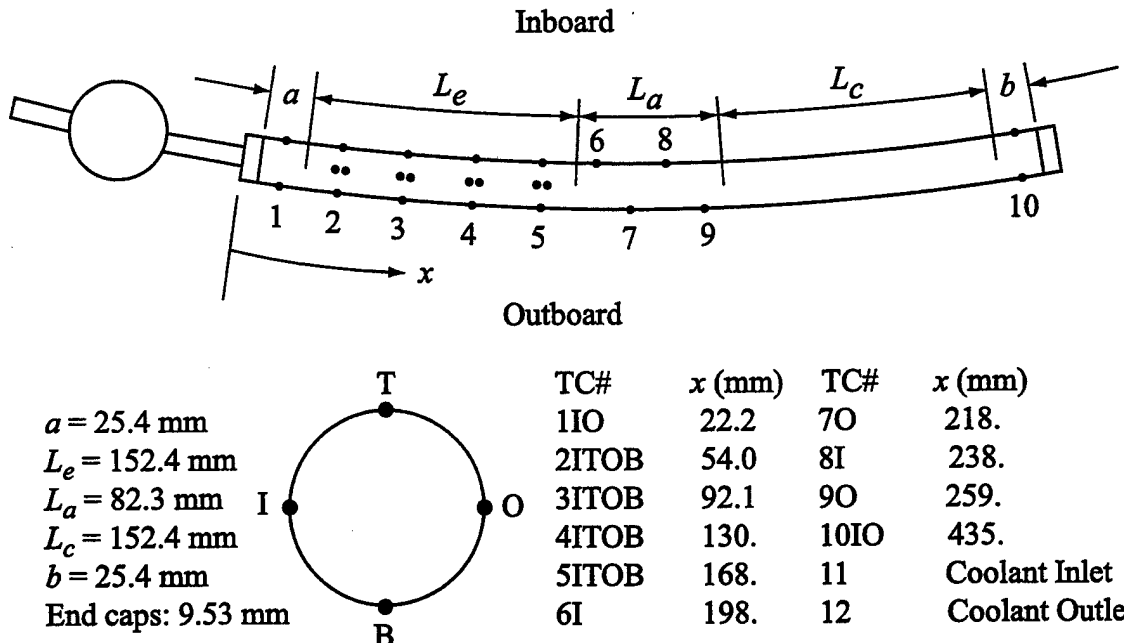
Figure 9: Thermocouple locations and relevant lengths.

TC#	x (mm)	TC#	x (mm)
1IO	22.2	7O	218.
2ITOB	54.0	8I	238.
3ITOB	92.1	9O	259.
4ITOB	130.	10IO	435.
5ITOB	168.	11	Coolant Inlet
6I	198.	12	Coolant Outlet

$a = 25.4$ mm
$L_e = 152.4$ mm
$L_a = 82.3$ mm
$L_c = 152.4$ mm
$b = 25.4$ mm
End caps: 9.53 mm

Table 11: Data acquisition mapping.

Data Acquisition Channel	Relay Number	Switch ON	Switch OFF
TC0	-	1-I	1-I
TC1	-	1-O	1-O
TC2	-	10-I	10-I
TC3	-	11	11
TC4	-	12	12
TC5	1	2-I	2-O
TC6	1	3-I	3-O
TC7	1	4-I	4-O
TC8	1	5-I	5-O
TC9	2	2-T	2-B
TC10	2	3-T	3-B
TC11	2	4-T	4-B
TC12	2	5-T	5-B
TC13	3	6-I	7-O
TC14	3	8-I	9-O
TC15	3	OPEN	10-O

(Model 500A) DAQ conditioner and a personal computer with Viewdac data logging software. Since a shortage of thermocouple channels existed on the centrifuge table, a series of three electrical relays were engaged to read one set of thermocouples, and disengaged to read the other set, as shown in Table 11. Also shown in this table is the mapping between the thermocouple reference name and data acquisition channel number.

Since the heat pipe assembly was subjected to air velocities due to the rotation of the table (up to 11 m/s = 25 mi/hr), efforts were made to reduce convective heat losses from the exterior of the heat pipe. A thin–walled aluminum box was fabricated to fit around the heat pipe. Ceramic wool insulation was placed inside the box and around the heat pipe through three small doors on the top of the box. This insulation/box arrangement provided an effective barrier to convective losses from the heat pipe to the ambient.

The helically-grooved copper-ethanol heat pipe was tested in the following manner. The recirculating chiller was turned on and allowed to reach the setpoint temperature, which was measured at the calorimeter inlet ($T_{in} = 30°C$). The coolant flow rate was set to $\dot{m}_{cw} = 3.45$ g/s (Signet reading of 0.15). The centrifuge table was started from the remote control room at a slow constant rotational speed to prevent damage to the power and instrumentation slip rings. In this case, the radial acceleration was less than $|\vec{a}_r| < 0.01$-g. In all cases, the centrifuge table rotated in a clockwise direction as seen from above. Power to the heater was applied ($Q_{in} = 10$ W) and the heat pipe was allowed to reach a steady-state condition, which was determined by monitoring the evaporator temperature detected by thermocouple 2-I until changes of less than 0.1°C over 2 min. were noted. The power to the heater was then increased to $Q_{in} = 20$ W and again the heat pipe was allowed to reach a steady–state condition. This was repeated until the maximum allowable evaporator temperature was reached ($T_{heater,max} = 100°C$) or the maximum power input was reached ($Q_{in,max} = 200$ W). After all data had been recorded the power to the heater was turned off, and the heat pipe was allowed to cool before shutting down the centrifuge table.

The power input to the electric heater was calculated using the average of five amperage and voltage readings taken during each test. Also, a correction was made for the losses generated by a short length of wire leading to the heater. Therefore, the heat input is

$$Q_{\text{in}} = IV - I^2(R_{\text{wire}}) \tag{19}$$

The heat removed from the heat pipe by the calorimeter is given by

$$Q_{\text{t}} = \dot{m}C_p \left(T_{\text{out}} - T_{\text{in}}\right) \tag{20}$$

The thermal resistance of the heat pipe was defined as the ratio of the temperature drop across the heat pipe to the transported heat

$$R_{\text{th}} = \frac{T_{\text{eec}} - T_{\text{cec}}}{\dot{m}C_p \left(T_{\text{out}} - T_{\text{in}}\right)} \tag{21}$$

where T_{eec} is the evaporator end cap temperature measured by TC1–I, and T_{cec} is the condenser end cap temperature measured by TC10–I. The heat transfer coefficient in the evaporator section is

$$h_e = \frac{Q_t}{A_e(T_w - T_a)} \tag{22}$$

where T_w represents the external wall temperatures measured in the evaporator section. Using the analysis given by Miller (1989), the uncertainties for the heat input, transported heat thermal resistance and heat transfer coefficient are

$$\Delta Q_{\text{in}} = \sqrt{\left[(V - 2IR_{\text{wire}})\,\Delta I\right]^2 + (I\Delta V)^2 + (I^2\Delta R_{\text{wire}})^2} \tag{23}$$

$$\Delta Q_{\text{t}} = \sqrt{\left[C_p \left(T_{\text{out}} - T_{\text{in}}\right)\Delta\dot{m}\right]^2 + \left[\dot{m}\left(T_{\text{out}} - T_{\text{in}}\right)\Delta C_p\right]^2 + \left(\dot{m}C_p\Delta T_{\text{in}}\right)^2 + \left(\dot{m}C_p\Delta T_{\text{out}}\right)^2} \tag{24}$$

$$\Delta R_{\text{th}} = \left\{ \left[\frac{\Delta T_{\text{eec}}}{\dot{m}C_p \left(T_{\text{out}} - T_{\text{in}}\right)}\right]^2 + \left[\frac{\Delta T_{\text{cec}}}{\dot{m}C_p \left(T_{\text{out}} - T_{\text{in}}\right)}\right]^2 + \left[\frac{(T_{\text{eec}} - T_{\text{cec}})\Delta\dot{m}}{\dot{m}^2C_p \left(T_{\text{out}} - T_{\text{in}}\right)}\right]^2 \right.$$
$$\left. + \left[\frac{(T_{\text{eec}} - T_{\text{cec}})\Delta C_p}{\dot{m}C_p^2 \left(T_{\text{out}} - T_{\text{in}}\right)}\right]^2 + \left[\frac{(T_{\text{eec}} - T_{\text{cec}})\Delta T_{\text{in}}}{\dot{m}C_p \left(T_{\text{out}} - T_{\text{in}}\right)^2}\right]^2 + \left[\frac{(T_{\text{eec}} - T_{\text{cec}})\Delta T_{\text{out}}}{\dot{m}C_p \left(T_{\text{out}} - T_{\text{in}}\right)^2}\right]^2 \right\}^{\frac{1}{2}} \tag{25}$$

29

Table 12: Maximum uncertainties of measured and calculated values.

Measured Values	
Mass flow rate	$\Delta \dot{m} = \pm\ 0.05$ g/s
Heater voltage	$\Delta V = \pm\ 0.5$ V
Heater current	$\Delta I = \pm\ 0.1$ A
Radial acceleration	$\Delta a_r = \pm\ 0.1$-g
Electrical wire resistance	$\Delta R_{\text{wire}} = \pm\ 2.4 \times 10^{-3}\ \Omega$
Calorimeter inlet temp.	$\Delta T_{\text{in}} = \pm\ 0.07$ K
Calorimeter outlet temp.	$\Delta T_{\text{out}} = \pm\ 0.08$ K
Evaporator end cap temp.	$\Delta T_{\text{eec}} = \pm\ 0.09$ K
Condenser end cap temp.	$\Delta T_{\text{cec}} = \pm\ 0.11$ K
Calculated Values	
Heat input	See Fig. 10
Heat transported	$\Delta Q_t = \pm\ 3.21$ W
Thermal resistance	See Fig. 11
Heat transfer coefficient	See Figs. 16 and 17

$$\Delta h_e = \left[\left(\frac{\Delta Q_t}{A_e(T_w - T_a)} \right)^2 + \left(\frac{Q_t \Delta A_e}{A_e^2(T_w - T_a)} \right)^2 + \left(\frac{Q_t \Delta T_w}{A_e(T_w - T_a)^2} \right)^2 \right.$$
$$\left. + \left(\frac{Q_t \Delta T_a}{A_e(T_w - T_a)^2} \right)^2 \right]^{\frac{1}{2}} \tag{26}$$

All of the measured and calculated uncertainty values for the experimental data are presented in Table 12.

5 Analytical Capillary Limit Model for HGHPs

The analytical model used in the present work was proposed by Thomas et al. (1998). The model used an iterative approach to solve for the heat transported by each groove, which was then summed to determine the total heat transported by the heat pipe. Starting with the following equation for the pressure balance in a heat pipe (Faghri, 1995; Chi, 1976)

$$\Delta P_{\mathrm{cap,max}} \geq \Delta P_v + \Delta P_l + \Delta P_{\mathrm{bf}} \tag{27}$$

an equation was derived for the pressure balance for a single helical groove (Thomas et al., 1998)

$$\frac{\sigma}{r_c} \geq \frac{(L_e + 2L_a + L_c)}{h_{\mathrm{fg}}} \left\{ \frac{4\mu_v Q_t}{\pi \rho_v r_v^4} + \frac{\mu_l Q_g \left(f_l \mathrm{Re}_l\right)}{4\rho_l r_l^2 A_{\mathrm{gr}} \varphi} \left[\left(\frac{2\pi r_h}{p}\right)^2 + 1 \right]^{1/2} \right\}$$

$$- \rho_l \left[\left(\frac{2\pi r_h}{p}\right)^2 + 1 \right]^{1/2} \left[\int_0^{L_t} \widehat{e}_{x_3} \cdot \left(-\vec{A} + \{-g\} \widehat{e}_{z_1} \right) \, ds \right] \tag{28}$$

An extensive analysis of the geometric parameters of the helically–grooved heat pipe showed that the groove geometry more closely matched a trapezoidal groove as opposed to the rectangular groove assumed by Thomas et al. (1998). In the model by Thomas et al. (1998), the liquid hydraulic radius corresponded to a rectangular channel

$$r_l = \frac{2hw}{2h + w} \tag{29}$$

in which the porosity was $\varphi = 1.0$. In addition, the coefficient of friction for a rectangular duct proposed by Shah and Bhatti (1987) was used

$$f_l \mathrm{Re}_l = 24(1 - 1.3553\alpha + 1.9467\alpha^2 - 1.7012\alpha^3 + 0.9564\alpha^4 - 0.2537\alpha^5) \tag{30}$$

where the aspect ratio is $\alpha = w/h$. In the updated model, the liquid hydraulic radius for a trapezoidal groove is

$$r_l = \frac{2[wh + 0.5h^2(\tan\theta_1 + \tan\theta_2)]}{w + h(\sec\theta_1 + \sec\theta_2)} \tag{31}$$

The porosity is defined by the ratio of pore volume to the total volume of the wick structure. Therefore, for a trapezoidal groove the porosity is

$$\varphi = \frac{V_p}{V_t} = \frac{N_{gr} L_t A_{gr}}{L_t \pi (r_o^2 - r_v^2)} = \frac{N_{gr}[wh + 0.5h^2(\tan\theta_1 + \tan\theta_2)]}{\pi(r_o^2 - r_v^2)} \tag{32}$$

where h, w, θ_1, and θ_2 are shown in Fig. 1. The coefficient of friction was changed to the value for a trapezoidal duct ($f_l \mathrm{Re}_l = 14.21$) given by Shah (1975).

The thermal physical properties of ethanol given by Faghri (1995) were used by Thomas et al. (1998). It was found from an extensive literature search that the properties reported by Faghri (1995) were for aqueous ethanol which is 96% ethanol by volume and 4% water. In the present experiment 99.9% anhydrous ethanol was used as the working fluid. Therefore, the density of the liquid and vapor will be changed to the best-fit equations found in Sec. 2.3.

In the Thomas et al. (1998) model, the maximum capillary pressure for a rectangular groove was given as

$$\Delta P_{\mathrm{cap,max}} = \frac{\sigma}{r_c} = \frac{2\sigma}{w} \tag{33}$$

where σ is the surface tension and r_c is the capillary pore radius. Thomas et al. (1999) provides the capillary pore radius for liquid flowing in trapezoidal grooves. As the meniscus recedes into the groove during evaporation, the meniscus bifurcates into two separate flows in the corners of the groove. This point of bifurcation is assumed in the present analysis to be when dryout occurs in the heat pipe. The capillary pore radius at the point of bifurcation is (Thomas et al., 1999)

$$r_c = \frac{h}{2}\left[1 + (\beta + \tan\theta)^2\right] \tag{34}$$

where $\beta = w/2h$ is the groove aspect ratio. The meniscus contact angle at bifurcation is a function of the groove geometry.

$$\gamma_b = \tan^{-1}\left[\frac{(3\beta^2 - 4)\cos\theta + \beta^2 \cos 3\theta}{8\beta\cos\theta + (\beta^2 + 4)\sin\theta + \beta^2 \sin 3\theta}\right] \tag{35}$$

Equations (34) and (35) were used to determine the capillary pore radius at the point of dryout in the following manner. The groove aspect ratio was calculated using the

32

Table 13: Comparison of the parameters used in the analytical model for predicting the capillary limit of the helically–grooved heat pipe.

	Thomas et al. (1998)	Present
h (m)	4.420×10^{-4}	3.831×10^{-4}
w (m)	4.735×10^{-4}	3.445×10^{-4}
L_a (m)	0.1016	0.0823
r_v (m)	6.730×10^{-3}	6.793×10^{-3}
p (m)	1.385	1.358
$f_l \mathrm{Re}_l$	14.22	14.21
φ	1.0	0.5063
r_l (m)	3.064×10^{-4}	2.997×10^{-4}
r_h (m)	6.950×10^{-3}	6.985×10^{-3}
ρ_v (at $T_{\mathrm{sat}} = 40°\mathrm{C}$) (kg/m^3)	0.2753	0.3036
ρ_l (at $T_{\mathrm{sat}} = 40°\mathrm{C}$) (kg/m^3)	780.1	772.3
r_c (m)	4.735×10^{-4}	2.252×10^{-4}

groove height and width found in Table 3 ($\beta = 0.4496$). As per the discussion by Thomas et al. (1999), this value of β indicates that the meniscus must recede into the groove before the bifurcation point can be reached. Therefore, eqn. (35) was solved iteratively to determine the aspect ratio for which the meniscus contact angle was equal to the minimum meniscus contact angle for the copper-ethanol system. Faghri (1995) gives this value as $\gamma_0 = 7°$ for a receding meniscus. With $\gamma_b = \gamma_0 = 7°$ and $\theta = 14.62°$ (average groove half-angle from Table 3), the resulting aspect ratio was $\beta = 1.2112$. Solving for h, which is now the height of the meniscus above the groove bottom, results in $h = 0.01422$ cm. Substituting this value into eqn. (34) for the meniscus radius of curvature gives $r_c = 0.0002252$ cm.

Table 13 shows all of the variables used by Thomas et al. (1998) and the updated values used in the present work. The most significant changes are to the wick porosity and capillary pore radius.

6 Results and Discussion

The objective of this experiment was to determine the steady–state performance of a revolving helically–grooved heat pipe as a function of the working fluid inventory. The heat input, radial acceleration and working fluid fill were varied as follows: Q_{in} = 10 to 180 W, $|\vec{a}_r|$ = 0.01 to 10-g, and G = 0.5, 1.0 and 1.5. Thermocouples on the inboard, outboard, top, and bottom sides of the heat pipe (Fig. 9) were used to determine the axial and circumferential temperature distributions. Typical steady-state temperature distributions for the heat pipe for G = 1.0 at $|\vec{a}_r|$ = 0.01-g are shown in Fig. 10. All of the steady–state temperature distributions collected during this research are presented in Sec. 9.4. For low power input levels, the temperature distribution was uniform. As the power input increased, the temperatures within the evaporator and the short unheated section adjacent to the evaporator increased significantly, indicating a partial dryout situation. Since the coolant temperature and flow rate were constant for all tests, the adiabatic and condenser temperatures increased slightly with input power. Figure 11 shows the thermal resistance versus transported heat over the entire range of radial acceleration for each fill level. In Fig. 11(a) the thermal resistance was quite high, which indicates that the heat pipe was partially dried out for G = 0.5, even at the lowest power input levels. However, the thermal resistance decreased significantly as the radial acceleration increased, showing that the capillary pumping ability of the helical grooves increased. For G = 1.0 and 1.5, the thermal resistance decreased and then increased with transported heat when dryout commenced. The G = 1.5 fill tests showed dryout occurring only for $|\vec{a}_r|$ = 0.01 and 2.0-g. Dryout was not reached for G = 1.5 with $|\vec{a}_r|$ = 4.0, 6.0, 8.0 and 10.0-g due to reaching the maximum allowable heater temperature ($T_{heater,max}$ = 100°C). The capillary limit was considered to be reached when the thermal resistance began to increase as defined by Thomas et al. (1998).

Thomas et al. (1998) presented a mathematical model which predicted the capillary limit of a helically–grooved heat pipe subjected to a transverse body force. This model accounted for the geometry of the heat pipe and the grooves (including helix
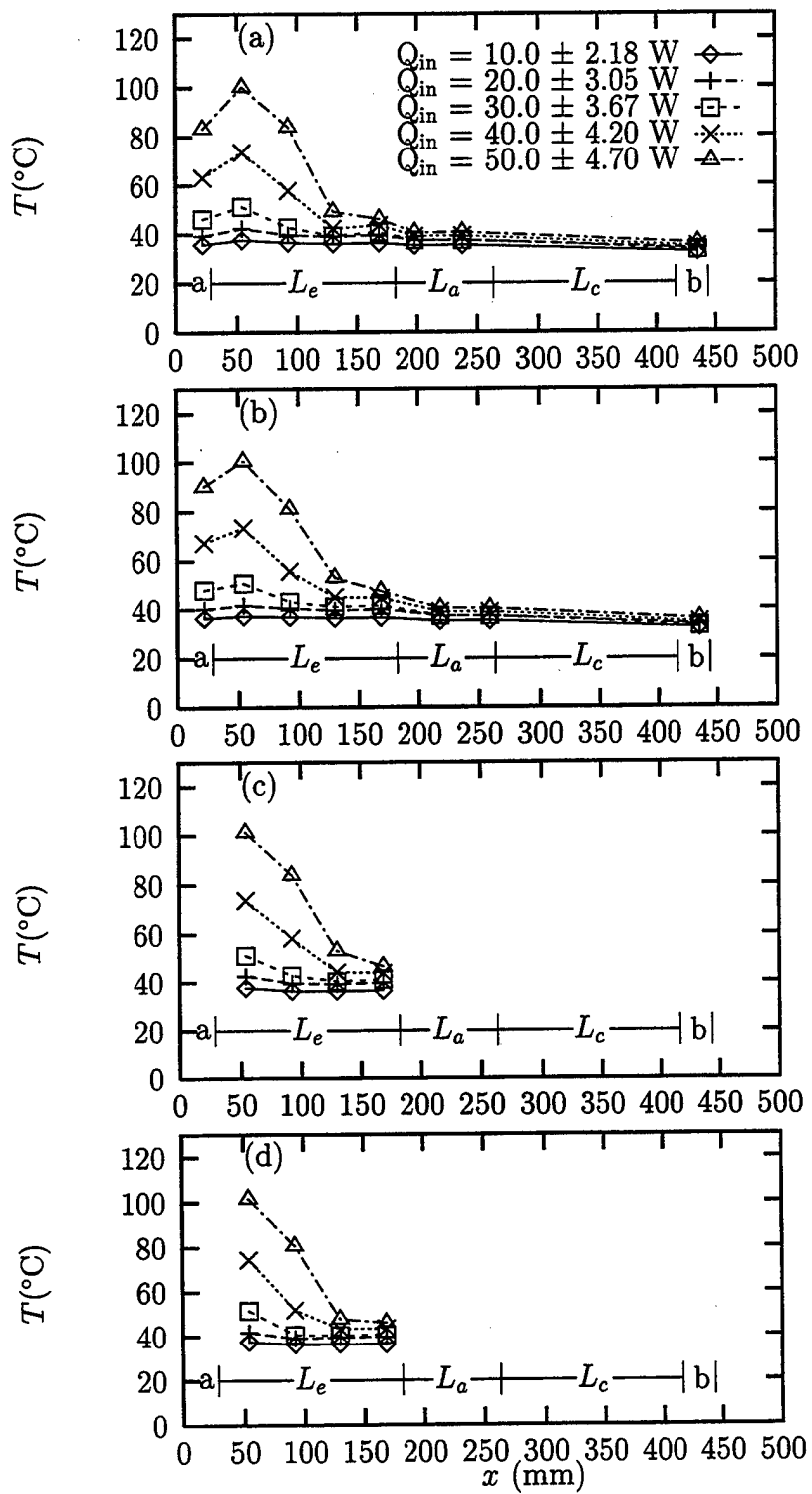
Figure 10: Steady–state temperature distributions for $|\vec{a}_r| = 0.01$-g, $G = 1.0$: (a) Inboard; (b) Outboard; (c) Top; (d) Bottom.
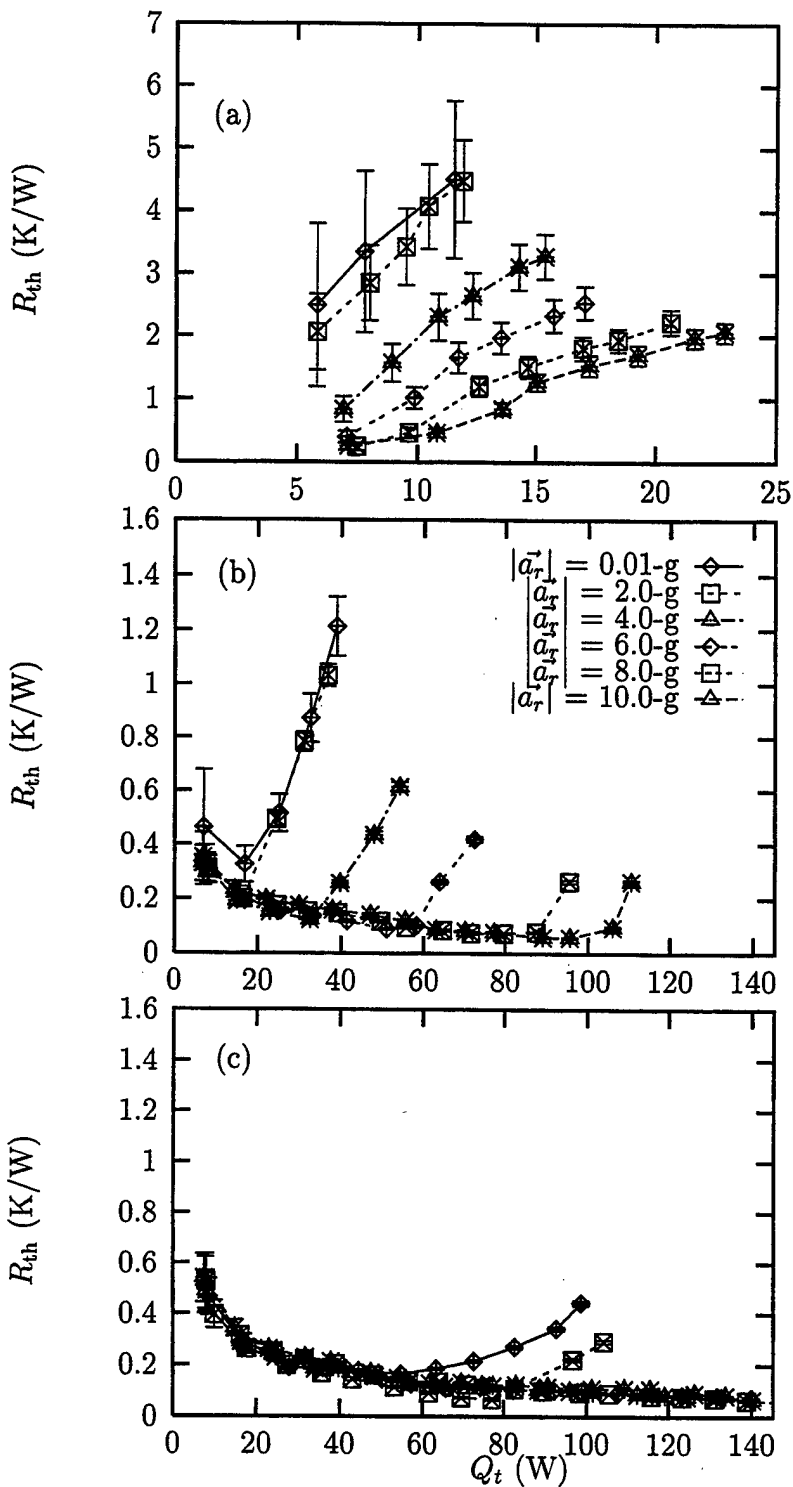
Figure 11: Thermal resistance versus heat transport: (a) $G = 0.5$; (b) $G = 1.0$; (c) $G = 1.5$.
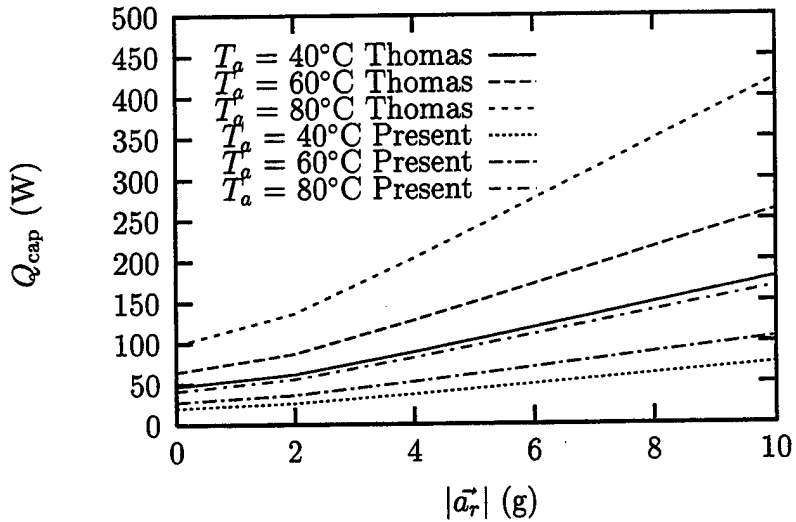
Figure 12: Capillary limit versus radial acceleration comparison of present model and Thomas et al. (1998).

pitch), body force field strength, and temperature–dependent working fluid properties. The capillary limit versus radial acceleration is given in Fig. 12 for various working temperatures with the Thomas et al. (1998) model and the present model in which improvements were made as discussed in Sec. 5. The capillary limit increased steadily with radial acceleration and working temperature. The present model shows a significantly lower prediction for the capillary limit when compared to the Thomas model due to the improved geometric measurements and working fluid property equations.

Figure 13 shows a comparison of the experimental data and present analytical model for the capillary limit of a revolving helically–grooved heat pipe. No attempt was made to maintain a constant adiabatic temperature during the experiments. Therefore, the working fluid temperature in the model was set to the adiabatic temperature found experimentally. For $G = 0.5$, the heat pipe operated successfully only for $|\vec{a}_r| \geq 8.0$-g. In Fig. 13(b) ($G = 1.0$), the capillary limit increased significantly with radial acceleration. With the heat pipe overfilled by 50% ($G = 1.5$), the capillary limit increased dramatically, showing the effect that overfilling has on performance.
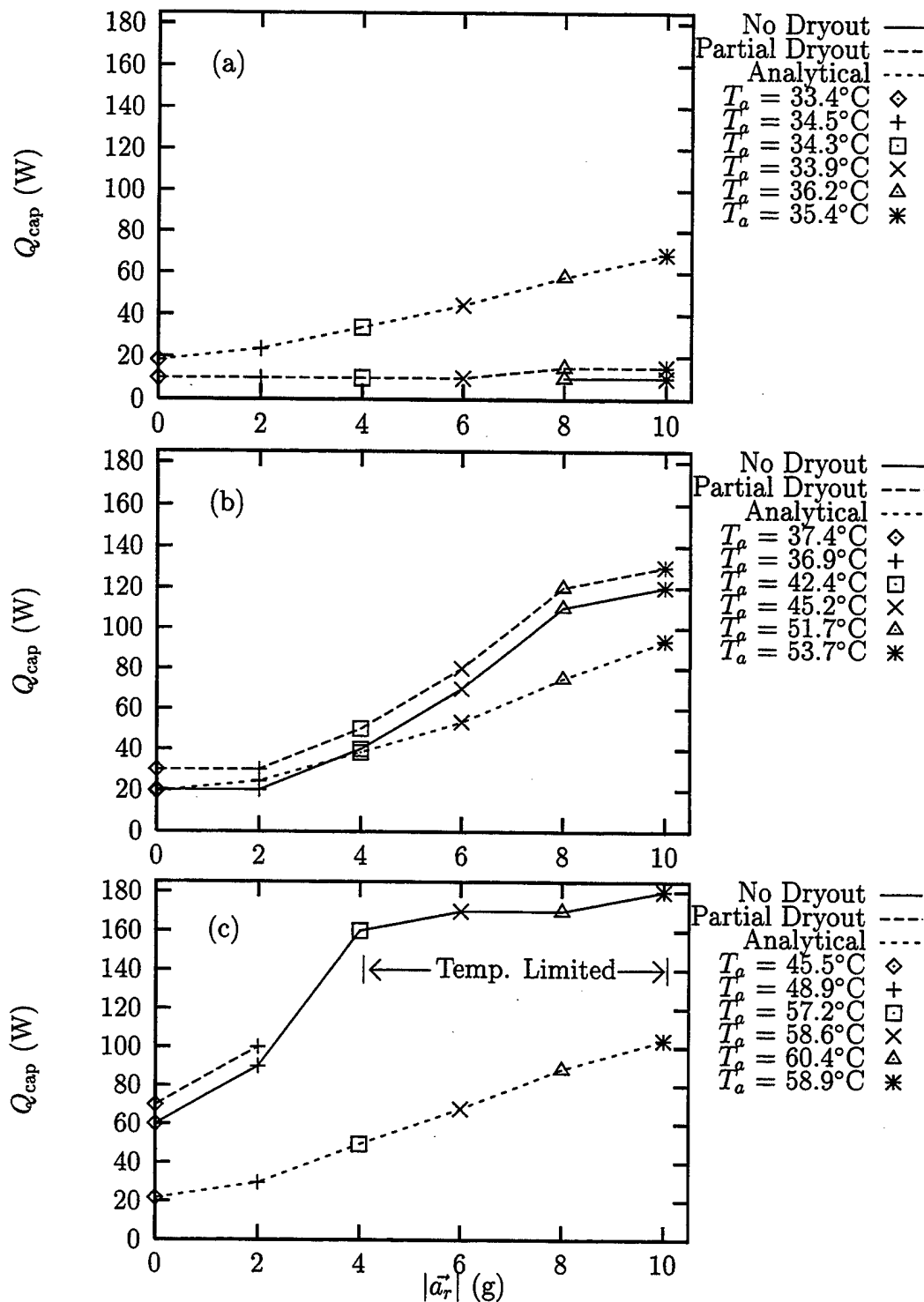
Figure 13: Comparison of present model and experimental capillary limit data versus radial acceleration: (a) $G = 0.5$; (b) $G = 1.0$; (c) $G = 1.5$.

The agreement of the analytical model was very good for $G = 1.0$ as expected. For $G = 0.5$, the model overpredicted the experimental data because it was assumed that the grooves were completely filled. For $G = 1.5$, the model underpredicted the data due to the assumption that no liquid communication occurred between the grooves.

Temperatures within the evaporator section are shown in Figs. 14 and 15 for $|\vec{a}_r| = 0.01$-g and 10.0-g, respectively. In general, the temperatures within the evaporator increased with transported heat. In addition, the wall temperatures decreased with G for a given heat transport due to the fact that more grooves were active. The temperatures along the length of the evaporator section can be tracked by examining the case for $G = 1.0$. Near the evaporator end cap, the temperatures departed those for $G = 1.5$ at approximately $Q_t = 15$ W (Fig. 14(a)). At $x = 92.1$ mm (Fig. 14(b)), this departure was delayed until approximately $Q_t = 25$ W, and at $x = 168$ mm (Fig. 14(d)), the data for $G = 1.0$ and 1.5 were nearly coincident. This behavior shows that the grooves were essentially full near the adiabatic section, and proceeded to dry out closer to the evaporator end cap, as expected. Dryout for the $G = 1.5$ case can be seen in Fig. 14(a) where the temperatures converged to nearly the same value around the circumference. It should be noted that the temperatures around the circumference were relatively uniform for $|\vec{a}_r| = 0.01$-g. Evaporator temperatures for $|\vec{a}_r| = 10.0$-g are shown in Fig. 15. In comparison to $|\vec{a}_r| = 0.01$-g, the evaporator temperatures were in general lower due to the improved pumping ability of the helical grooves under increased radial acceleration. In addition, the temperatures tended to overlap over a greater range of heat transport values. In contrast to $|\vec{a}_r| = 0.01$-g, the evaporator temperature variation was greater around the circumference at higher Q_t, but no pattern was distinguishable in the data.

Local heat transfer coefficient data versus heat transport is shown in Figs. 16 and 17 for $|\vec{a}_r| = 0.01$-g and 10.0-g. Overall, the values for h_e were very low for $G = 0.5$ due to the fact that most of the grooves were dried out. As the percent fill increased from $G = 0.5$ to $G = 1.0$, the heat transfer coefficient increased significantly. For $|\vec{a}_r| = 0.01$-g (Fig. 16), h_e increased and then decreased with transported heat.
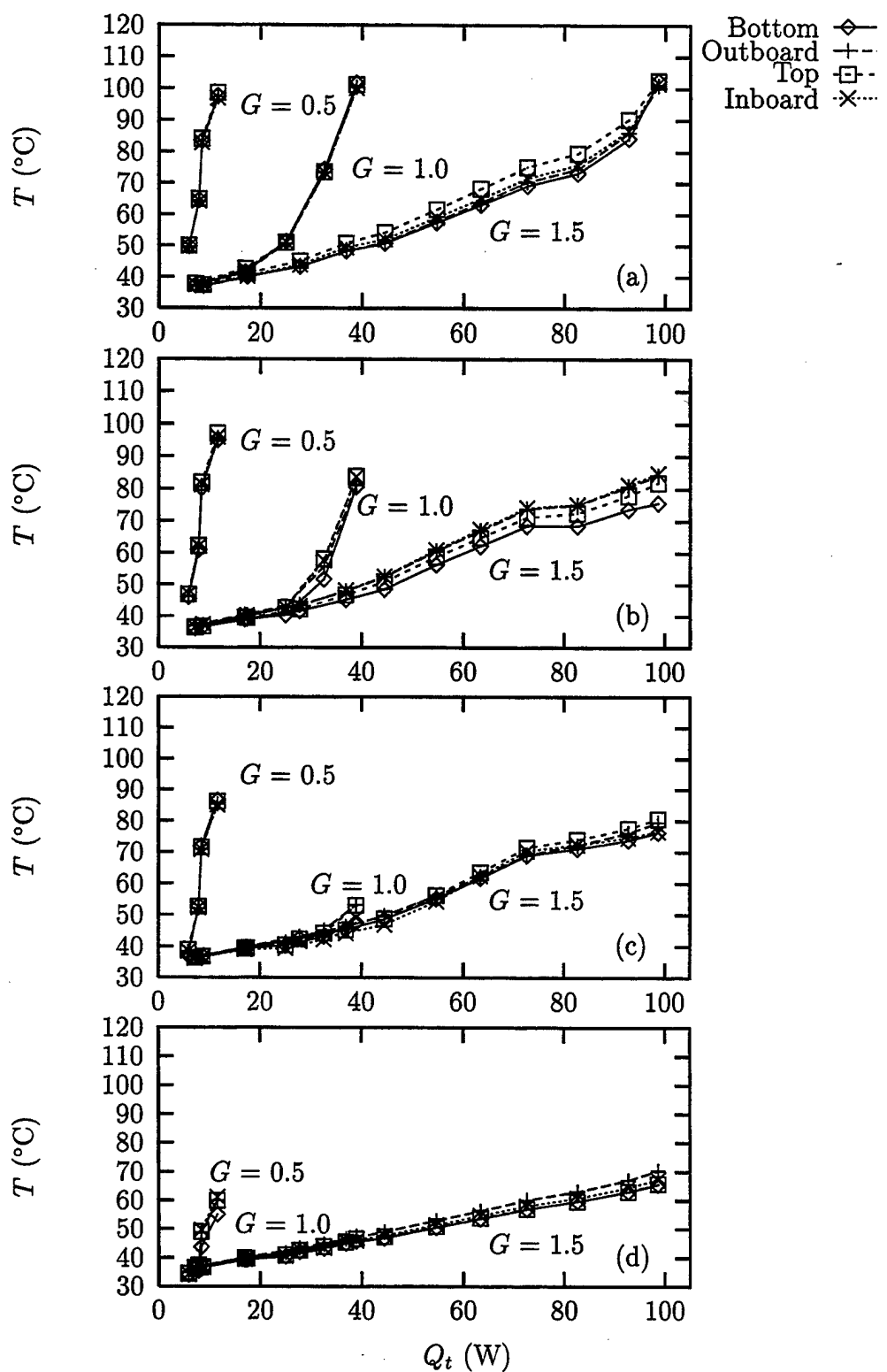
Figure 14: Temperatures within the evaporator section versus transported heat for $|\vec{a}_r| = 0.01$-g: (a) $x = 54.0$ mm; (b) $x = 92.1$ mm; (c) $x = 130$ mm; (d) $x = 168$ mm.
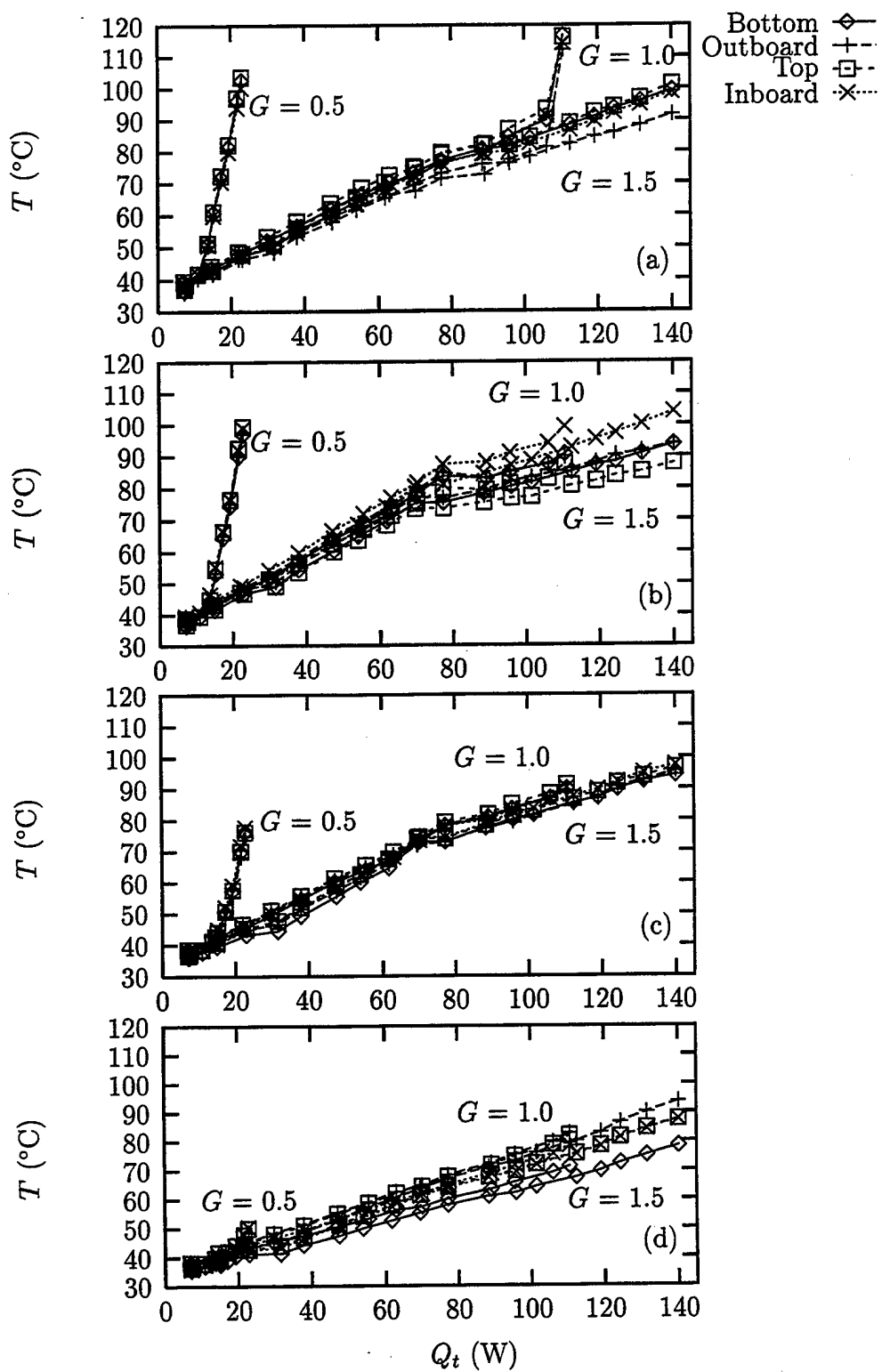
Figure 15: Temperatures within the evaporator section versus transported heat for $|\vec{a}_r| = 10.0$-g: (a) $x = 54.0$ mm; (b) $x = 92.1$ mm; (c) $x = 130$ mm; (d) $x = 168$ mm.

This trend was also reported by Vasiliev et al. (1981) for an aluminum axially–grooved heat pipe with acetone as the working fluid. For $G = 1.0$ and 1.5, the heat transfer coefficient near the evaporator end cap (Fig. 16(a)) decreased until all of the values around the circumference converged. Closer to the adiabatic section, the heat transfer coefficient values around the circumference had not yet converged, showing these portions to still be active. For $|\vec{a}_r| = 10.0$-g (Fig. 17), the values of h_e were significantly more uniform around the circumference and along the axial direction, even during a dryout event ($G = 1.0$, Fig. 17(a)). In addition, the heat transfer coefficient seems to be more constant with respect to the transported heat compared to $|\vec{a}_r| = 0.01$-g. During the experiments, the heat pipe working temperature was not constant, which resulted in changes in the specific volume of the liquid and vapor of the working fluid. Since the heat pipe was filled at room temperature, it was important to quantify the potential effects of the change in volume of liquid in the grooves with temperature. Figure 18 shows the variation of the percentage of groove volume occupied by liquid G with saturation temperature for the three fill amounts over the range of working temperatures seen in the experiments. The maximum percent difference was 2.7%, which was not deemed to be significant.
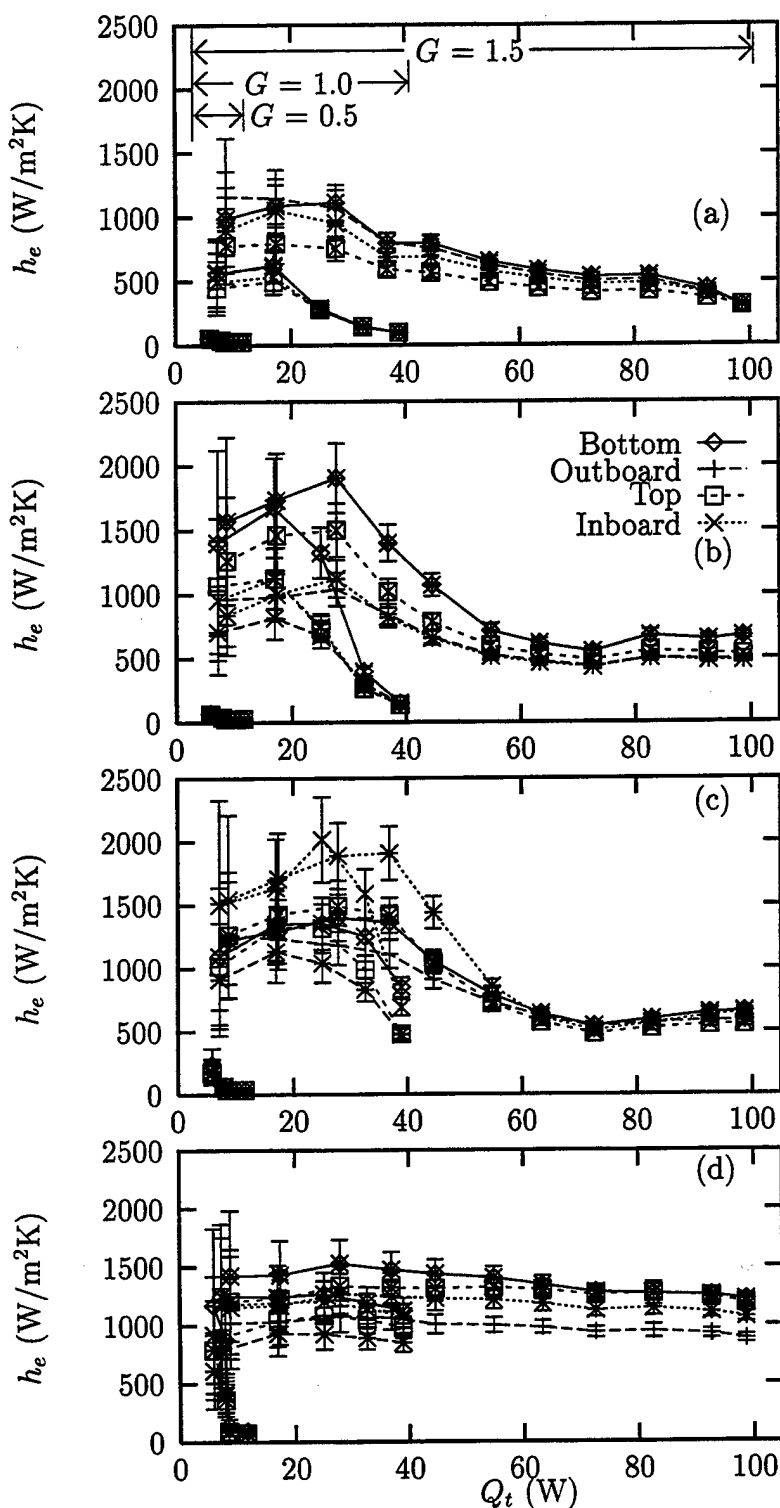
Figure 16: Heat transfer coefficients within the evaporator section versus transported heat for $|\vec{a}_r| = 0.01$-g: (a) $x = 54.0$ mm; (b) $x = 92.1$ mm; (c) $x = 130$ mm; (d) $x = 168$ mm.
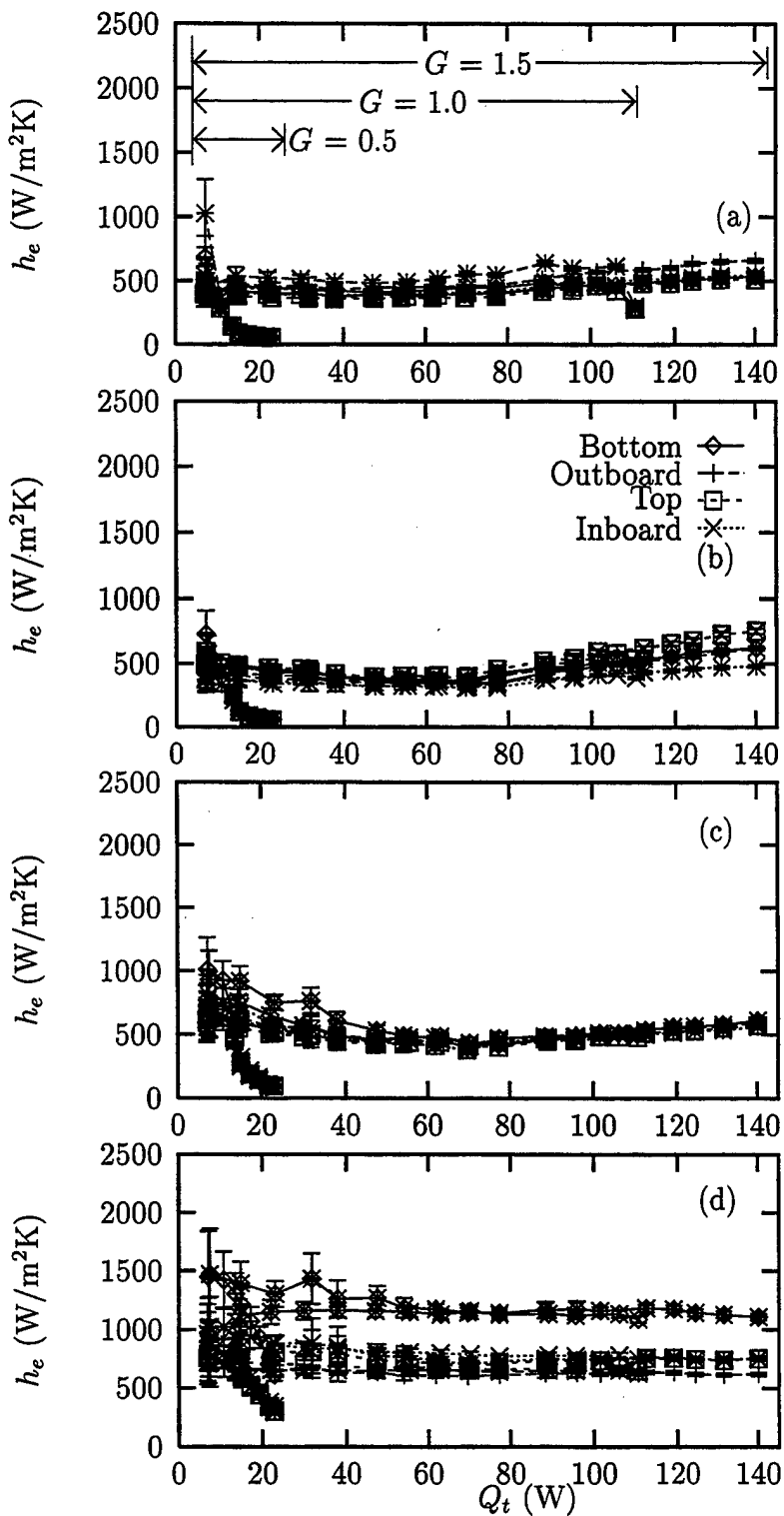
Figure 17: Heat transfer coefficients within the evaporator section versus transported heat for $|\vec{a}_r| = 10.0$-g: (a) $x = 54.0$ mm; (b) $x = 92.1$ mm; (c) $x = 130$ mm; (d) $x = 168$ mm.
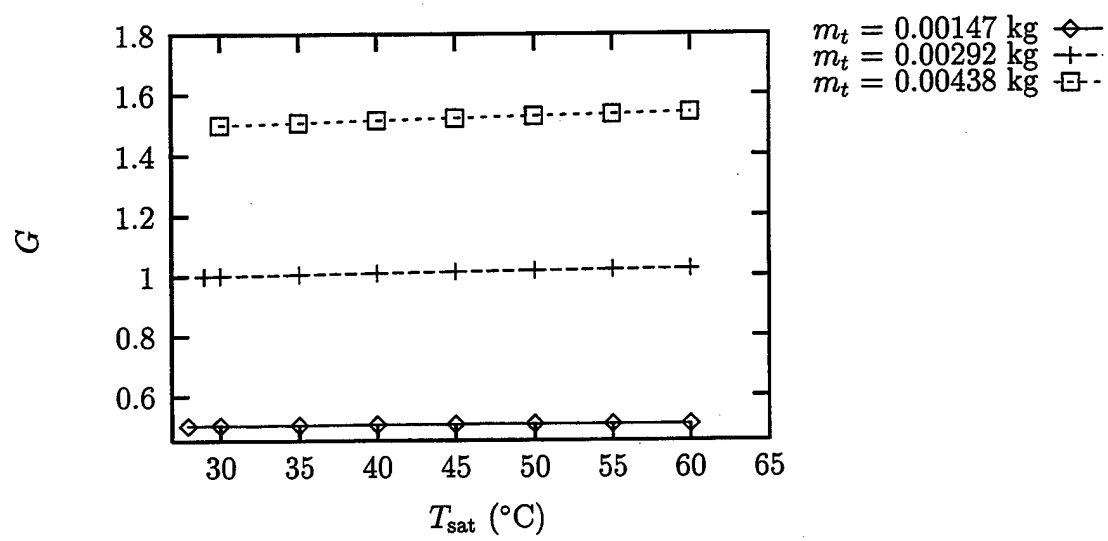
Figure 18: Ratio of liquid volume to total groove volume versus saturation temperature.

7 Conclusions

The effect of fluid inventory on the steady–state performance of a helically–grooved copper–ethanol heat pipe has been examined both experimentally and analytically. It was found that the capillary limit increased and the thermal resistance decreased significantly as the amount of working fluid within the heat pipe increased. In addition, the evaporative heat transfer coefficient was found to be a strong function of the fill amount. The updated analytical model was in very good agreement with the experimental capillary limit results for $G = 1.0$. However, the analytical model overpredicted the capillary limit data for $G = 0.5$ and underpredicted the data for $G = 1.5$.

8 References

ASHRAE, 1977, *Handbook of Fundamentals*, American Society of Heating, Refrigerating and Air–Conditioning Engineers, Inc., Atlanta, GA.

Brennan, P., Kroliczek, E., Jen H., and McIntosh R., 1977, "Axially Grooved Heat Pipes," *AIAA 12th Thermophsics Conf.*, Paper No. 77-747.

Carey, V., 1992, *Liquid-Vapor Phase-Change Phenomena: An Introduction to the Thermophysics of Vaporization and Condensation Processes in Heat Transfer Equipment*, Hemisphere, Washington, D.C.

Chi, S., 1976, *Heat Pipe Theory and Practice: A Sourcebook*, Hemisphere Publ. Corp., New York.

Coleman, H., and Steele, W., 1989, *Experimentation and Uncertainty Analysis for Engineers*, Wiley, New York.

Dunn, P., and Reay, D., 1978, *Heat Pipes*, Pergamon, Oxford.

Faghri, A., 1995, *Heat Pipe Science and Technology*, Taylor and Francis, Washington, D.C.

Ivanovskii, M., Sorokin, V., and Yagodkin, I., 1982, *The Physical Principles of Heat Pipes*, Clarendon, Oxford.

Klasing, K., Thomas, S., and Yerkes, K., 1999, "Prediction of the Operating Limits of Revolving Helically–Grooved Heat Pipes," *ASME Journal of Heat Transfer*, Vol. 121, pp. 213–217.

Lide, D., and Kehiaian, H., 1994, *CRC Handbook of Thermophysical and Thermochemical Data*, CRC Press, Boca Raton, FL.

Miller, R., 1989, *Flow Measurement Engineering Handbook*, 2nd Edn., McGraw-Hill.

Peterson, G., 1994, *An Introduction to Heat Pipes: Modeling, Testing, and Applications*, Wiley, New York.

Schlunder, E., 1983, *Heat Exchanger Design Handbook*, Hemisphere, Washington, D.C.

Shah, R., 1975, "Laminar Flow Friction and Forced Convection Heat Transfer in

Ducts of Arbitrary Geometry," *International Journal of Heat and Mass Transfer*, Vol. 18, pp. 849-862.

Shah, R. K., and Bhatti, M. S., 1987, "Laminar Convection Heat Transfer in Dusts," in: *Handbook of Single-Phase Convective Heat Transfer*, Kakac, S., Shah, R., K., and Aung, W., eds., Wiley, New York.

Thomas, S., Klasing, K., and Yerkes, K., 1998, "The Effects of Transverse Acceleration Induced Body Forces on the Capillary Limit of Helically–Grooved Heat Pipes," *ASME Journal of Heat Transfer*, Vol. 120, pp. 441–451.

Thomas, S., Lykins, R., and Yerkes, K., 1999, "Friction Factors for Fully-Developed Laminar Flow in Trapezoidal Grooves with Shear Stress at the Free Surface," to be submitted to *ASME J. Fluids Engineering*.

Timmermans, J., 1950, *Physico-Chemical Constants of Pure Organic Compounds*, Elsevier, New York.

TRC, 1985, *TRC Thermodynamic Tables—Non-hydrocarbons*, Thermodynamic Research Center: The Texas A & M University System, College Station, TX (Looseleaf data sheets).

Vargaftik, N., 1975, *Handbook of Physical Properties of Liquids and Gases*, Hemisphere, Washington, D.C.

Vasiliev, L., Grakovich L., and Khrustalev D., 1981, "Low–Temperature Axially Grooved Heat Pipes," *Proc. 4th Int. Heat Pipe Conf.*, London, pp. 337–348.

9 Appendices

9.1 Heat Pipe Filling Station Operating Procedure

In this section, the procedure for filling a heat pipe is outlined. Table 14 shows the valving sequence during a typical filling procedure. Prior to filling, the heat pipe container was evacuated for 24 hr using a turbomolecular vacuum pump to a pressure of 10^{-6} Torr. The evacuated heat pipe was then installed onto the filling station at valve 5.

1. Close all valves.

2. Fill the working fluid reservoir with 500 ml of fluid and remove any noncondensable gas from the fluid by the freeze/thaw method. Prior to handling LN$_2$, read the Material Safety Data Sheet (MSDS), and wear protective clothing and goggles.

    (a) Fill the LN$_2$ dewar. Connect a vacuum line from the manifold drain plug port to valve 3.

    (b) Slowly raise the LN$_2$ dewar with the lab jack until the working fluid reservoir is partially submerged to freeze the working fluid. The pressure read by the vacuum gage will be less than 100 μmHg when the ethanol freezes.

    (c) Open and then close valves 3 and 7 for 10 min. to clear the reservoir of noncondensable gases. Lower the LN$_2$ dewar to thaw the working fluid.

    (d) Repeat steps 2(b) and 2(c) at least three times.

3. Remove the air from the fill station manifold and heat pipe fill valve stem.

    (a) Install the manifold drain plug and the evacuated heat pipe on the fill station.

    (b) Open valves 2, 5, 6 and 7. Evacuate the system for 20 minutes (Manifold pressure $\leq$ 60 μm).

4. Fill the manifold and dispensing burette completely with fluid.

   (a) Isolate the manifold from the vacuum source by closing valves 6 and 7.

   (b) Slowly open valve 4 to draw fluid into the dispensing burette.

   (c) If necessary, pressurize the fluid reservoir by attaching the GN_2 feed line to valve 3.

   (d) Open the valve on the GN_2 cylinder and adjust the regulated pressure of the feed line to less than 10 psig.

   (e) Open valve 3 and slowly open and close valve 1 to completely fill the dispensing burette with fluid. Vapor above the fluid will be vented to atmosphere.

   (f) First close valve 4, then close valve 3 and the valve on the GN_2 cylinder.

5. Purge the manifold of vapor bubbles by pressurizing the fluid in the dispensing burette using the GN_2 feed line attached to the pressure gage (dashed line in Fig. 6).

   (a) Open the valve on the GN_2 cylinder and adjust the pressure to less than 5 psig (GN_2 will escape from the 1 psig pressure relief valve). Open valve 1 and remove the manifold drain plug.

   (b) Open and then close valve 6 to drain down the fluid to the first graduation mark on the dispensing burette. Fluid will appear at the manifold drain.

   (c) Close valve 2 and note the change in the fluid meniscus level when opening and closing the pressure relief valve.

   (d) Open valve 2 and again note the change in the meniscus level when opening and closing the pressure relief valve. If there is a significant difference between the change found in steps 5(c) and 5(d), the presence of trapped vapor bubbles in the manifold is indicated.

(e) Close and open valves 2 and 5 several times while cycling the the pressure relief valve to remove any trapped vapor bubbles within these valves. The volume displaced by each valve (without trapped vapor) is 0.06 ml. Valves 2 and 5 must be open at the end of this sub-process.

6. Dispense the working fluid into the heat pipe.

   (a) Record the dispensing burette meniscus level.

   (b) Slowly open and then close valve 8 (heat pipe fill valve) to meter in the desired volume of fluid into the heat pipe by noting the drop in the meniscus level.

   (c) Again record the dispensing burette meniscus level.

   (d) Close valve 5 and remove the filled heat pipe.

7. Purge the filling station of working fluid.

   (a) Open valve 3 to atmosphere and then slowly open valve 4 to purge the unused fluid in the dispensing burette back into the fluid reservoir.

   (b) Close valve 4 and then valve 3, and remove the working fluid reservoir from the filling station at valve 4.

   (c) Open valves 4, 5 and 6 to allow the GN_2 to evaporate any remaining working fluid within the filling station.

   (d) Once the manifold is dry, close the valve on the GN_2 cylinder, then close valves 1, 4, 5, and 6 and install the manifold drain plug.

Table 14: Flow chart for fill station operating procedure (O = Open, C = Closed, OC = Open then Close, CO = Close then Open).

Step	Valve								M.D.P.	GN$_2$	P.R.V.
	1	2	3	4	5	6	7	8			
1	C	C	C	C	C	C	C	C	O	C	C
2a	C	C	C	C	C	C	C	C	O	C	C
2b	C	C	C	C	C	C	C	C	O	C	C
2c	C	C	OC	C	C	C	OC	C	O	C	C
3a	C	C	C	C	C	C	C	C	C	C	C
3b	C	O	C	C	O	O	O	C	C	C	C
4a	C	O	C	C	O	C	C	C	C	C	C
4b	C	O	C	O	O	C	C	C	C	C	C
4c	C	O	C	O	O	C	C	C	C	C	C
4d	C	O	C	O	O	C	C	C	C	O	C
4e	OC	O	O	O	O	C	C	C	C	O	C
4f	C	O	C	C	O	C	C	C	C	C	C
5a	O	O	C	C	O	C	C	C	O	O	C
5b	O	O	C	C	O	OC	C	C	O	O	C
5c	O	C	C	C	O	C	C	C	O	O	OC
5d	O	O	C	C	O	C	C	C	O	O	OC
5e	O	CO	C	C	CO	C	C	C	O	O	OC
6a	O	O	C	C	O	C	C	C	O	O	C
6b	O	O	C	C	O	C	C	OC	O	O	C
6c	O	O	C	C	O	C	C	C	O	O	C
6d	O	O	C	C	C	C	C	C	O	O.	C
7a	O	O	O	O	C	C	C	C	O	O	C
7b	O	O	C	C	C	C	C	C	O	O	C
7c	O	O	C	O	O	O	C	C	O	O	C
7d	C	O	C	C	C	C	C	C	C	C	C

52

9.2 Thermocouple Calibration Procedure

The thermocouples used in the present experiment were calibrated from 20 to 100°C in increments of 10°C with a Hart Scientific (Model 5691) NIST-Traceable resistance temperature detector (RTD) and a low-dead band ($\pm$ 0.01°C) Brinkmann (Model RC20) recirculating bath. The thermocouples were mounted to the RTD probe and submerged into the recirculating bath. The recirculation of the bath oil (Brayco micronic 889) caused significant temperature gradients throughout the bath. To address this problem a small can was submerged in the bath and the RTD/thermocouple bundle was placed inside the can. Electrical noise was found to be present in the test cell where the thermocouples were calibrated, as shown in Fig. 19(a). To address this problem the data was averaged every 10 s over the entire sampling interval. Figure 19(b) shows a typical averaged data set taken at a setpoint temperature of 90°C for 3.5 hr, where the uncertainty of the readings has been significantly reduced. Even though the averaged data was relatively constant, the recirculating bath was stabilized for 2 hr before data was taken at each setpoint temperature to ensure that steady–state conditions had been reached.

Since some of the thermocouples were switched by relays, a test was performed in order to ensure that switching the relays on and off did not affect the thermocouple readings. The test consisted of starting the data acquisition and waiting 1 min., switching the relays to the on position and waiting 15 min., then switching the relays to the off position and waiting 15 min. The result of the test showed there was no significant change in the temperature with time for any of the thermocouples. A series of tests was also performed on the thermocouple relays to determine the effect the relay contacts had on the thermocouple output temperature. Some of the tests consisted of blowing hot and cold air across the relay contacts. The results of these tests showed that the relays had to be insulated and covered with a box to keep the convective heat losses to a minimum while the centrifuge table was spinning.

The following is the procedure used in the calibration process.

53
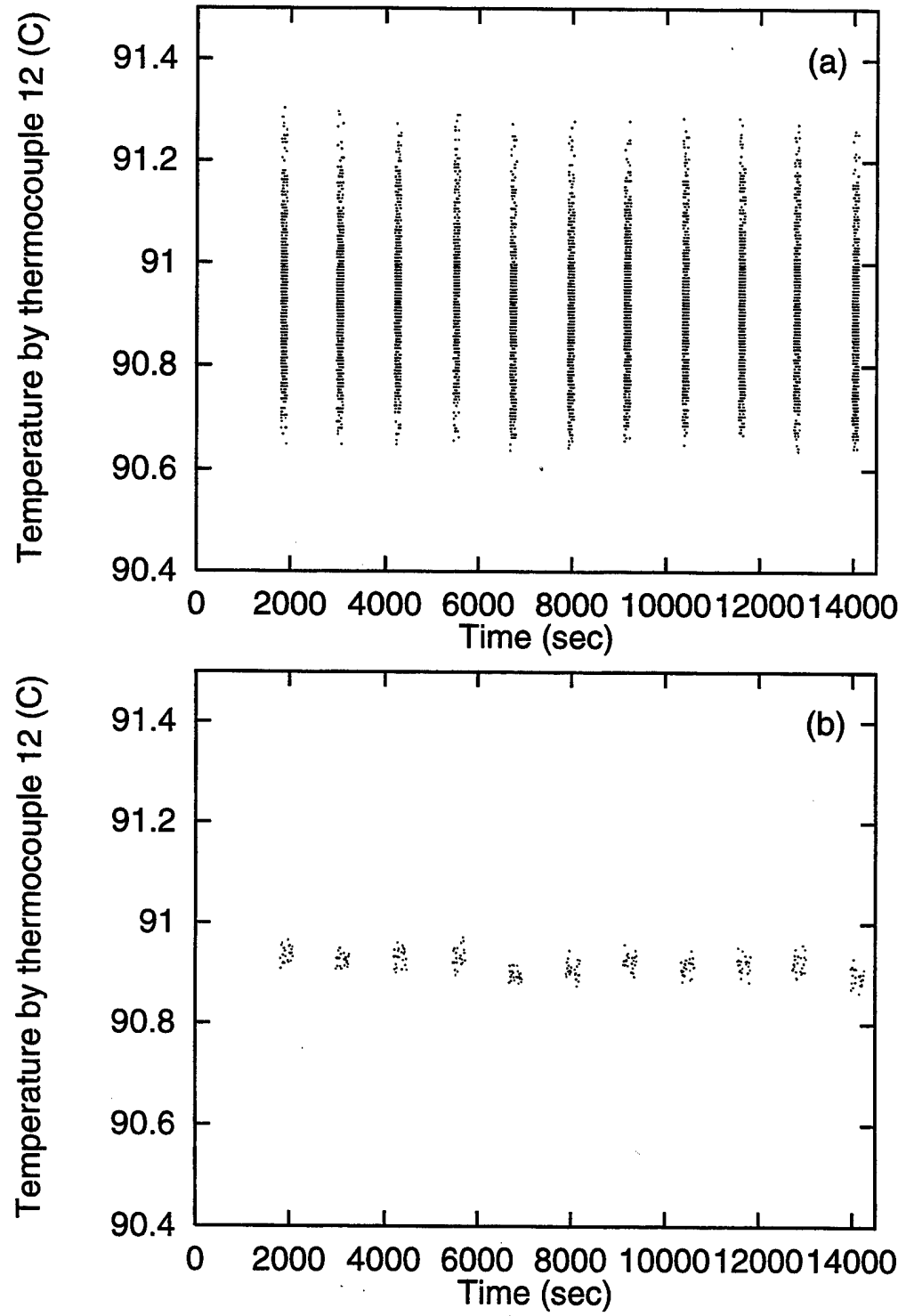
Figure 19: Calibration of thermocouple 11 at 90°C: (*a*) Raw data; (*b*) Averaged data.

1. Prepare the thermocouple coils to match the conditions during testing by ensuring they are insulated and all covers are in place.

2. Mount all of the thermocouples (including the calorimeter thermocouples) onto the RTD probe as close to the sensing portion as possible.

3. Place the RTD/thermocouple bundle vertically into the recirculating bath with a laboratory stand. Submerge the bundle as far as possible without the RTD or any of the thermocouples touching the bottom or sides of the recirculating bath.

4. Turn on the recirculating bath and adjust the setpoint to 20°C.

5. Turn on the centrifuge table power.

6. Turn on the RTD computer and initiate the program associated with the RTD.

7. Turn on the control room electronics and thermocouple data acquisition program Viewdac.

8. Place the thermocouple coil switch in the OFF position.

9. Open Viewdac sequences calibrat.beq and calibrw1.beq.

10. Use calibrat.beq to monitor the bath temperature and calibrw1.beq to write data to a file.

11. Ensure that the sample rate is set to 10 Hz and the output file name has proper identification for the thermocouple coil switch in the OFF position.

12. Start the data acquisition loop and run for 120 s.

13. Record an RTD value manually every ten seconds while the data acquisition loop is running.

14. Change the output file name to denote that the thermocouple coil switch is in the ON position.

15. Switch the thermocouple coil switch to the ON position. Wait ten seconds to ensure coil stability.

16. Start the data acquisition loop and run for 120 s.

17. Record an RTD value manually every ten seconds while the data acquisition loop is running.

18. Switch the thermocouple coil switch to the OFF position.

19. Advance the recirculating bath to the next setpoint temperature.

20. Repeat steps 12-19 for the next setpoint.

Coefficients for the linear curve fit for each thermocouple are given in Table 15 for the range $20°C \leq T_{\text{reading}} \leq 100°$.

$$T_{\text{actual}} = \alpha_0 + \alpha_1 T_{\text{reading}} \pm \epsilon \tag{36}$$

Using the standard error given by Coleman and Steele (1989), the uncertainty associated with each of the thermocouple calibration equations is

$$\epsilon = \sqrt{\sum_{i=1}^{n} \frac{(T_{\text{actual}(i)} - T_{\text{reading}(i)})^2}{n - 2}} \tag{37}$$

Table 15: Coefficients for thermocouple calibration.

Thermocouple	α_0	α_1	ϵ	Data Acquisition Channel
Coolant Inlet (11)	-0.4620302	0.9999193	0.0699	TC3
Coolant Outlet (12)	-0.8748547	0.9996509	0.0841	TC4
1–Inboard	-0.0521081	0.9959866	0.0732	TC0
2–Inboard	-0.2641292	1.0001844	0.0800	TC5
3–Inboard	-0.8430881	1.0003875	0.0760	TC6
4–Inboard	-0.5082865	0.9970537	0.0736	TC7
5–Inboard	-0.3317360	0.9991215	0.0702	TC8
6–Inboard	-0.5198530	0.9961772	0.0828	TC13
8–Inboard	-0.3119424	0.9961133	0.0732	TC14
10–Inboard	-0.6501503	0.9965431	0.0686	TC2
1–Outboard	-0.5721585	0.9959817	0.0776	TC1
2–Outboard	-0.1469691	0.9960199	0.0800	TC5
3–Outboard	-0.8401706	1.0008819	0.0769	TC6
4–Outboard	-0.4942304	0.9970113	0.0699	TC7
5–Outboard	-0.3201927	0.9992546	0.0748	TC8
7–Outboard	-0.5018720	0.9960913	0.0816	TC13
9–Outboard	-0.2943188	0.9959160	0.0750	TC14
10–Outboard	0.2829758	0.9946570	0.0738	TC15
2–Top	-0.5137903	1.0005327	0.1341	TC9
3–Top	-0.2518604	1.0001036	0.0759	TC10
4–Top	-0.3904948	1.0013209	0.0656	TC11
5–Top	0.4147904	0.9950726	0.0649	TC12
2–Bottom	-0.5077360	1.0004865	0.0661	TC9
3–Bottom	-0.2490069	1.0000940	0.0710	TC10
4–Bottom	-0.4025206	1.0014220	0.0686	TC11
5–Bottom	0.4148459	0.9951285	0.0652	TC12

9.3 Calculated Experimental data

Table 16: Evaporative heat transfer coefficient (W/m^{2}K) for thermocouple 2, $G = 0.5$ and $a_r = 0.01$-g.

Q_{in} (W)	Bottom		Outboard		Top		Inboard	
	h_e	Δh_e	h_e	Δh_e	h_e	Δh_e	h_e	Δh_e
11.254	54.580	28.492	55.396	28.921	53.971	28.184	54.737	28.577
15.494	39.413	15.219	39.808	15.374	38.956	15.044	39.832	15.382
20.777	26.511	9.834	26.653	9.888	26.141	9.698	26.821	9.950
25.045	28.554	7.966	28.740	8.018	28.158	7.856	28.896	8.062

Table 17: Evaporative heat transfer coefficient (W/m^{2}K) for thermocouple 3, $G = 0.5$ and $a_r = 0.01$-g.

Q_{in} (W)	Bottom		Outboard		Top		Inboard	
	h_e	Δh_e	h_e	Δh_e	h_e	Δh_e	h_e	Δh_e
11.254	71.586	37.373	69.625	36.352	66.707	34.826	66.082	34.500
15.494	44.767	17.288	43.907	16.956	42.730	16.502	42.918	16.575
20.777	28.368	10.523	28.054	10.407	27.366	10.152	27.679	10.268
25.045	29.829	8.322	29.567	8.249	28.894	8.061	29.349	8.188

Table 18: Evaporative heat transfer coefficient (W/m^{2}K) for thermocouple 4, $G = 0.5$ and $a_r = 0.01$-g.

Q_{in} (W)	Bottom		Outboard		Top		Inboard	
	h_e	Δh_e	h_e	Δh_e	h_e	Δh_e	h_e	Δh_e
11.254	238.999	125.195	184.815	96.720	165.971	86.843	178.979	93.557
15.494	64.490	24.907	66.693	25.761	64.852	25.047	66.219	25.576
20.777	34.800	12.910	35.683	13.238	35.033	12.996	35.804	13.282
25.045	34.787	9.705	35.581	9.926	35.051	9.778	35.799	9.987

Table 19: Evaporative heat transfer coefficient (W/m²K) for thermocouple 5, $G = 0.5$ and $a_r = 0.01$-g.

Q_{in}	Bottom		Outboard		Top		Inboard	
	h_e	Δh_e	h_e	Δh_e	h_e	Δh_e	h_e	Δh_e
11.254	1168.919	660.165	611.749	328.146	788.292	423.748	920.380	501.517
15.494	876.782	350.646	400.343	155.831	359.535	139.983	423.567	165.301
20.777	143.245	53.186	92.298	34.257	90.234	33.488	86.543	32.119
25.045	90.659	25.309	72.417	20.210	72.585	20.254	69.268	19.328

Table 20: Evaporative heat transfer coefficient (W/m²K) for thermocouple 2, $G = 1.0$ and $a_r = 0.01$-g.

Q_{in} (W)	Bottom		Outboard		Top		Inboard	
	h_e	Δh_e	h_e	Δh_e	h_e	Δh_e	h_e	Δh_e
10.903	557.26	257.17	568.41	265.15	447.73	208.51	495.04	227.19
21.176	622.95	124.73	608.62	122.12	498.53	100.61	532.93	107.02
30.494	277.81	37.22	290.38	38.93	283.36	38.11	283.08	38.04
40.053	142.35	14.75	146.50	15.19	145.46	15.10	146.53	15.20
49.903	98.09	8.82	100.06	9.00	98.77	8.89	100.47	9.04

Table 21: Evaporative heat transfer coefficient (W/m²K) for thermocouple 3, $G = 1.0$ and $a_r = 0.01$-g.

Q_{in} (W)	Bottom		Outboard		Top		Inboard	
	h_e	Δh_e	h_e	Δh_e	h_e	Δh_e	h_e	Δh_e
10.903	1402.98	718.49	704.90	328.73	1067.54	525.04	955.67	468.29
21.176	1674.12	382.68	816.53	166.82	1124.19	236.99	1127.08	236.72
30.494	1325.08	197.80	676.35	94.98	731.00	101.10	746.43	103.95
40.053	397.60	42.54	301.54	31.38	263.87	27.41	270.45	28.16
49.903	149.08	13.43	147.24	13.26	138.36	12.45	138.49	12.46

Table 22: Evaporative heat transfer coefficient (W/m²K) for thermocouple 4, $G = 1.0$ and $a_r = 0.01$-g.

Q_{in} (W)	Bottom		Outboard		Top		Inboard	
	h_e	Δh_e	h_e	Δh_e	h_e	Δh_e	h_e	Δh_e
10.903	1095.94	542.02	911.73	444.91	1018.26	496.46	1499.84	826.94
21.176	1347.75	287.24	1131.17	241.54	1325.19	289.71	1634.73	383.83
30.494	1354.52	207.02	1038.21	152.70	1315.68	192.11	2015.83	337.37
40.053	1248.87	146.83	827.96	90.11	987.30	106.86	1588.34	194.26
49.903	847.62	79.50	472.47	43.12	477.35	43.42	687.18	64.25

Table 23: Evaporative heat transfer coefficient (W/m²K) for thermocouple 5, $G = 1.0$ and $a_r = 0.01$-g.

Q_{in}	Bottom		Outboard		Top		Inboard	
	h_e	Δh_e	h_e	Δh_e	h_e	Δh_e	h_e	Δh_e
10.903	1248.05	618.59	785.68	374.66	894.79	423.76	1174.16	578.17
21.176	1239.50	271.27	928.74	191.37	1035.20	220.32	1191.51	255.87
30.494	1265.95	184.38	921.92	128.64	1083.38	154.07	1204.23	174.67
40.053	1192.77	132.43	887.30	97.74	1043.66	114.21	1140.45	127.81
49.903	1122.63	111.39	849.51	80.00	980.95	93.10	1076.25	103.55

Table 24: Evaporative heat transfer coefficient (W/m²K) for thermocouple 2, $G = 1.5$ and $a_r = 0.01$-g.

Q_{in} (W)	Bottom		Outboard		Top		Inboard	
	h_e	Δh_e	h_e	Δh_e	h_e	Δh_e	h_e	Δh_e
10.124	987.10	368.44	1158.46	454.97	775.69	292.30	898.09	333.98
20.024	1087.67	211.23	1145.94	220.74	793.58	155.27	1051.70	199.72
29.462	1111.74	139.05	1071.60	139.10	755.35	93.65	953.77	117.78
39.808	797.77	74.96	801.47	75.54	590.46	55.47	687.69	65.10
50.142	794.32	63.26	760.30	61.05	565.05	44.28	688.77	54.91
60.577	652.89	40.23	629.16	38.99	492.30	30.22	579.27	35.67
69.754	584.59	31.87	557.57	30.82	447.73	24.40	521.71	28.12
80.619	532.34	24.67	502.15	23.21	414.04	18.86	476.34	21.84
89.645	540.57	31.18	511.88	26.50	425.64	20.38	484.42	23.32
101.692	438.04	18.83	414.05	16.97	369.07	14.88	405.92	16.73
110.802	307.01	11.75	316.84	12.21	307.40	12.03	312.52	12.19

Table 25: Evaporative heat transfer coefficient (W/m²K) for thermocouple 3, $G = 1.5$ and $a_r = 0.01$-g.

Q_{in} (W)	Bottom		Outboard		Top		Inboard	
	h_e	Δh_e	h_e	Δh_e	h_e	Δh_e	h_e	Δh_e
10.124	1569.96	650.12	964.54	365.12	1262.58	497.12	836.24	307.83
20.024	1730.98	364.55	978.85	185.45	1460.90	292.27	999.40	188.77
29.462	1904.73	271.33	1039.95	130.69	1500.52	207.76	1124.41	145.53
39.808	1401.40	141.25	843.85	80.73	1020.95	98.50	819.04	77.93
50.142	1071.25	89.56	663.19	52.30	782.14	61.31	656.62	52.28
60.577	714.24	52.92	526.12	32.67	592.79	37.20	513.79	32.27
69.754	615.53	38.50	473.85	25.41	528.96	28.88	464.91	26.22
80.619	549.94	28.33	435.76	19.89	485.00	22.76	429.34	20.16
89.645	673.87	45.70	498.63	25.10	557.01	27.56	499.08	24.48
101.692	645.42	31.70	488.83	19.92	539.80	21.97	481.49	20.35
110.802	671.19	26.74	488.41	18.63	526.78	20.82	479.25	18.37

Table 26: Evaporative heat transfer coefficient (W/m²K) for thermocouple 4, $G = 1.5$ and $a_r = 0.01$-g.

Q_{in} (W)	Bottom		Outboard		Top		Inboard	
	h_e	Δh_e	h_e	Δh_e	h_e	Δh_e	h_e	Δh_e
10.124	1224.23	462.42	1264.21	497.76	1264.24	496.80	1542.33	666.10
20.024	1293.35	251.80	1230.76	240.52	1425.45	288.04	1705.03	362.79
29.462	1399.15	182.91	1181.53	154.20	1489.83	201.69	1887.88	260.32
39.808	1361.70	133.50	1108.98	111.61	1416.39	138.90	1906.83	213.24
50.142	1054.00	86.27	909.67	74.72	1037.44	83.96	1438.24	127.36
60.577	789.57	50.43	728.30	45.64	720.66	45.25	855.04	55.53
69.754	637.53	34.65	617.56	33.72	570.07	30.73	607.55	33.45
80.619	538.84	24.57	532.37	24.19	480.59	21.84	504.22	23.15
89.645	592.38	34.37	566.40	31.23	523.88	24.94	560.89	26.98
101.692	644.04	26.66	582.55	23.70	550.08	22.21	620.25	25.05
110.802	655.10	25.51	575.90	22.24	552.01	21.55	646.52	25.14

Table 27: Evaporative heat transfer coefficient (W/m^{2}K) for thermocouple 5, $G = 1.5$ and $a_r = 0.01$-g.

Q_{in}	Bottom		Outboard		Top		Inboard	
	h_e	Δh_e	h_e	Δh_e	h_e	Δh_e	h_e	Δh_e
10.124	1423.07	558.67	1020.07	387.25	1204.81	446.64	1153.26	438.56
20.024	1429.74	294.15	1029.79	194.38	1228.68	237.18	1169.01	223.53
29.462	1529.28	202.36	1076.75	136.47	1334.65	169.72	1270.90	171.02
39.808	1473.39	151.58	1062.05	102.57	1317.64	131.96	1244.51	124.90
50.142	1438.23	121.63	1005.13	82.04	1315.64	110.07	1227.82	103.50
60.577	1406.21	92.16	999.43	63.90	1323.38	84.83	1217.49	78.82
69.754	1343.67	78.73	979.77	56.17	1302.39	79.85	1182.23	67.16
80.619	1280.96	61.52	936.75	44.49	1258.37	60.98	1126.54	55.41
89.645	1267.80	97.98	946.49	57.78	1272.85	70.92	1144.84	62.87
101.692	1256.42	56.34	923.74	40.20	1245.94	54.98	1109.64	48.05
110.802	1217.01	49.54	880.04	35.06	1187.86	49.08	1067.51	43.48

Table 28: Evaporative heat transfer coefficient (W/m^{2}K) for thermocouple 2, $G = 0.5$ and $a_r = 10.0$-g.

Q_{in} (W)	Bottom		Outboard		Top		Inboard	
	h_e	Δh_e	h_e	Δh_e	h_e	Δh_e	h_e	Δh_e
10.735	682.76	165.96	1025.69	265.59	490.96	120.62	536.97	129.68
15.694	301.40	45.61	362.46	55.12	285.47	43.55	285.80	43.27
20.869	145.74	17.47	150.93	18.10	143.81	17.28	148.24	17.78
25.298	92.57	9.95	94.88	10.20	91.42	9.84	95.73	10.29
29.973	75.60	8.12	77.05	8.28	74.53	8.01	78.44	8.42
33.634	67.16	6.20	68.27	6.31	66.15	6.11	69.73	6.44
40.170	57.52	4.57	58.31	4.63	56.53	4.49	59.55	4.73
43.285	54.98	4.27	55.70	4.32	54.03	4.20	57.00	4.42

Table 29: Evaporative heat transfer coefficient (W/m^{2}K) for thermocouple 3, $G = 0.5$ and $a_r = 10.0$-g.

Q_{in} (W)	Bottom		Outboard		Top		Inboard	
	h_e	Δh_e	h_e	Δh_e	h_e	Δh_e	h_e	Δh_e
10.735	729.30	177.96	579.12	139.84	594.26	143.66	408.87	97.52
15.694	494.05	75.69	460.59	70.54	467.42	71.60	337.05	51.15
20.869	273.24	32.90	270.51	32.63	256.09	30.85	211.73	25.44
25.298	132.83	14.30	131.63	14.17	122.51	13.18	118.44	12.74
29.973	95.08	10.21	93.22	10.01	89.24	9.59	89.08	9.57
33.634	79.63	7.36	78.11	7.22	75.60	6.99	75.95	7.02
40.170	64.03	5.09	63.25	5.03	61.24	4.87	61.80	4.91
43.285	60.19	4.67	59.76	4.64	57.84	4.49	58.38	4.53

Table 30: Evaporative heat transfer coefficient (W/m^{2}K) for thermocouple 4, $G = 0.5$ and $a_r = 10.0$-g.

Q_{in} (W)	Bottom		Outboard		Top		Inboard	
	h_e	Δh_e	h_e	Δh_e	h_e	Δh_e	h_e	Δh_e
10.735	1009.38	254.97	774.51	190.40	663.68	160.52	722.99	177.73
15.694	927.33	148.84	746.73	117.68	627.76	96.92	625.27	97.00
20.869	597.21	73.70	559.62	69.15	472.33	57.68	443.86	54.21
25.298	285.69	30.89	319.74	34.61	276.29	29.85	251.44	27.18
29.973	192.06	20.66	217.31	23.44	189.07	20.34	173.24	18.64
33.634	148.04	13.72	163.74	15.20	146.44	13.56	136.30	12.61
40.170	104.50	8.31	110.33	8.78	104.12	8.28	99.23	7.89
43.285	93.07	7.23	96.69	7.52	93.44	7.26	89.86	6.98

Table 31: Evaporative heat transfer coefficient (W/m²K) for thermocouple 5, $G = 0.5$ and $a_r = 10.0$-g.

Q_{in}	Bottom		Outboard		Top		Inboard	
	h_e	Δh_e	h_e	Δh_e	h_e	Δh_e	h_e	Δh_e
10.735	1449.55	389.00	718.06	175.87	791.29	193.52	1013.29	255.47
15.694	1420.43	243.46	706.20	111.30	793.12	124.44	1022.27	166.40
20.869	1303.71	176.15	646.04	80.39	728.23	90.61	929.43	119.49
25.298	1212.23	143.81	571.96	63.33	596.50	65.71	752.26	84.39
29.973	1070.29	122.33	514.38	56.14	509.36	55.39	597.14	65.51
33.634	933.94	90.74	462.22	43.36	441.42	41.26	483.14	45.29
40.170	704.61	57.83	381.32	30.60	344.25	27.57	338.41	27.15
43.285	611.42	48.80	344.56	27.03	305.34	23.87	295.44	23.15

Table 32: Evaporative heat transfer coefficient (W/m²K) for thermocouple 2, $G = 1.0$ and $a_r = 10.0$-g.

Q_{in} (W)	Bottom		Outboard		Top		Inboard	
	h_e	Δh_e	h_e	Δh_e	h_e	Δh_e	h_e	Δh_e
10.966	391.52	98.43	439.49	111.33	402.45	103.45	447.79	114.10
20.617	459.90	56.82	537.66	67.13	398.51	49.99	440.68	54.58
29.937	444.06	37.21	522.39	44.07	393.11	33.36	433.73	36.44
40.167	436.92	26.94	514.60	31.97	390.81	24.36	432.26	26.63
49.244	419.50	21.04	491.03	24.84	377.40	19.14	420.25	21.14
60.373	411.63	17.97	483.74	21.32	372.94	16.41	411.64	18.00
70.243	416.93	16.14	492.04	19.17	378.96	14.78	418.87	16.23
80.156	430.36	15.32	515.30	18.46	390.36	14.02	435.50	15.55
88.516	449.62	14.46	555.03	17.93	405.34	13.18	449.78	14.48
98.323	445.54	13.80	545.67	17.01	398.62	12.42	445.32	13.80
111.223	486.10	14.31	638.97	19.67	443.04	13.21	490.96	14.45
119.747	463.21	13.21	598.35	18.24	429.87	12.41	477.21	13.60
131.622	464.85	13.77	613.65	17.85	423.96	15.38	449.15	15.32
139.843	279.34	7.47	302.00	8.12	281.25	7.66	290.85	7.87

Table 33: Evaporative heat transfer coefficient (W/m^{2}K) for thermocouple 3, $G = 1.0$ and $a_r = 10.0$-g.

Q_{in} (W)	Bottom		Outboard		Top		Inboard	
	h_e	Δh_e	h_e	Δh_e	h_e	Δh_e	h_e	Δh_e
10.966	481.33	121.70	371.79	93.86	497.07	126.34	384.47	96.94
20.617	492.73	61.22	421.63	52.04	475.25	58.87	373.01	45.89
29.937	456.38	38.25	409.86	34.24	463.64	38.94	362.65	30.28
40.167	437.11	26.96	404.06	24.89	458.29	28.37	357.19	22.00
49.244	397.39	19.92	376.38	18.88	417.50	20.99	338.47	16.93
60.373	371.00	16.16	353.02	15.37	394.82	17.25	323.81	14.09
70.243	373.33	14.42	357.94	13.86	402.65	15.62	328.37	12.69
80.156	373.56	13.26	359.88	12.76	408.53	14.55	329.80	11.72
88.516	357.08	11.44	345.29	11.06	398.93	12.80	321.13	10.28
98.323	348.10	10.75	338.22	10.45	391.09	12.07	314.48	9.70
111.223	431.25	12.84	430.27	12.65	487.93	14.32	371.88	10.91
119.747	455.53	13.01	453.58	13.21	513.89	14.77	384.19	10.90
131.622	497.45	16.08	498.82	16.37	577.61	16.40	415.00	11.44
139.843	488.28	13.53	497.25	13.39	535.33	14.49	391.14	10.58

Table 34: Evaporative heat transfer coefficient (W/m^{2}K) for thermocouple 4, $G = 1.0$ and $a_r = 10.0$-g.

Q_{in} (W)	Bottom		Outboard		Top		Inboard	
	h_e	Δh_e	h_e	Δh_e	h_e	Δh_e	h_e	Δh_e
10.966	588.69	150.59	662.27	170.79	609.26	155.58	702.64	182.87
20.617	757.80	96.01	590.32	73.63	548.86	68.21	605.06	75.99
29.937	648.24	55.43	540.05	45.75	508.73	42.79	554.32	46.82
40.167	568.73	35.78	506.72	31.44	483.23	29.81	525.65	32.62
49.244	484.92	24.40	457.21	23.03	444.39	22.28	481.88	24.31
60.373	456.40	19.98	439.36	19.24	425.15	18.54	462.11	20.24
70.243	476.94	18.50	454.31	17.61	438.36	16.98	475.34	18.46
80.156	482.98	17.27	458.12	16.32	440.30	15.68	476.46	16.98
88.516	433.32	13.94	425.63	13.70	409.84	13.18	427.58	13.78
98.323	419.12	13.02	415.38	12.85	402.23	12.40	419.23	12.95
111.223	464.66	14.42	458.63	14.08	449.18	13.65	477.19	14.46
119.747	479.96	13.58	475.84	13.45	455.26	13.04	483.56	13.99
131.622	508.81	14.43	507.35	13.82	486.08	13.09	510.85	13.92
139.843	497.84	13.35	507.00	13.58	479.60	12.85	494.35	13.30

Table 35: Evaporative heat transfer coefficient (W/m^{2}K) for thermocouple 5, $G = 1.0$ and $a_r = 10.0$-g.

Q_{in}	Bottom		Outboard		Top		Inboard	
	h_e	Δh_e	h_e	Δh_e	h_e	Δh_e	h_e	Δh_e
10.966	717.21	185.83	903.80	240.71	758.06	195.90	960.79	255.12
20.617	1114.11	145.03	648.33	81.44	721.99	90.66	909.16	116.66
29.937	1148.33	102.74	652.49	55.40	708.48	60.22	869.98	76.01
40.167	1159.28	76.00	652.43	40.91	698.94	44.10	843.92	54.13
49.244	1162.59	62.35	649.35	33.29	683.72	34.92	836.54	43.42
60.373	1158.07	53.23	648.36	28.83	674.15	29.70	811.23	36.11
70.243	1152.33	46.91	654.46	25.62	676.02	26.52	806.42	31.92
80.156	1129.35	42.24	653.01	23.58	673.65	24.27	798.64	29.13
88.516	1155.44	38.64	649.23	21.10	665.69	21.72	787.13	26.02
98.323	1127.79	36.04	639.64	20.05	658.06	20.53	771.64	24.24
111.223	1132.65	34.66	649.71	19.18	669.96	19.76	780.17	23.13
119.747	1119.88	32.42	646.48	18.20	667.68	18.82	775.49	22.09
131.622	1132.93	31.58	651.00	17.62	676.16	18.29	781.98	21.37
139.843	1087.71	30.19	627.91	16.95	647.74	17.46	746.76	20.26

Table 36: Evaporative heat transfer coefficient (W/m^{2}K) for thermocouple 2, $G = 1.5$ and $a_r = 10.0$-g.

Q_{in} (W)	Bottom		Outboard		Top		Inboard	
	h_e	Δh_e	h_e	Δh_e	h_e	Δh_e	h_e	Δh_e
10.281	449.88	107.45	507.44	122.39	395.13	95.90	418.71	100.39
20.038	421.66	51.60	477.88	58.98	380.43	47.16	409.89	50.35
30.875	397.20	30.58	450.77	35.02	365.54	28.53	395.26	30.59
41.022	404.27	55.40	463.62	63.79	366.42	68.49	395.65	73.51
50.181	374.47	43.03	427.01	49.21	360.19	55.72	390.11	60.10
61.273	395.65	29.25	450.31	33.50	361.90	36.12	394.93	38.97
70.586	391.52	25.71	448.51	29.59	371.39	32.97	407.34	35.80
80.548	394.49	13.79	454.15	15.94	368.87	13.02	405.18	14.21
89.981	394.57	12.92	455.07	15.07	369.10	12.14	406.52	13.33
100.278	403.17	12.16	465.86	14.16	379.79	11.58	417.89	12.64
111.715	435.63	19.55	512.23	22.39	417.47	18.18	455.13	19.71
122.090	462.96	19.67	555.08	23.01	454.68	18.63	482.78	19.77
129.122	472.64	12.61	571.10	15.31	464.73	12.52	493.11	13.18
140.716	487.24	12.74	586.92	15.50	480.83	13.49	510.32	13.48
149.761	500.55	12.64	602.03	15.28	481.68	12.29	516.89	13.13
158.110	507.76	12.89	634.91	16.24	500.24	12.84	525.07	13.36
169.488	523.84	13.06	651.86	16.29	511.78	12.88	538.84	13.42
180.974	535.21	12.98	660.12	16.09	511.08	12.60	543.32	13.30

Table 37: Evaporative heat transfer coefficient (W/m²K) for thermocouple 3, $G = 1.5$ and $a_r = 10.0$-g.

Q_{in} (W)	Bottom		Outboard		Top		Inboard	
	h_e	Δh_e	h_e	Δh_e	h_e	Δh_e	h_e	Δh_e
10.281	577.30	139.40	446.53	107.27	507.09	121.81	393.17	94.08
20.038	491.65	60.41	414.94	50.89	475.89	58.58	376.39	45.97
30.875	422.00	32.77	369.09	28.60	428.94	33.24	341.93	26.41
41.022	445.48	61.17	392.22	53.73	434.92	85.17	350.74	66.30
50.181	395.84	45.55	354.53	40.71	418.53	67.31	337.12	52.21
61.273	390.18	28.85	354.22	26.14	396.00	40.26	322.65	32.04
70.586	378.91	24.86	346.81	22.72	403.03	36.97	326.00	29.08
80.548	377.81	13.20	350.07	12.23	397.83	13.92	320.21	11.18
89.981	365.13	12.02	341.24	11.20	388.39	12.68	311.81	10.17
100.278	426.12	12.94	406.60	12.60	456.22	14.02	354.11	10.73
111.715	467.72	23.57	454.32	24.90	520.15	22.58	387.43	16.78
122.090	478.20	23.04	454.51	23.67	541.05	22.20	393.12	16.04
129.122	506.96	14.00	482.42	13.34	592.51	16.56	413.34	11.22
140.716	536.94	14.28	521.23	13.99	619.94	16.79	434.71	11.58
149.761	555.63	14.38	543.26	13.77	656.71	16.82	446.01	11.26
158.110	588.75	15.59	555.49	14.28	679.36	18.12	461.34	11.94
169.488	603.73	15.11	590.11	15.17	726.39	18.85	472.10	11.76
180.974	620.00	15.07	619.34	14.99	750.54	19.06	479.35	11.80

Table 38: Evaporative heat transfer coefficient (W/m^{2}K) for thermocouple 4, $G = 1.5$ and $a_r = 10.0$-g.

Q_{in} (W)	Bottom		Outboard		Top		Inboard	
	h_e	Δh_e	h_e	Δh_e	h_e	Δh_e	h_e	Δh_e
10.281	928.13	231.36	639.44	156.02	621.05	150.31	797.22	198.45
20.038	918.59	117.63	629.37	78.24	596.45	73.93	717.65	90.04
30.875	748.58	59.57	550.11	43.12	513.69	39.96	567.21	44.60
41.022	759.48	106.82	561.64	77.73	502.19	105.85	541.74	122.58
50.181	606.42	70.64	490.18	56.65	470.67	79.77	493.48	87.62
61.273	530.68	39.82	467.79	34.69	424.03	44.97	433.25	47.34
70.586	488.55	32.45	450.13	29.67	426.14	40.53	432.28	42.11
80.548	473.62	16.69	446.99	15.66	414.66	14.51	417.94	14.64
89.981	398.02	13.04	413.00	13.54	382.50	12.49	377.78	12.37
100.278	468.11	16.16	469.20	14.47	449.23	13.71	444.02	13.59
111.715	484.68	25.36	486.70	24.74	470.53	20.39	465.14	20.18
122.090	484.87	25.49	496.99	24.24	466.13	19.03	454.26	18.54
129.122	509.75	13.93	513.32	13.68	487.61	13.00	478.41	12.94
140.716	532.16	14.53	538.50	14.31	512.85	13.50	499.67	13.47
149.761	560.22	14.26	552.83	13.96	527.99	13.43	517.27	13.14
158.110	563.44	17.91	550.33	14.32	531.06	13.72	527.40	13.60
169.488	576.83	15.59	571.12	14.29	552.32	13.77	535.02	13.37
180.974	610.85	14.90	591.22	14.30	572.84	13.88	560.35	13.56

Table 39: Evaporative heat transfer coefficient (W/m²K) for thermocouple 5, $G = 1.5$ and $a_r = 10.0$-g.

Q_{in}	Bottom		Outboard		Top		Inboard	
	h_e	Δh_e	h_e	Δh_e	h_e	Δh_e	h_e	Δh_e
10.281	1471.54	390.35	675.21	164.90	859.31	211.69	1020.30	257.08
20.038	1391.51	187.16	677.45	85.01	847.80	107.02	949.04	121.45
30.875	1301.98	110.09	646.08	51.20	804.54	64.16	880.23	71.07
41.022	1433.55	217.38	681.79	95.15	810.19	184.75	881.20	212.59
50.181	1262.11	156.87	629.86	73.51	794.65	149.84	852.69	169.34
61.273	1268.49	103.04	635.53	47.79	736.49	92.79	775.69	100.82
70.586	1185.01	84.26	608.84	40.59	735.94	82.94	768.87	89.55
80.548	1174.06	43.46	610.03	21.58	709.13	25.13	736.56	26.24
89.981	1144.59	39.25	602.06	19.91	686.98	22.69	705.12	23.45
100.278	1139.51	35.89	612.11	18.67	709.81	21.65	728.73	22.39
111.715	1166.11	70.17	625.51	35.62	736.42	32.11	752.17	32.76
122.090	1173.63	66.98	626.69	33.69	731.70	30.01	745.27	30.65
129.122	1160.12	32.07	622.32	16.74	736.16	19.81	747.97	20.21
140.716	1181.13	31.67	636.29	16.63	754.53	19.82	763.99	20.18
149.761	1174.68	30.51	634.69	16.07	756.12	19.19	766.27	19.52
158.110	1142.55	29.90	619.87	15.86	744.46	19.10	750.00	19.27
169.488	1127.02	28.70	615.08	15.35	739.08	18.51	747.10	18.78
180.974	1106.86	27.28	619.64	15.01	752.48	18.89	755.01	19.36

Table 40: Thermal resistance, Transported heat and Input heat for $G = 0.5$ and $a_r = 0.01$-g.

R_{th} (K/W)	ΔR_{th} (K/W)	Q_t (W)	ΔQ_t (W)	Q_{in} (W)	ΔQ_{in} (W)
2.4929	1.30160	5.829	3.042	11.254	2.220
3.3485	1.29290	7.791	3.007	15.494	2.615
4.8585	1.80183	8.360	3.100	20.777	3.039
4.5051	1.25605	11.528	3.214	25.045	3.331

Table 41: Thermal resistance, Transported heat and Input heat for $G = 1.0$ and $a_r = 0.01$-g.

R_{th} (K/W)	ΔR_{th} (K/W)	Q_t (W)	ΔQ_t (W)	Q_{in} (W)	ΔQ_{in} (W)
0.4635	0.21369	7.091	3.208	10.903	2.180
0.3256	0.06563	16.948	3.321	21.176	3.053
0.5154	0.06955	25.104	3.338	30.494	3.666
0.8716	0.09011	32.608	3.358	40.053	4.192
1.2130	0.10852	38.928	3.475	49.903	4.707

Table 42: Thermal resistance, Transported heat and Input heat for $G = 1.5$ and $a_r = 0.01$-g.

R_{th} (K/W)	ΔR_{th} (K/W)	Q_t (W)	ΔQ_t (W)	Q_{in} (W)	ΔQ_{in} (W)
0.4663	0.16527	8.666	3.019	10.124	2.096
0.2707	0.05004	17.406	3.067	20.024	2.955
0.1908	0.02399	27.874	3.254	29.462	3.592
0.1835	0.01844	36.886	3.352	39.808	4.177
0.1768	0.01534	44.497	3.365	50.142	4.697
0.1652	0.01357	54.705	3.213	60.577	5.165
0.1858	0.01073	63.351	3.256	69.754	5.544
0.2151	0.01312	72.570	3.114	80.619	5.994
0.2707	0.01271	82.626	3.720	89.645	6.273
0.3419	0.01330	92.707	3.487	101.692	6.691
0.4430	0.01617	98.670	3.544	110.802	7.007

Table 43: Thermal resistance, Transported heat and Input heat for $G = 0.5$ and a_r = 10.0-g.

R_{th} (K/W)	ΔR_{th} (K/W)	Q_t (W)	ΔQ_t (W)	Q_{in} (W)	ΔQ_{in} (W)
0.2555	0.06309	7.131	1.677	10.735	2.174
0.4580	0.06988	10.823	1.621	15.694	2.625
0.8389	0.10052	13.599	1.621	20.869	3.041
1.2670	0.13577	15.065	1.611	25.298	3.361
1.5288	0.16352	17.230	1.841	29.973	3.661
1.6983	0.15601	19.268	1.768	33.634	3.899
1.9696	0.15523	21.642	1.704	40.170	4.220
2.0622	0.15873	22.892	1.761	43.285	4.404

Table 44: Thermal resistance, Transported heat and Input heat for $G = 1.0$ and a_r = 10.0-g.

R_{th} (K/W)	ΔR_{th} (K/W)	Q_t (W)	ΔQ_t (W)	Q_{in} (W)	ΔQ_{in} (W)
0.3529	0.09036	6.921	1.721	10.966	2.196
0.2324	0.03002	14.516	1.762	20.617	3.007
0.1963	0.01719	22.005	1.800	29.937	3.640
0.1737	0.01143	29.894	1.789	40.167	4.210
0.1578	0.00851	37.977	1.842	49.244	4.673
0.1405	0.00662	47.087	1.973	60.373	5.173
0.1183	0.00516	55.452	2.047	70.243	5.595
0.0853	0.00360	62.975	2.119	80.156	5.972
0.0817	0.00322	70.110	2.108	88.516	6.298
0.0765	0.00299	77.254	2.227	98.323	6.636
0.0590	0.00271	89.159	2.405	111.223	7.053
0.0577	0.00242	95.625	2.449	119.747	7.323
0.0942	0.00606	106.054	2.594	131.622	7.673
0.2620	0.00670	110.573	2.701	139.843	7.929

Table 45: Thermal resistance, Transported heat and Input heat for $G = 1.5$ and a_r = 10.0-g.

R_{th} (K/W)	ΔR_{th} (K/W)	Q_t (W)	ΔQ_t (W)	Q_{in} (W)	ΔQ_{in} (W)
0.5400	0.12865	7.502	1.770	10.281	2.107
0.3435	0.04257	14.906	1.797	20.038	2.951
0.2629	0.02075	23.055	1.742	30.875	3.668
0.2292	0.03527	31.702	4.285	41.022	4.256
0.2130	0.02785	37.905	4.301	50.181	4.705
0.1696	0.01528	47.508	3.429	61.273	5.203
0.1493	0.01258	54.078	3.460	70.586	5.601
0.1282	0.00479	61.757	2.043	80.548	5.972
0.1304	0.00454	69.557	2.133	89.981	6.312
0.1178	0.00386	77.290	2.168	100.278	6.680
0.1028	0.00485	88.473	3.701	111.715	7.039
0.0992	0.00446	95.964	3.769	122.090	7.365
0.0941	0.00289	101.478	2.464	129.122	7.575
0.0854	0.00262	112.422	2.654	140.716	7.910
0.0809	0.00251	119.096	2.705	149.761	8.164
0.0771	0.00248	124.457	2.857	158.110	8.445
0.0729	0.00217	131.473	2.941	169.488	8.708
0.0652	0.00203	140.110	3.026	180.974	9.002

9.4   Steady–State Temperature Distributions
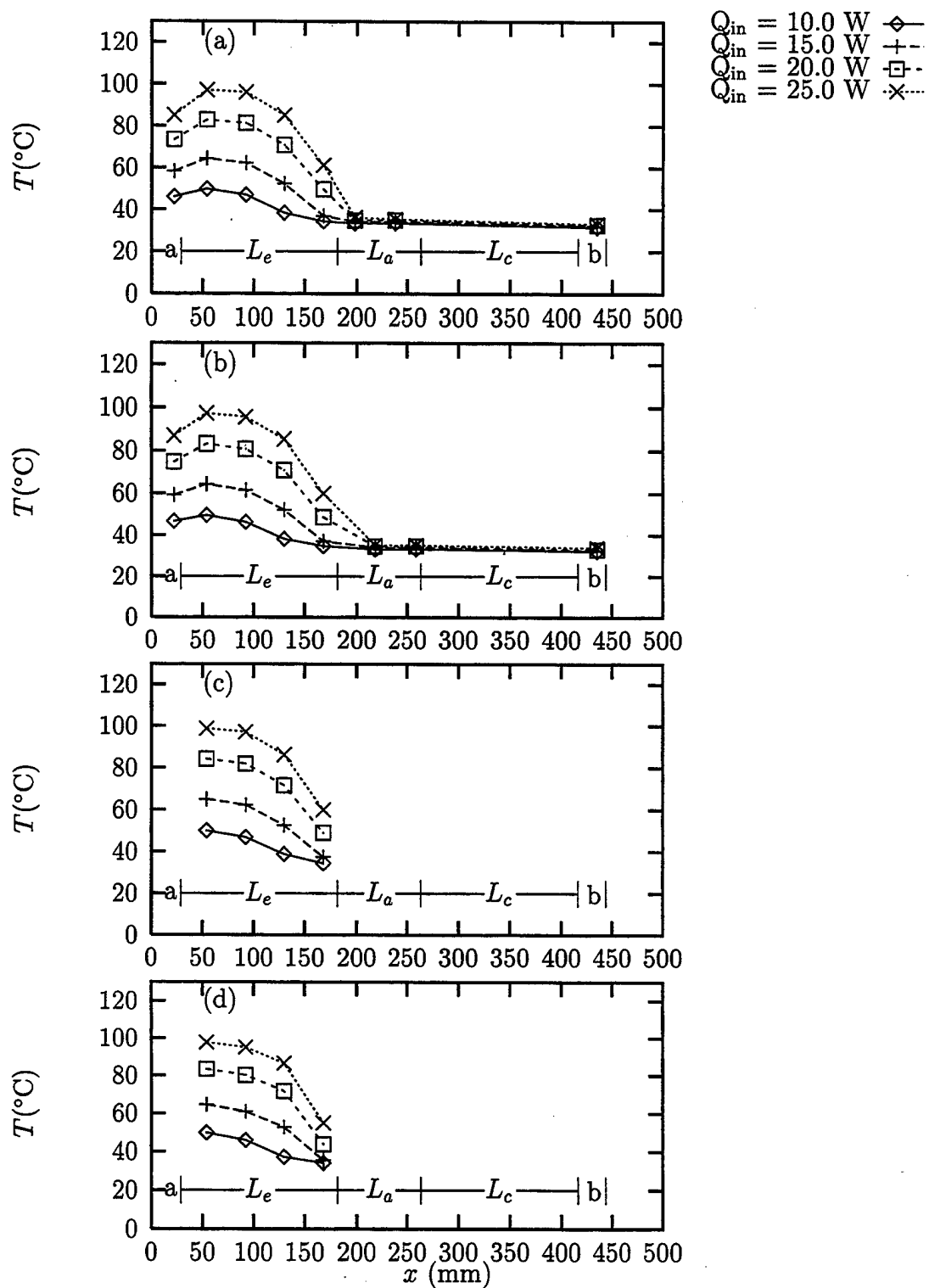
Figure 20: Steady state temperature distributions for $|\vec{a}_r| = 0.01$ g, $G = 0.5$: (a) Inboard; (b) Outboard; (c) Top; (d) Bottom.
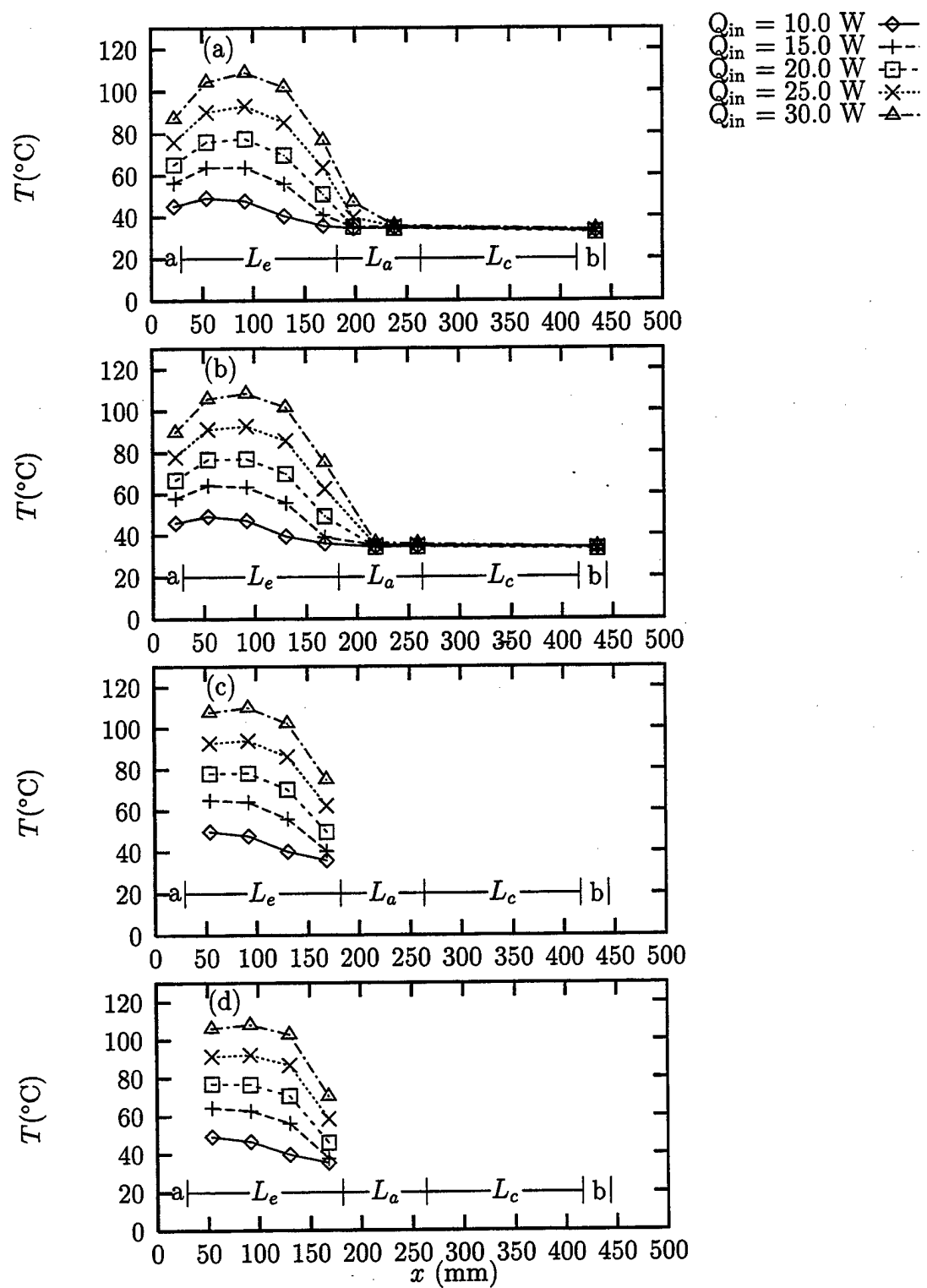
Figure 21: Steady state temperature distributions for $|\vec{a}_r| = 2.0$ g, $G = 0.5$: (a) Inboard; (b) Outboard; (c) Top; (d) Bottom.
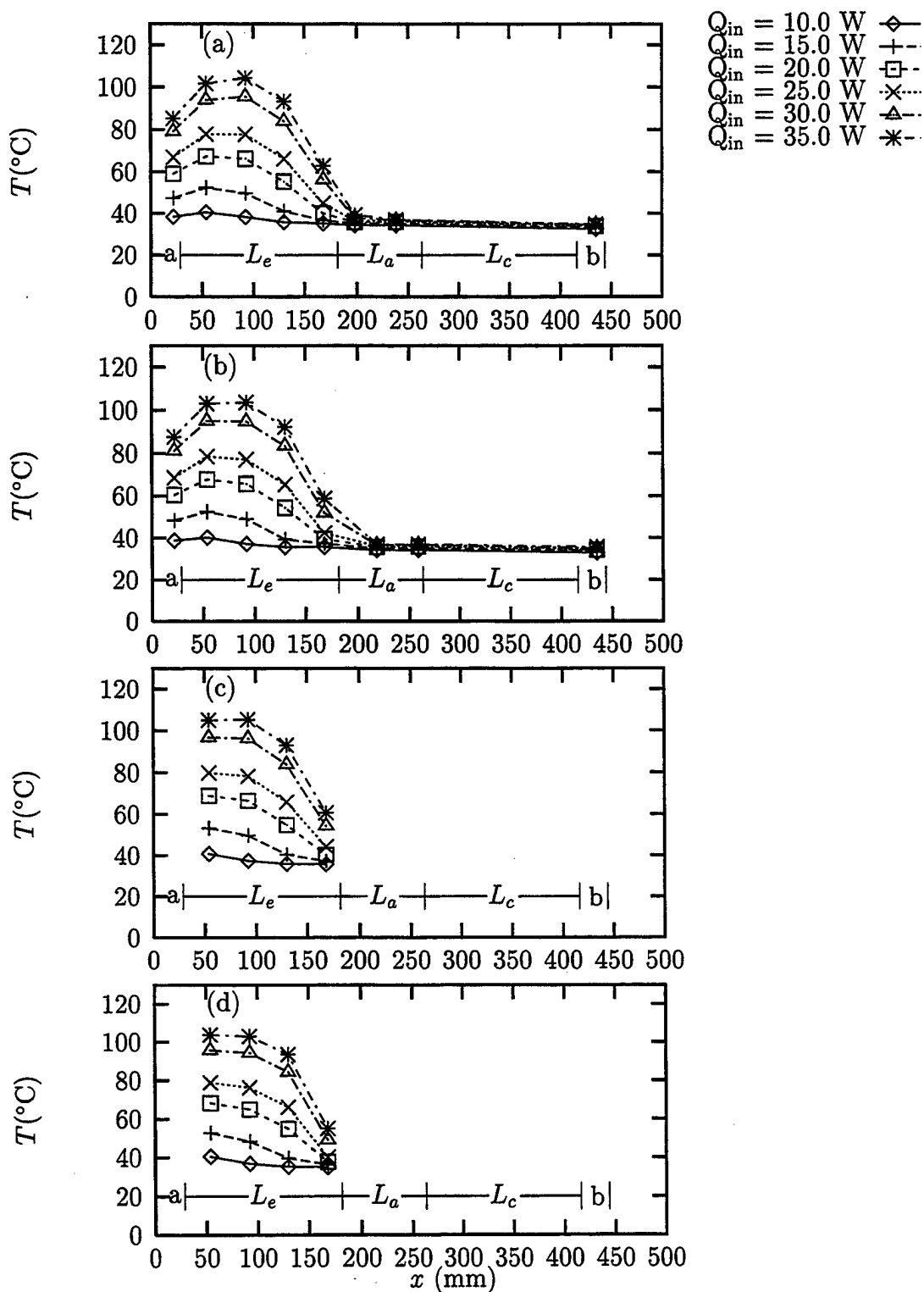
Figure 22: Steady state temperature distributions for $|\vec{a}_r| = 4.0$ g, $G = 0.5$: (a) Inboard; (b) Outboard; (c) Top; (d) Bottom.
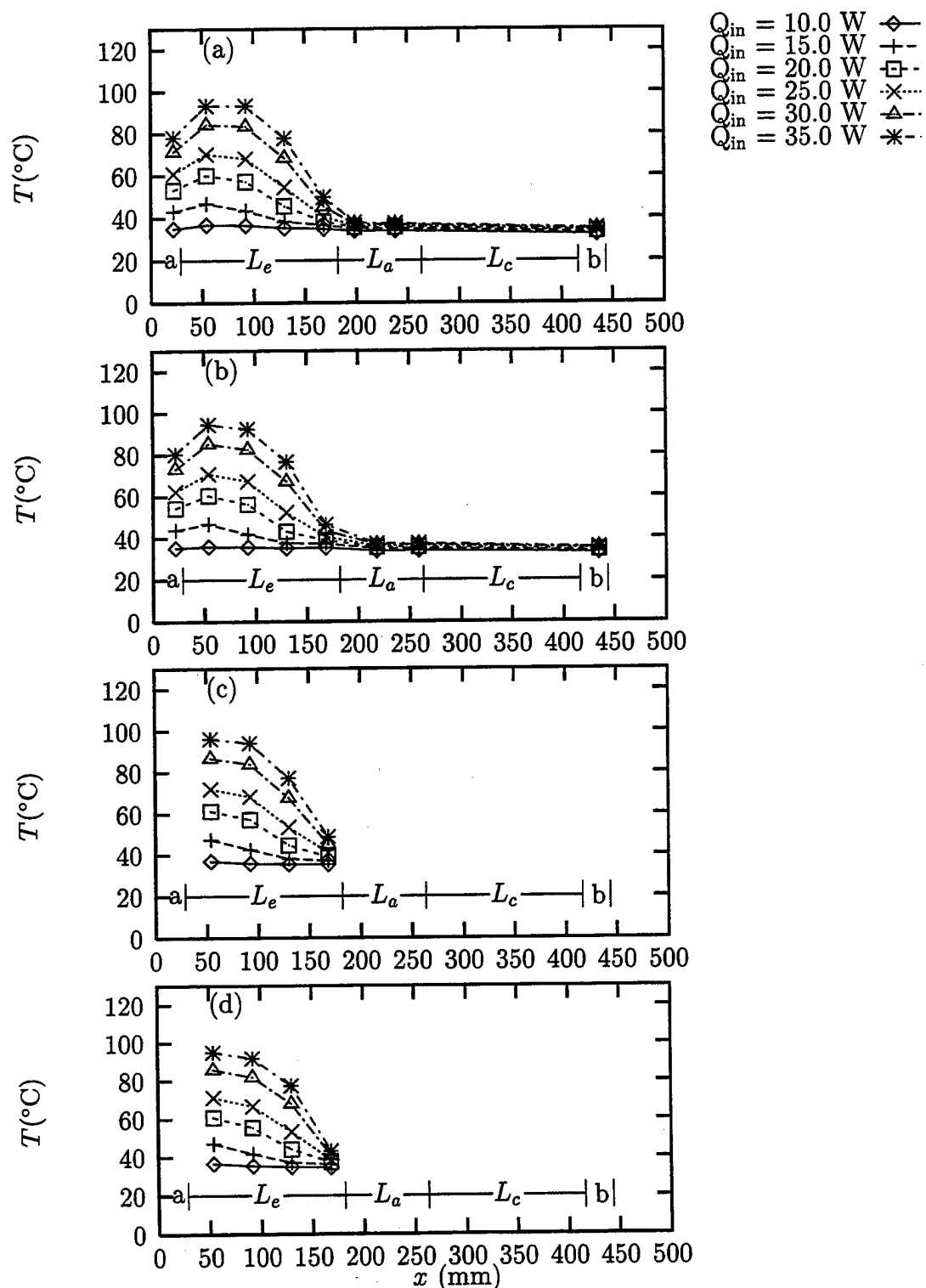
Figure 23: Steady state temperature distributions for $|\vec{a}_r| = 6.0$ g, $G = 0.5$: (a) Inboard; (b) Outboard; (c) Top; (d) Bottom.
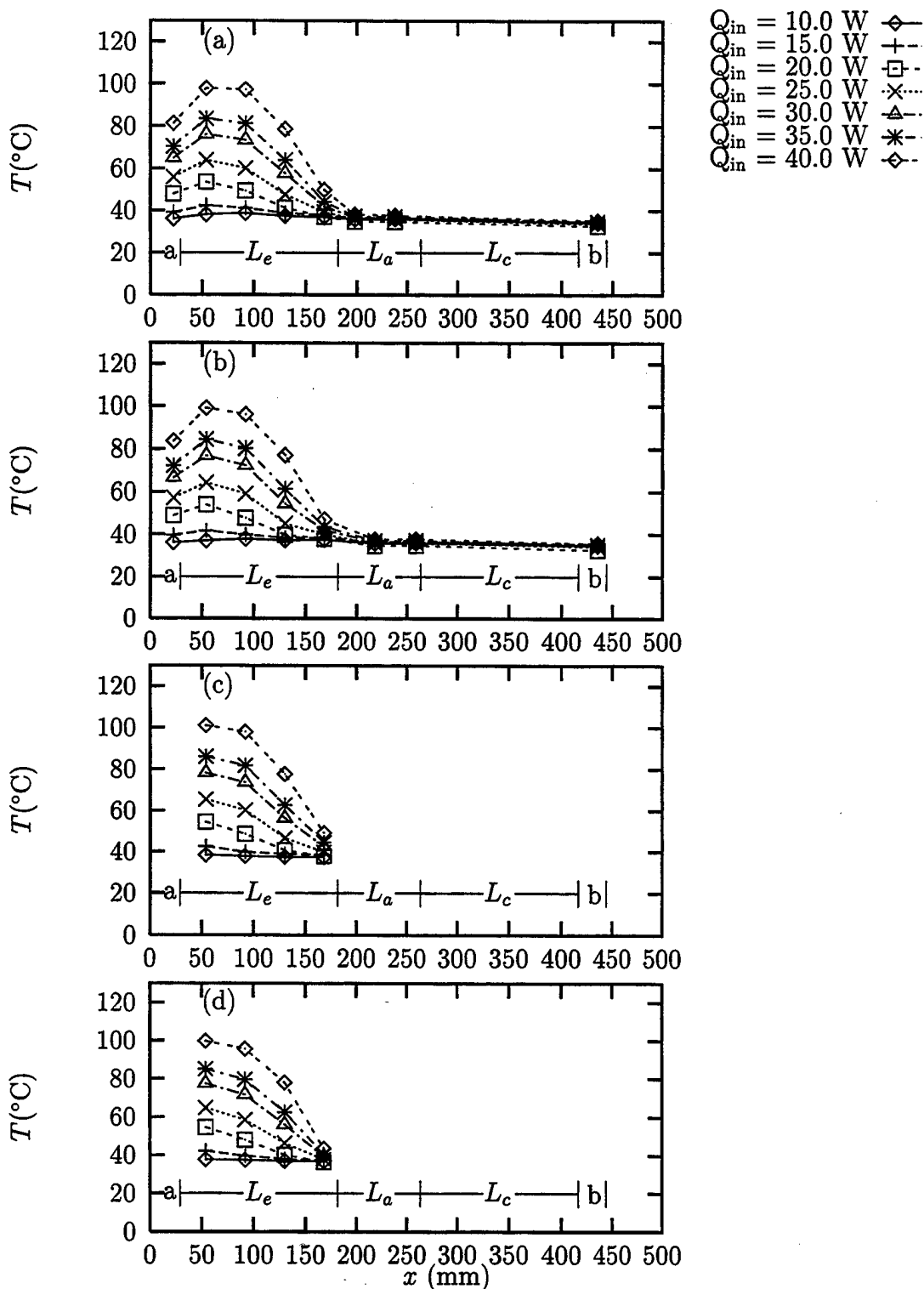
Figure 24: Steady state temperature distributions for $|\vec{a}_r| = 8.0$ g, $G = 0.5$: (a)Inboard; (b) Outboard; (c) Top; (d) Bottom.
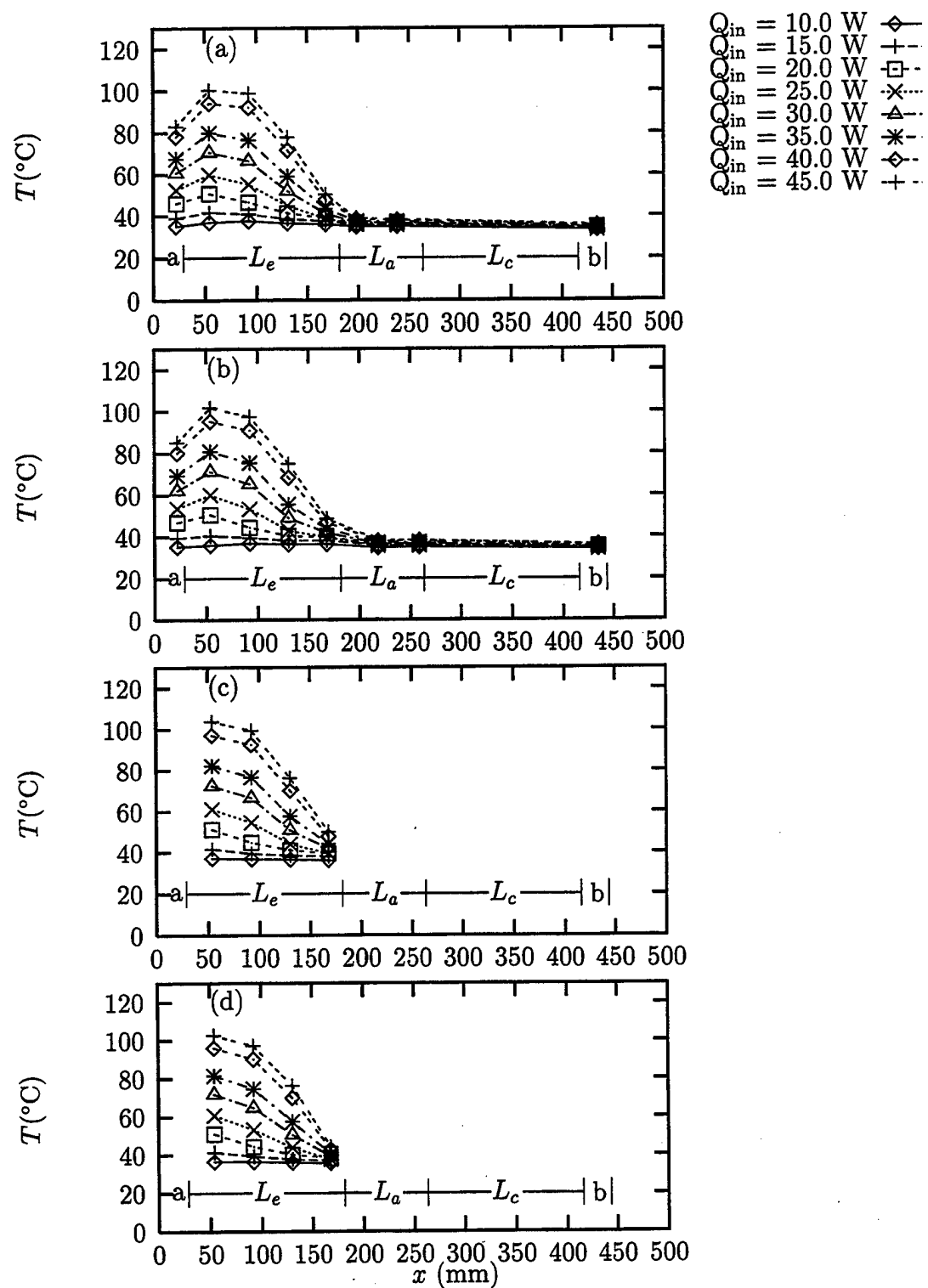
Figure 25: Steady state temperature distributions for $|\vec{a}_r| = 10.0$ g, $G = 0.5$: (a) Inboard; (b) Outboard; (c) Top; (d) Bottom.
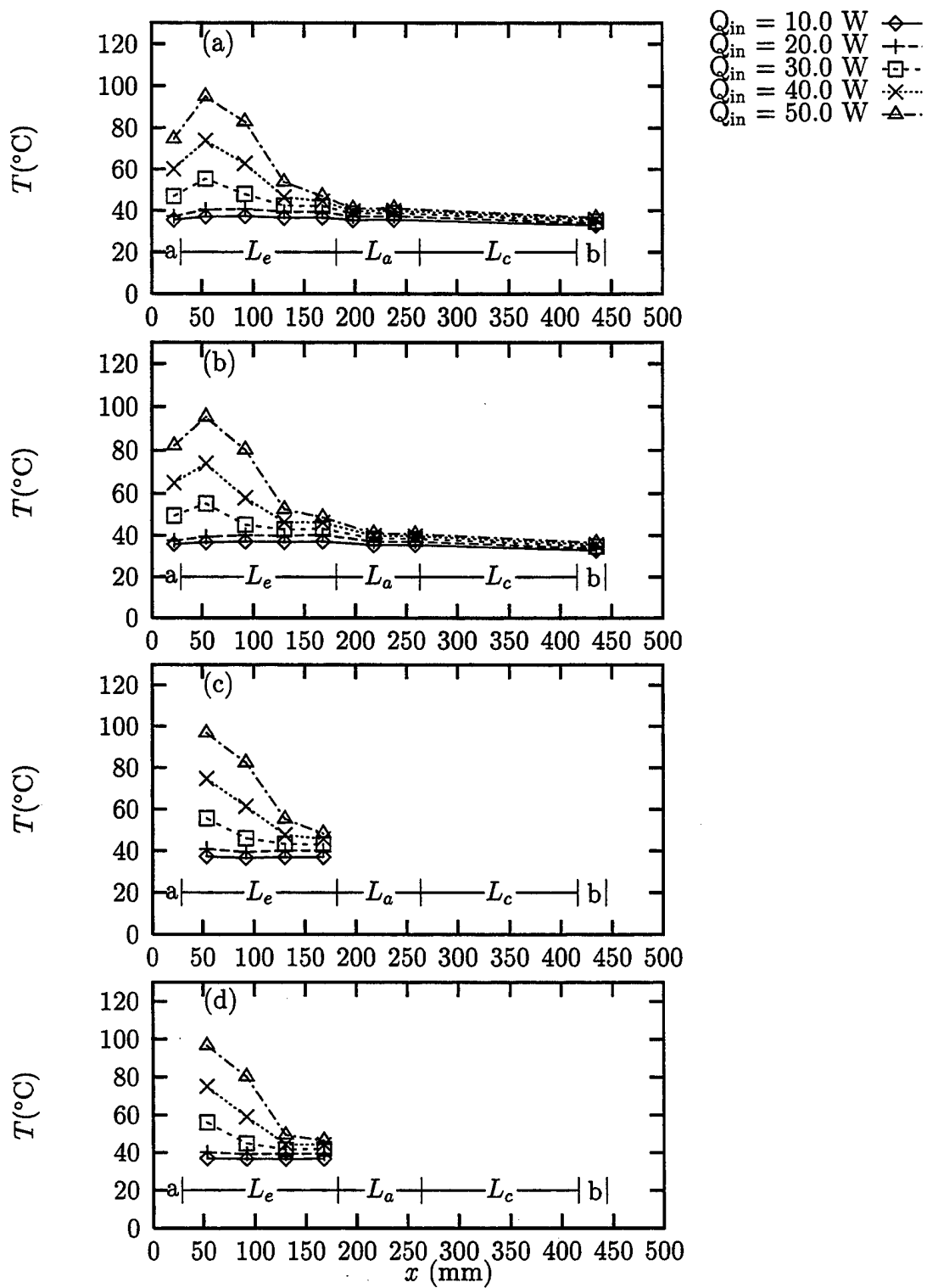
Figure 26: Steady state temperature distributions for $|\vec{a}_r| = 2.0$ g, $G = 1.0$: (a) Inboard; (b) Outboard; (c) Top; (d) Bottom.
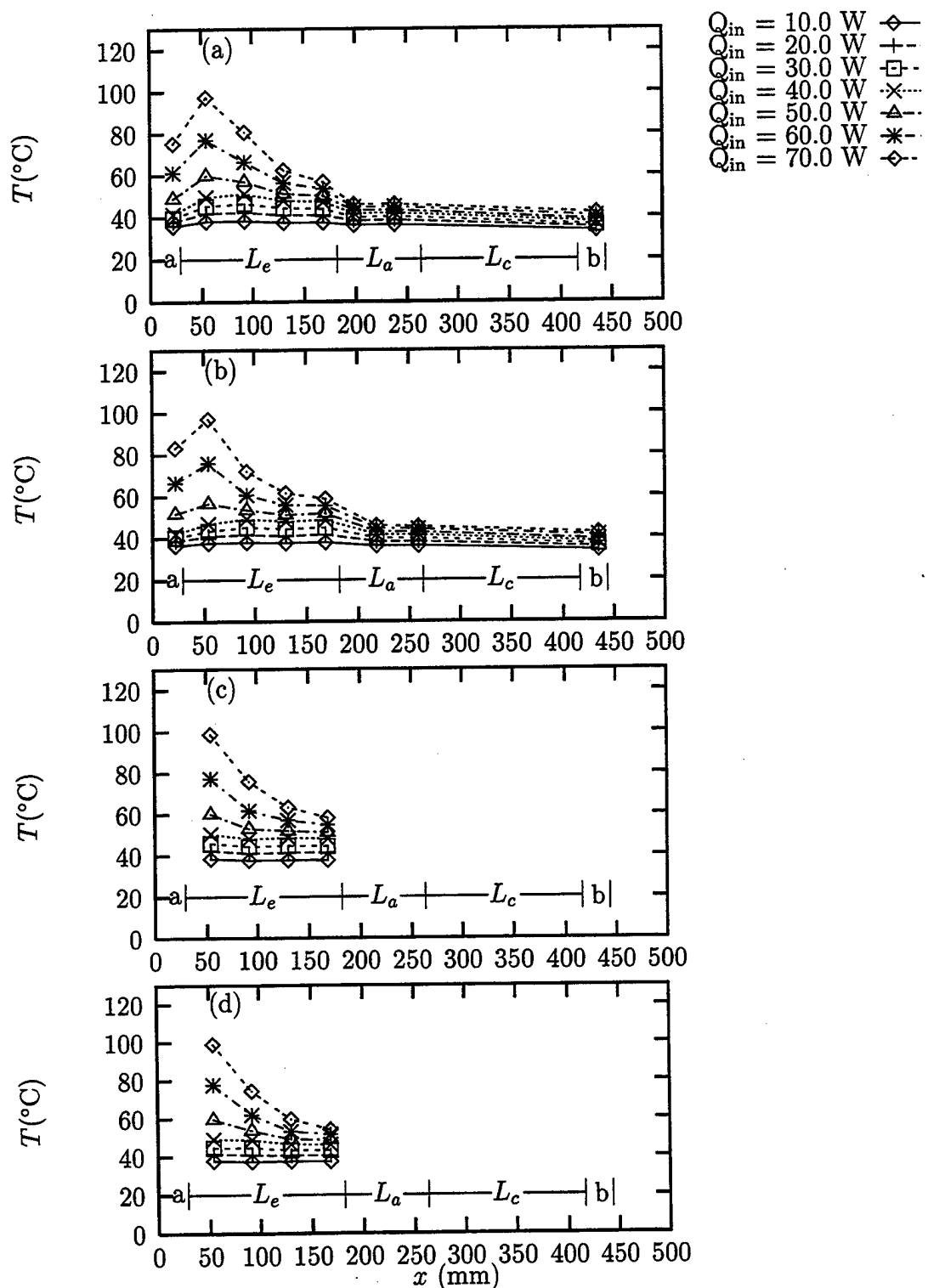
Figure 27: Steady state temperature distributions for $|\vec{a}_r| = 4.0$ g, $G = 1.0$: (a) Inboard; (b) Outboard; (c) Top; (d) Bottom.

83
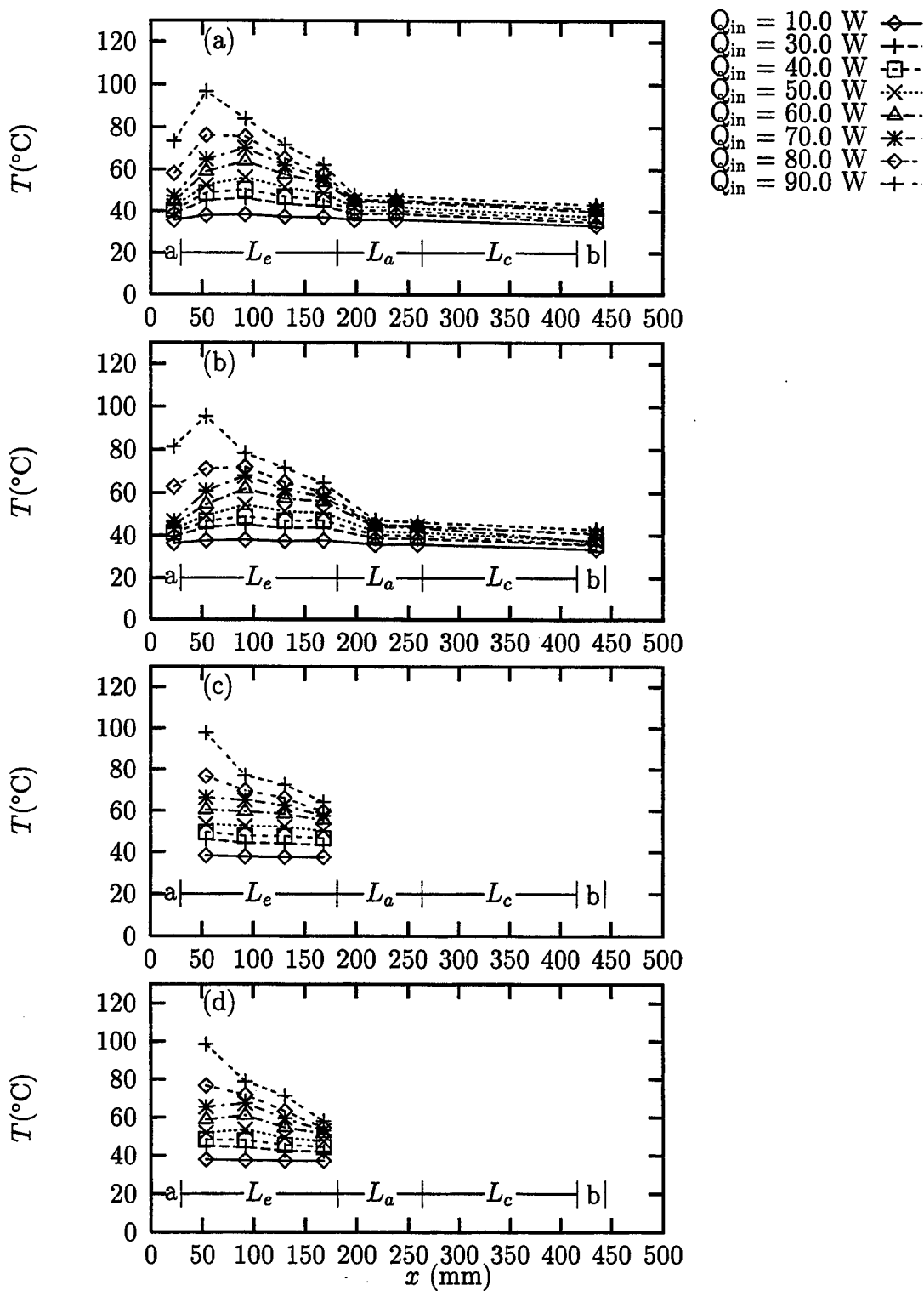
Figure 28: Steady state temperature distributions for $|\vec{a}_r| = 6.0$ g, $G = 1.0$: (a) Inboard; (b) Outboard; (c) Top; (d) Bottom.
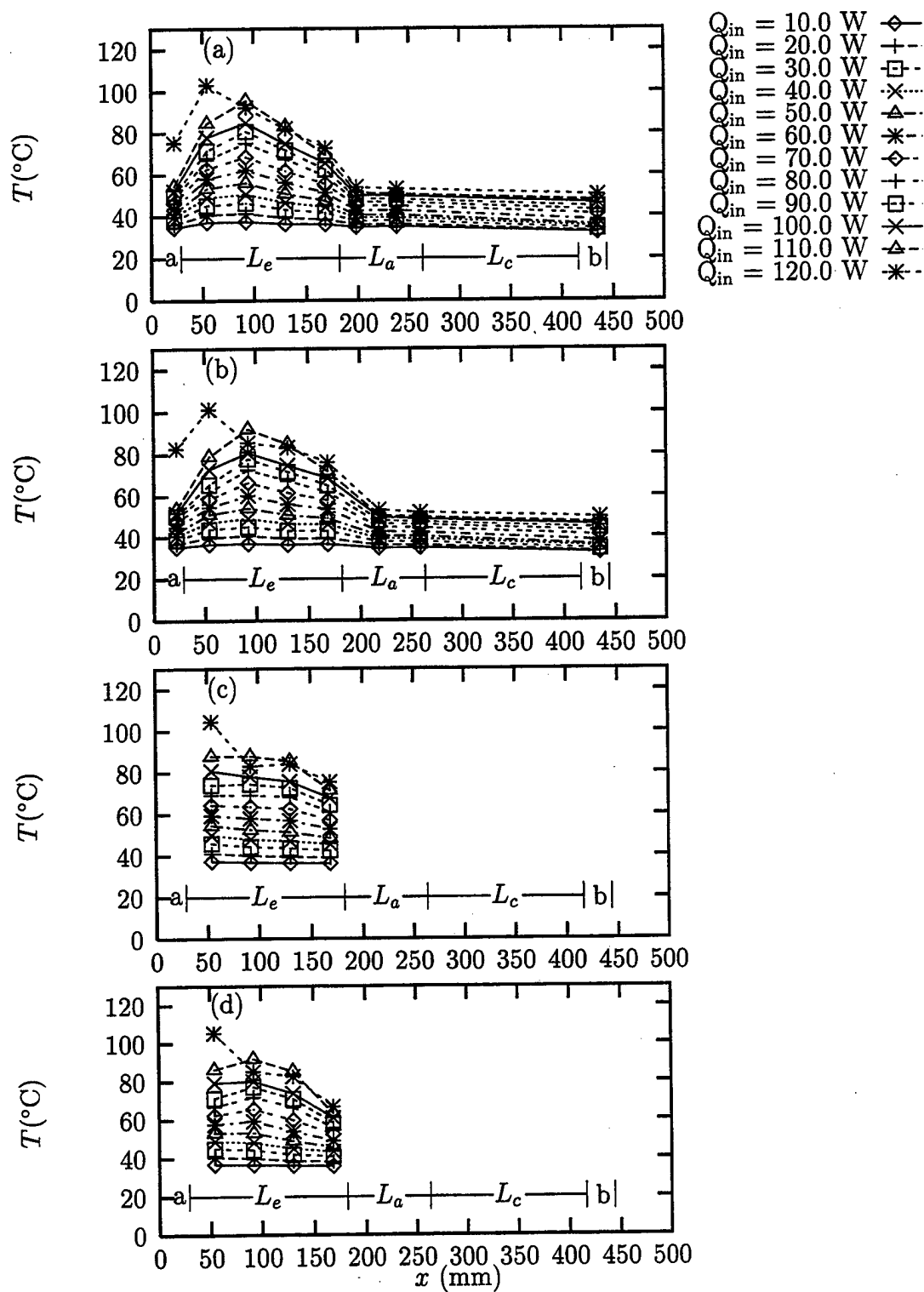
Figure 29: Steady state temperature distributions for $|\vec{a}_r| = 8.0$ g, $G = 1.0$: (a) Inboard; (b) Outboard; (c) Top; (d) Bottom.
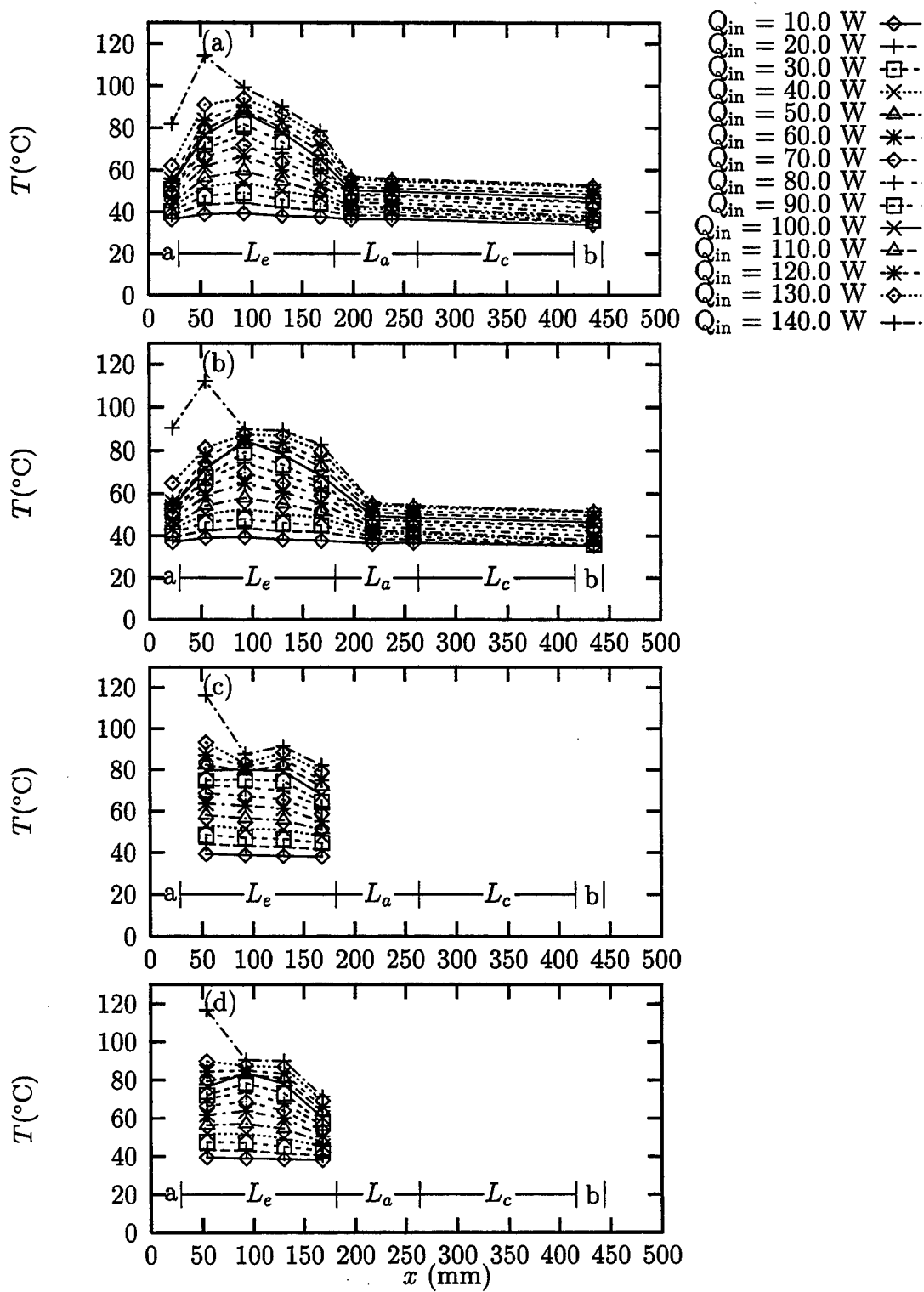
Figure 30: Steady state temperature distributions for $|\vec{a}_r| = 10.0$ g, $G = 1.0$: (a) Inboard; (b) Outboard; (c) Top; (d) Bottom.
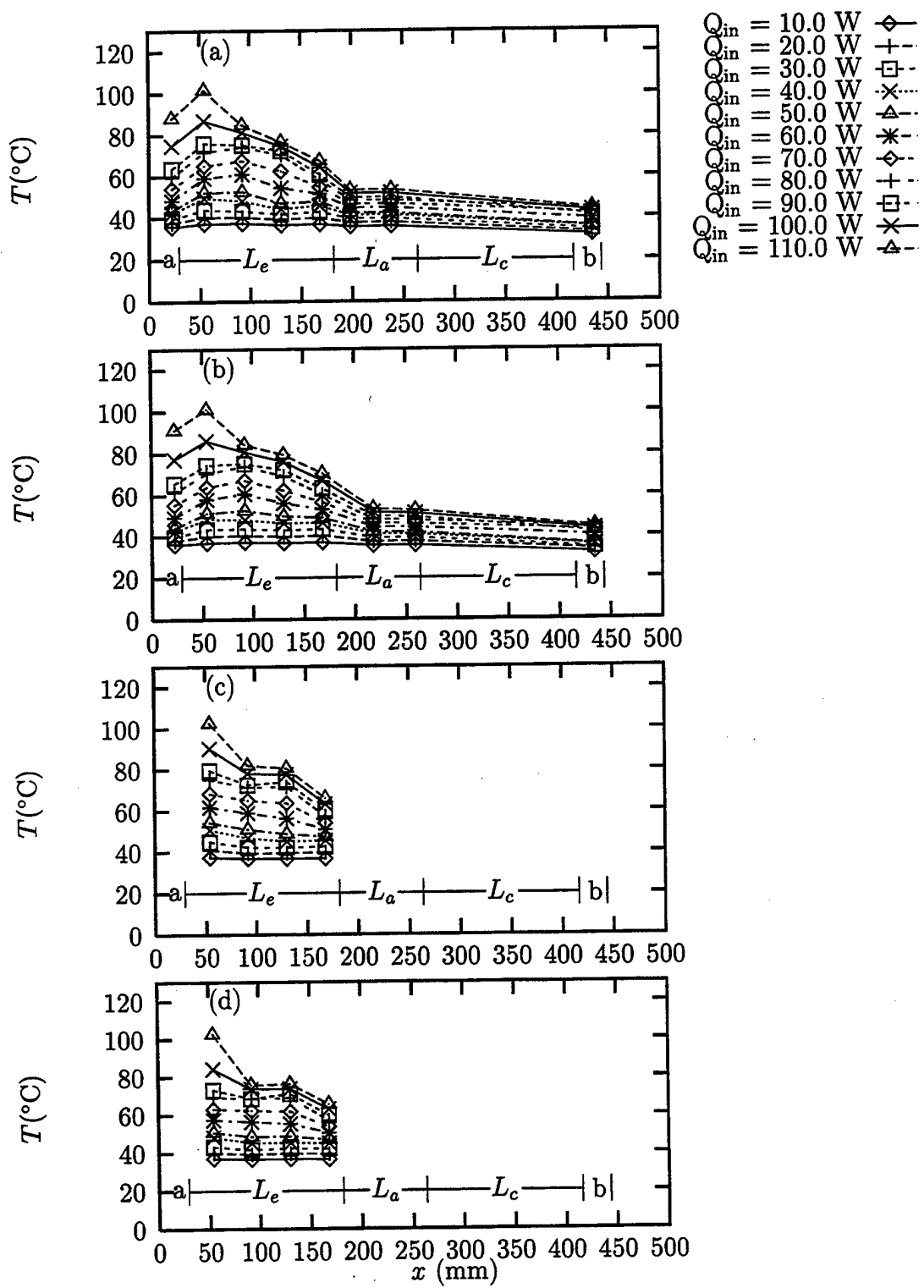
Figure 31: Steady state temperature distributions for $|\vec{a}_r| = 0.01$ g, $G = 1.5$: (a) Inboard; (b) Outboard; (c) Top; (d) Bottom.
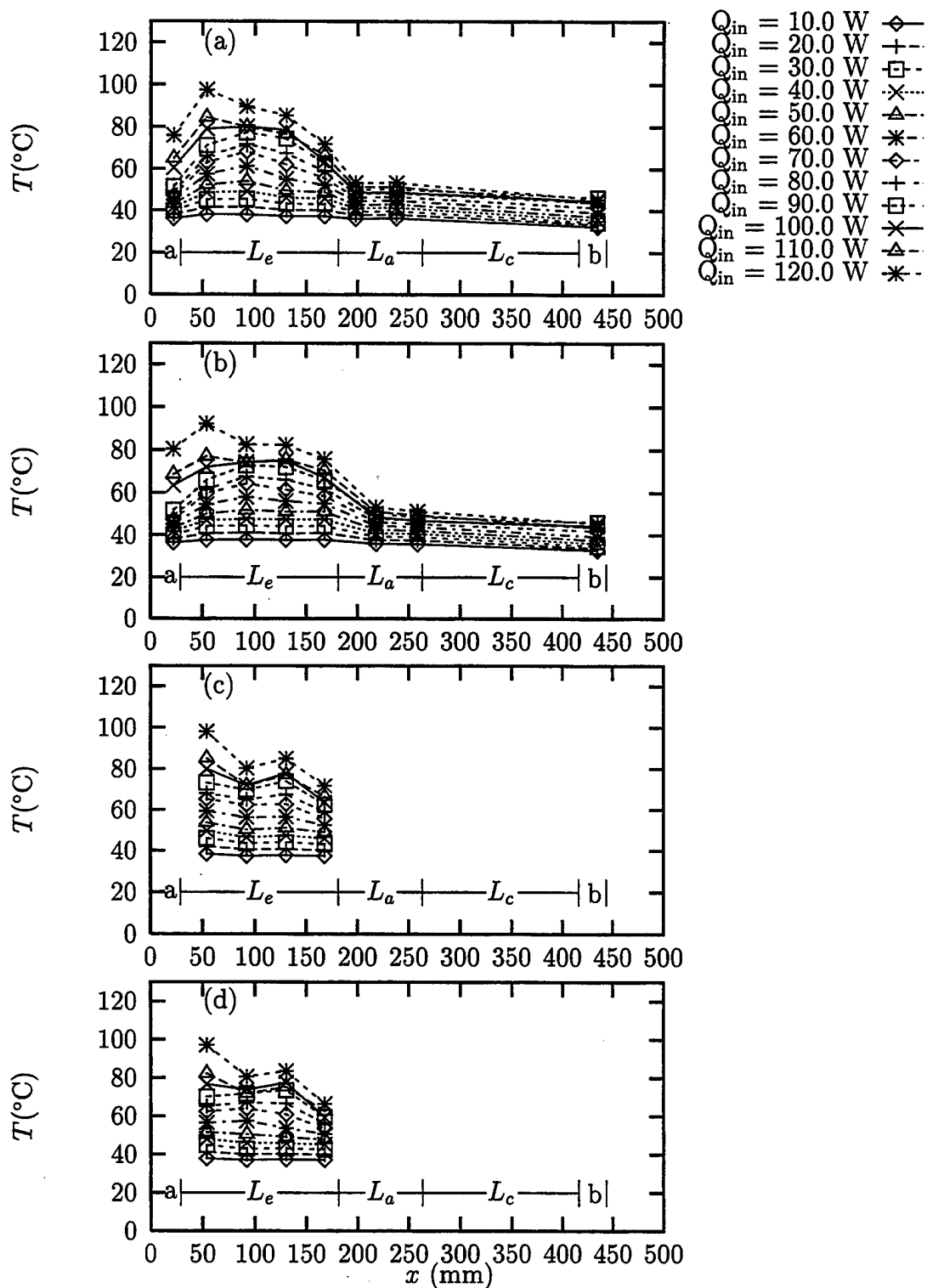
Figure 32: Steady state temperature distributions for $|\vec{a}_r| = 2.0$ g, $G = 1.5$: (a) Inboard; (b) Outboard; (c) Top; (d) Bottom.
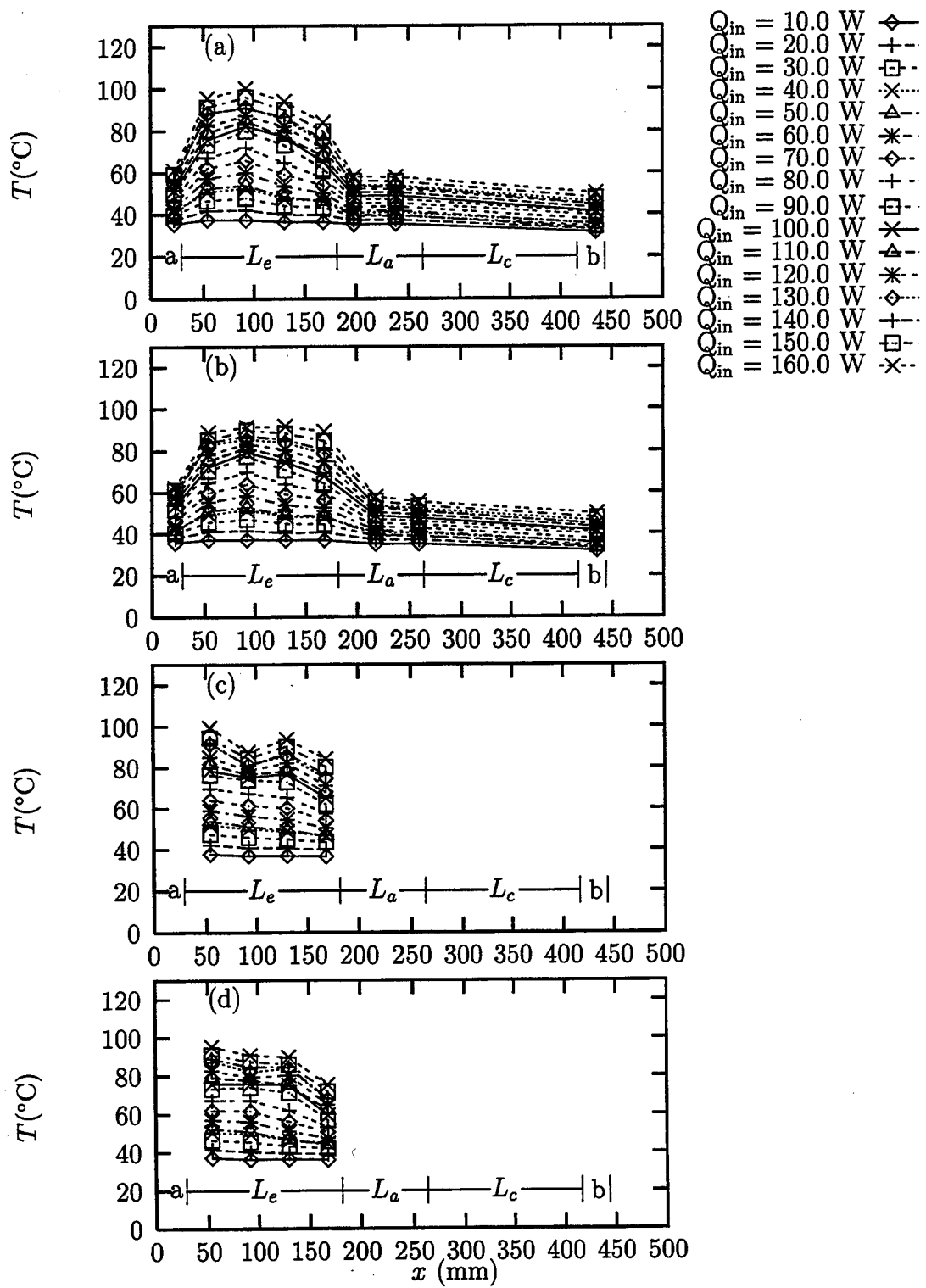
Figure 33: Steady state temperature distributions for $|\vec{a}_r| = 4.0$ g, $G = 1.5$: (a) Inboard; (b) Outboard; (c) Top; (d) Bottom.
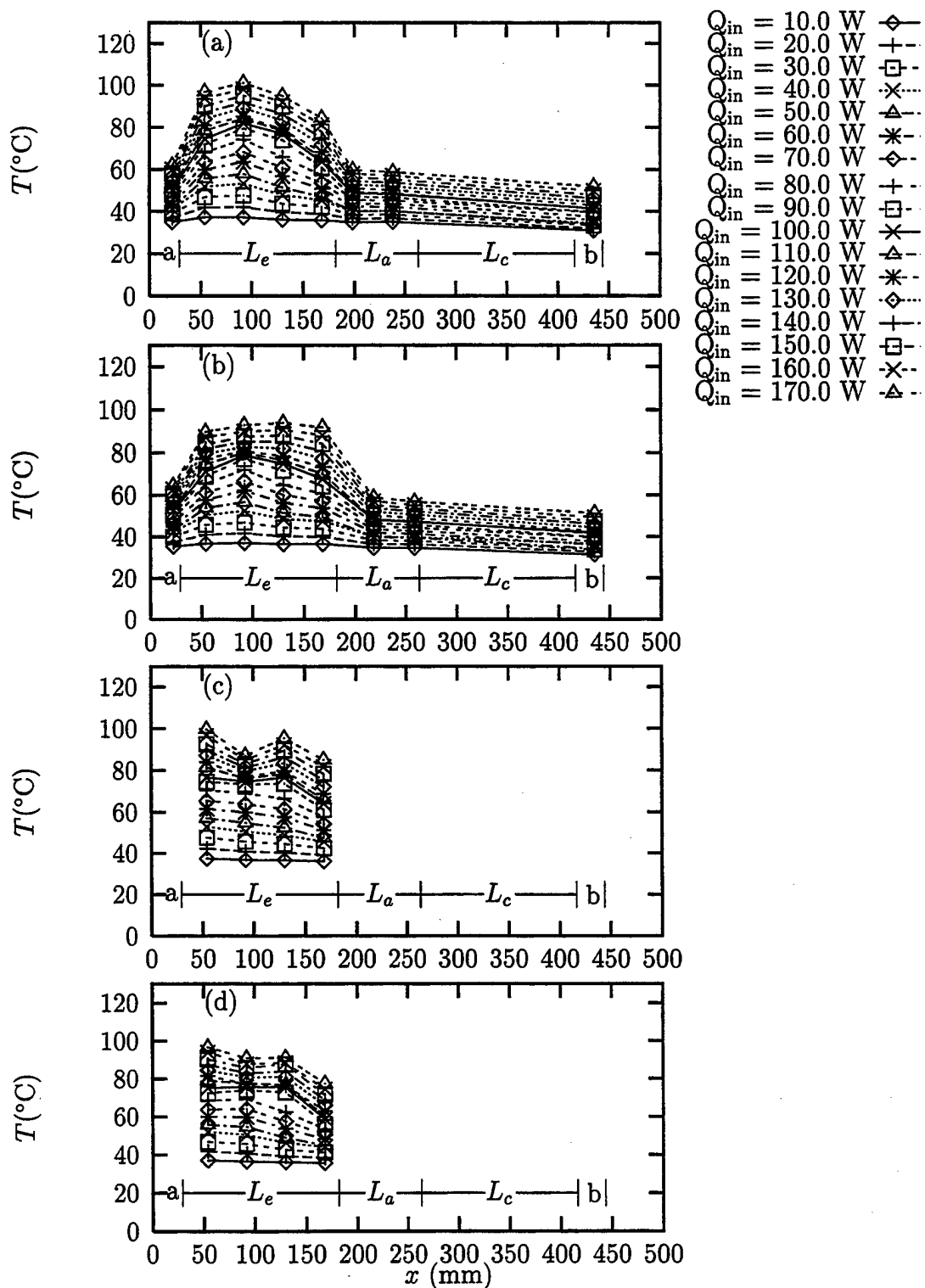
Figure 34: Steady state temperature distributions for $|\vec{a}_r| = 6.0$ g, $G = 1.5$: (a) Inboard; (b) Outboard; (c) Top; (d) Bottom.
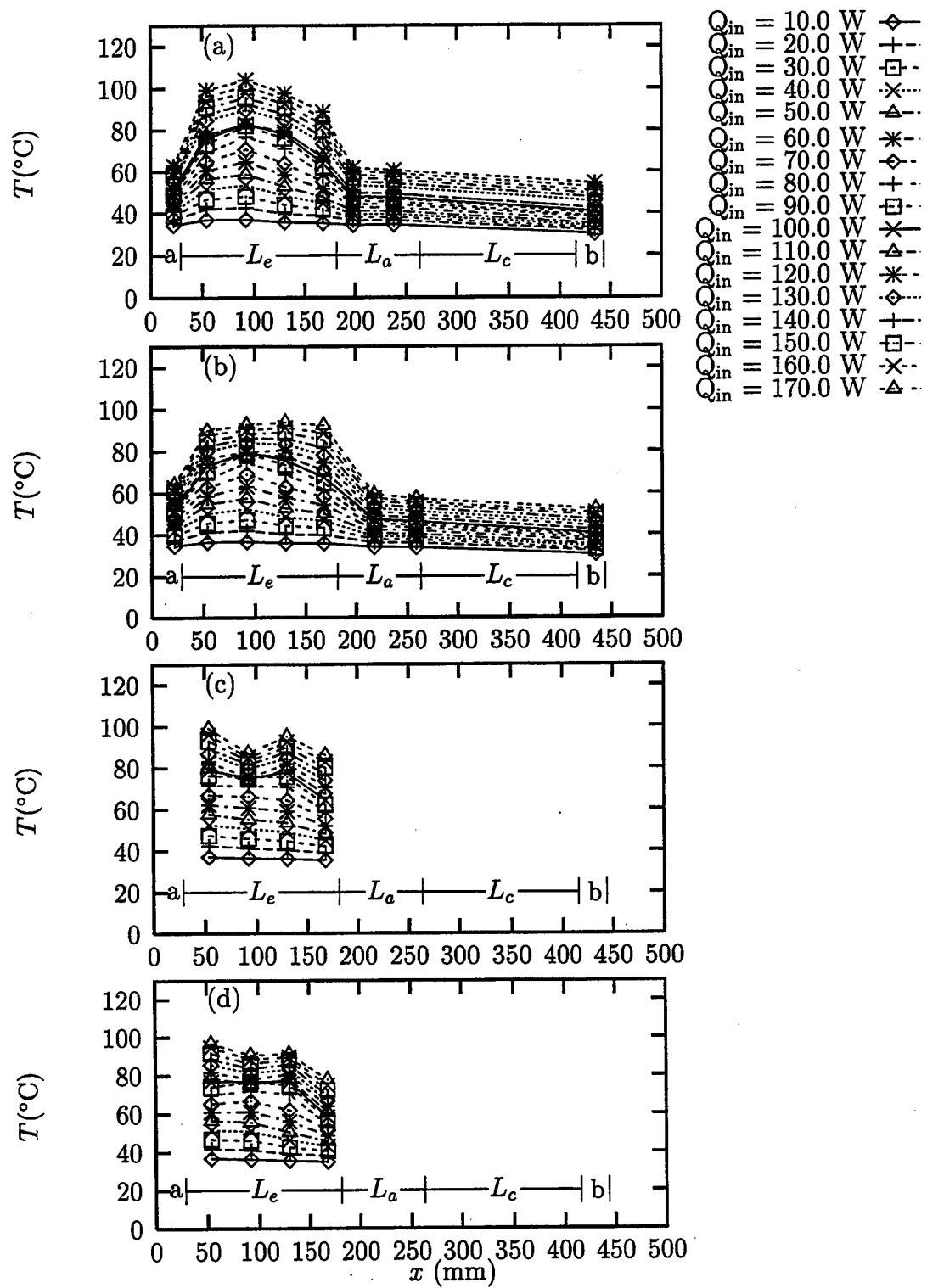
Figure 35: Steady state temperature distributions for $|\vec{a}_r| = 8.0$ g, $G = 1.5$: (a) Inboard; (b) Outboard; (c) Top; (d) Bottom.

91
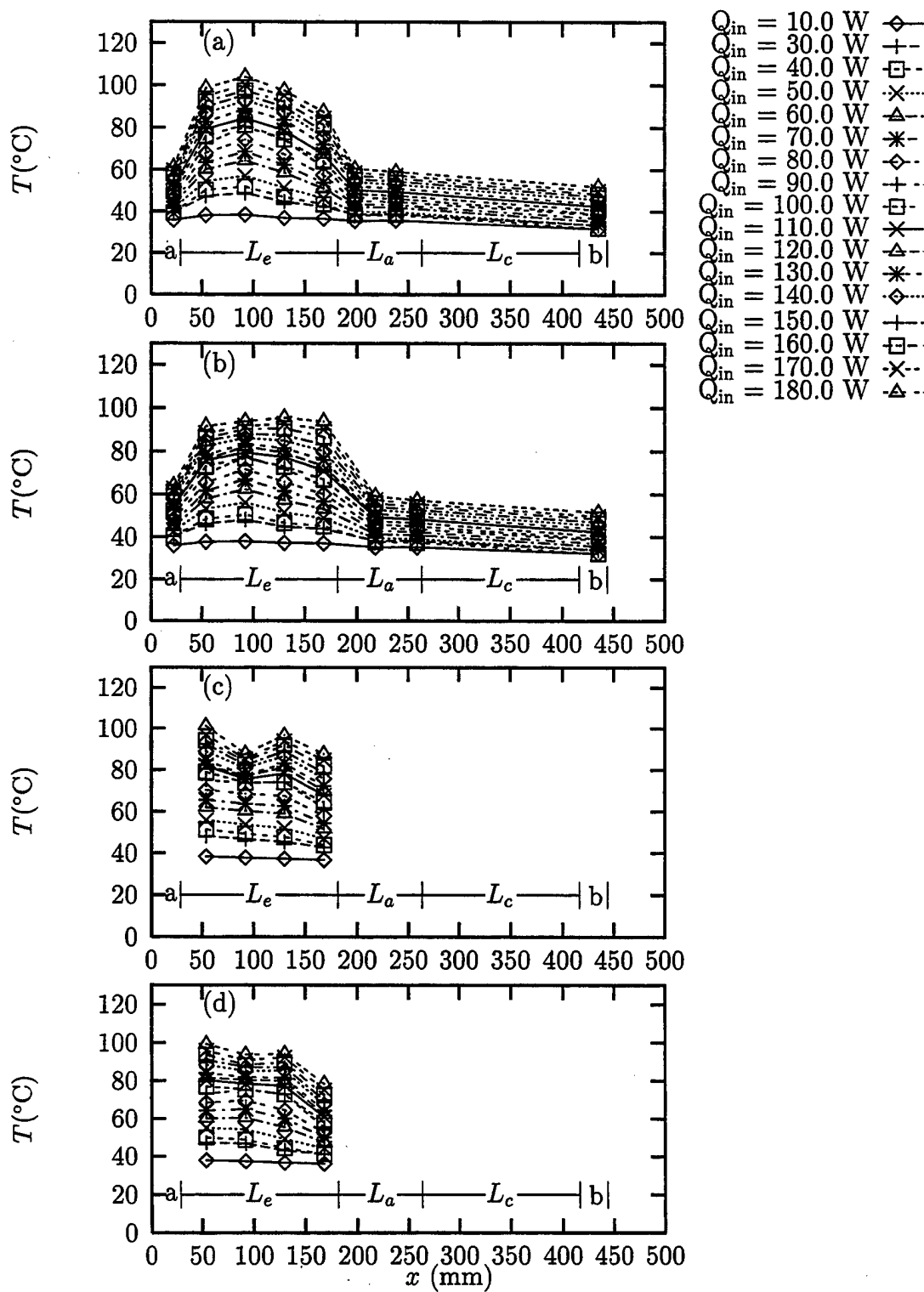
Figure 36: Steady state temperature distributions for $|\vec{a}_r| = 10.0$ g, $G = 1.5$: (a) Inboard; (b) Outboard; (c) Top; (d) Bottom.